Relationship between large-scale structural and functional brain connectivity in the human lifespan

by

Benedetta Toselli

Thesis submitted for the degree of *Doctor of Philosophy* (31° cycle)

December 2018

Marco Fato, Gabriele Arnulfo	Supervisors
Giorgio Cannata	Head of the PhD program

Dibris

Department of Informatics, Bioengineering, Robotics and Systems Engineering

Abstract

The relationship between the anatomical structure of the brain and its functional organization is not straightforward and has not been elucidated yet, despite the growing interest this topic has received in the last decade. In particular, a new area of research has been defined in these years, called *'connectomics'*: this is the study of the different kinds of 'connections' existing among micro- and macro-areas of the brain, from *structural* connectivity — described by white matter fibre tracts physically linking cortical areas — to *functional* connectivity — defined as temporal correlation between electrical activity of different brain regions — to *effective* connectivity — defining causal relationships between functional activity of different brain areas. Cortical areas of the brain physically linked by tracts of white matter fibres are known to exhibit a more coherent functional synchronization than areas which are not anatomically linked, but the absence of physical links between two areas does not imply a similar absence of functional correspondence. Development and ageing, but also structural modifications brought on by malformations or pathology, can modify the relation between structure and function.

The aim of my PhD work has been to further investigate the existing relationship between structural and functional connectivity in the human brain at different ages of the human lifespan, in particular in healthy adults and both healthy and pathological neonates and children. These two 'categories' of subjects are very different in terms of the analysis techniques which can be applied for their study, due to the different characteristics of the data obtainable from them: in particular, while healthy adult data can be studied with the most advanced state-of-the-art methods, paediatric and neonatal subjects pose hard constraints to the acquisition methods applicable, and thus to the quality of the data which can be analysed.

During this PhD I have studied this relation in healthy adult subjects by comparing structural connectivity from DWI data with functional connectivity from stereo-EEG recordings of epileptic patients implanted with intra-cerebral electrodes. I have then focused on the paediatric age, and in particular on the challenges posed by the paediatric clinical environment to the analysis of structural connectivity. In collaboration with the Neuroradiology Unit of the Giannina Gaslini Hospital in Genova, I have adapted and tested advanced DWI

analysis methods for neonatal and paediatric data, which is commonly studied with less effective methods. We applied the same methods to the study of the effects of a specific brain malformation on the structural connectivity in 5 paediatric patients.

While diffusion weighted imaging (DWI) is recognised as the best method to compute structural connectivity in the human brain, the most common methods for estimating functional connectivity data — functional MRI (fMRI) and electroencephalography (EEG) — suffer from different limitations: fMRI has good spatial resolution but low temporal resolution, while EEG has a better temporal resolution but the localisation of each signal's originating area is difficult and not always precise. Stereo-EEG (SEEG) combines strong spatial and temporal resolution with a high signal-to-noise ratio and allows to identify the source of each signal with precision, but is not used for studies on healthy subjects because of its invasiveness.

Functional connectivity in children can be computed with either fMRI, EEG or SEEG, as in adult subjects. On the other hand, the study of structural connectivity in the paediatric age is met with obstacles posed by the specificity of this data, especially for the application of the advanced DWI analysis techniques commonly used in the adult age. Moreover, the clinical environment introduces even more constraints on the quality of the available data, both in children and adults, further limiting the possibility of applying advanced analysis methods for the investigation of connectivity in the paediatric age.

Our results on adult subjects showed a positive correlation between structural and functional connectivity at different granularity levels, from global networks to community structures to single nodes, suggesting a correspondence between structural and functional organization which is maintained at different aggregation levels of brain units. In neonatal and paediatric subjects, we successfully adapted and applied the same advanced DWI analysis method used for the investigation in adults, obtaining white matter reconstructions more precise and anatomically plausible than with methods commonly used in paediatric clinical environments, and we were able to study the effects of a specific type of brain malformation on structural connectivity, explaining the different physical and functional manifestation of this malformation with respect to similar pathologies. This work further elucidates the relationship between structural and functional connectivity in the adult subject, and poses the basis for a corresponding work in the neonatal and paediatric subject in the clinical environment, allowing to study structural connectivity in the healthy and pathological child with clinical data.

Table of contents

II   Network-level structural and functional connectivity in the healthy and pathological child   46

5   Feasibility of advanced WM structural reconstruction on paediatric data at low magnetic field and low *b*-value   47

Nomenclature

Acronyms / Abbreviations

ACC	**A**genesis of the **C**orpus **C**allosum
AIC	**A**kaike **I**nformation **C**riterion
BIC	**B**ayesian **I**nformation **C**riterion
CC	**C**orpus **C**allosum
CPCT	**C**ortico-**P**onto-**C**erebellar **T**racts
cPLV	**c**omplex **P**hase **L**ocking **V**alue
CSD	**C**onstrained **S**pherical **D**econvolution
CSF	**C**erebrospinal **F**luid
CST	**C**ortico-**S**pinal **T**racts
CTT	**C**erebellar-**T**halamic **T**racts
DEC-TDI	**D**irectionally-**E**ncoded **C**olor **T**rack-**D**ensity **I**maging
DKI	**D**iffusion **K**urtosis **I**maging
dMRI	**d**iffusion **M**agnetic **R**esonance **I**maging
DWI	**D**iffusion **W**eighted **I**maging
EV	**E**igen**V**ector
FA	**F**ractional **A**nisotropy
FACT	**F**iber **A**ssignment by **C**ontinuous **T**racking
FC	**F**unctional **C**onnectivity
FOD	**F**iber **O**rientation **D**istribution
GM	**G**ray **M**atter
GMH-IVH	**G**erminal **M**atrix-**I**ntra**V**entricular **H**emorrhage
GMPI	**G**ray **M**atter **P**roximity **I**ndex
GUI	**G**raphical **U**ser **I**nterface
HC	**H**ippocampal **C**ommissure
HCP	**H**uman **C**onnectome **P**roject
HRI	**H**ubert-**R**and **I**ndex

ICVF	**I**ntra**C**ellular **V**olume **F**raction
iPLV	**i**maginary **P**hase **L**ocking **V**alue
ISOVF	**ISO**tropic **V**olume **F**raction
LFP	**L**ocal **F**ield **P**otential
MD	**M**ean **D**iffusivity
MLE	**M**aximum **L**ikelihood **E**stimate
MRI	**M**agnetic **R**esonance **I**maging
NODDI	**N**eurite **O**rientation **D**ispersion and **D**ensity **I**maging
ODI	**O**rientation **D**ispersion **I**ndex
PLV	**P**hase **L**ocking **V**alue
PT	**P**robabilistic **T**ractography
PVC	**P**artial **V**irtual **C**allosotomy
QSM	**Q**uantitative **S**usceptibility **M**apping
ROI	**R**egion **O**f **I**nterest
RMS	**R**oot **M**ean **S**quare
SC	**S**tructural **C**onnectivity
SD	**S**tandard **D**eviation
SEEG	**S**tereo-**E**lectro**E**ncephalo**G**raphy
segACC	**seg**mental **A**genesis of the **C**orpus **C**allosum
stDEC-TDI	**s**hort-**t**rack **D**irectionally-**E**ncoded **C**olor **T**rack-**D**ensity **I**maging
TDI	**T**rack-**D**ensity **I**maging
WM	**W**hite **M**atter

Chapter 1

Introduction

Brain structure and function are commonly assumed to be interlinked and statistically correlated [Skudlarski et al. (2008)]; in particular, many studies have found evidence that brain function is shaped by the underlying structural organization of the brain [Greicius et al. (2009); Sporns (2014)]. While it has been found that brain areas linked by anatomical connections will exhibit a stronger functional connectivity than non-physically-linked areas [Honey et al. (2009)], the absence of physical links between brain regions does not imply a missing functional link. On the contrary, strong statistical correlation is often found between the signals from cortical regions which are not directly connected by axonal tracts [Honey et al. (2009)]. The relationship between structural and functional organization in the brain is therefore not straightforward, and, despite the many studies conducted on this topic, it has not been completely understood yet [Damoiseaux and Greicius (2009)].

The study of how this link between anatomy and functionality develops and changes through the human lifespan has garnered strong interest in the last two decades. The first study which found a correspondence between structural connectivity from DWI data and functional connectivity computed with BOLD-fMRI in a single brain slice was by Koch et al. (2002). From that point on, many groups have tried to investigate how brain structure determines and influences brain functions and human behaviour, both in resting-state and during tasks. For example, Hagmann et al. (2008) found the same correspondence between structure and function in the whole brain, subdividing it into 66 separate areas; Cohen et al. (2008), on the other hand, studied the network engaged in adaptive behaviour during feedback-guided decision-making tasks, finding that the strength of the physical connections between several brain areas had a good correspondence with their functional connectivity.

Development and ageing are the first causes of structural and functional modification of the brain through the lifespan; congenital malformations, neurodegenerative pathologies and

acquired brain injury can produce changes in the micro- and macro-structure of the brain, influencing both its structure and its function [Sharp et al. (2014)]. In ageing, analysis of functional connectivity through functional MRI showed that cognitive decline in elderly people is mediated by the extent of white matter damage and caused by functional disruption in the coordination of brain systems supporting cognition, especially in the Default Mode Network [Andrews-Hanna et al. (2007)]. Achard and Bullmore (2007) also showed alterations of efficiency relative to the cost of small-world functional networks due to normal ageing or to the use of pharmacological agents. While the physical organization of the brain is more or less constant day-to-day [Honey et al. (2009)], it can change considerably during development and across longer time spans of weeks/months [Draganski et al. (2004); Kuner and Flor (2017)]; on the other hand, functional connectivity can change and reorganise itself in a very short time span [Bassett et al. (2006)]. The brain can change its whole organization during an individual's life through neuroplasticity, which gives it the ability to modify both its structural and functional organization as a response to injury or pathology, but also to learning and environmental or social stimuli.

The aim of this work was to investigate the relationship between large-scale, network-level structural and functional connectivity at different ages in the lifespan, in particular in infancy and young adulthood. Both ages present different characteristics and challenges, which I have tried to overcome during this work.

The healthy adult subject is one of the most studied 'cases' in neuroimaging, as it can be considered as the 'baseline' human subject. Many studies on the link between structural and functional connectivity on healthy adults exist; despite this, though, the nature of this correlation has still not been completely revealed [Honey et al. (2009)]. For example, while some of the variance in functional networks not predicted by structural organization has been explained by indirect coupling and interregional distance [Honey et al. (2009)], the plasticity of the brain and especially of its functional organization makes it difficult to obtain a complete 'model' of connectivity from indirect measures of the activity of single areas. The functional model is further complicated by the excitatory/inhibitory function of postsynaptic densities, which influence the way the electrical signals are propagated and maintained through the axons.

One of the most famous projects aimed at understanding this relationship is the Young Adult Human Connectome Project (HCP), which is part of the Human Connectome Projects (https://www.humanconnectome.org/) and which aims to map the brain's structural and functional organization in the healthy adult. The HCP aims to investigate brain structure with magnetic resonance imaging (MRI) and functional connectivity with resting-state

functional MRI (rs-fMRI) and magneto-encephalography (MEG). These are all non-invasive techniques; in my work, I chose to study functional networks obtained through stereo-electroencephalography (SEEG), an invasive technique used in patients who suffer from drug-resistant epilepsy, in which the neural activity is acquired through intra-cerebral electrodes implanted in the patient's brain. Though invasive and not applicable on healthy volunteers, SEEG presents a higher resolution than fMRI and MEG and directly records electrical activity in the brain. In order to be able to study only the 'healthy' brain activity recorded by these electrodes, all non-typical brain activity present in the recorded signals was removed, so that only typical, 'healthy' functional data was used to infer connectivity.

While SEEG data can be acquired also from paediatric subjects and analysed with the same techniques as adult data [Taussig et al. (2014); Cossu et al. (2008)], the methods used for computation of structural connectivity in healthy adults have been applied on paediatric MRI data only in advanced research studies, and not on data from a clinical environment. These analysis methods have very specific requirements in terms of the quality of the data to which they are applied; the clinical environment, on the other hand, introduces time constraints to the MRI exams and other limitations which make it impossible to acquire data with the required conditions, especially on paediatric subjects. In the second part of this work, I have focused on the application of advanced structural analysis to MRI data acquired at the Giannina Gaslini Hospital in Genova, which presented characteristics which made it suboptimal for this kind of analysis. The aim of this second part of the work was to adapt the advanced MRI analysis methods applied in the first part of the work for the use on neonatal and paediatric clinical data, in order to be able to study the brain's structural network as done with adult data.

During this PhD I have also developed an analysis pipeline for brain structural connectivity and microstructural white matter analysis, which integrates several existing software tools into a single processing pipeline and is currently being used at the Gaslini hospital for research purposes (Chapter 3).

Chapter 2

Background

2.1 Brain connectivity and the connectome

'Brain connectivity' refers to a pattern of physical links, statistical dependencies or causal interactions between single units within the nervous system. Connectivity patterns can be examined at different granularities within the system, from single-neuron level to neuronal populations to anatomically defined brain regions; different types of connections can also be taken into account, from white matter (WM) fibre pathways physically linking cortical brain regions (*structural* connectivity) to statistical correlation or causal relationships between electrical signal patterns originating from separate neuronal populations (*functional* or *effective* connectivity) [Sporns (2007)]. Connectivity patterns influence and restrict neural activity and, more broadly, human function and behaviour: the analysis of how this influence is exerted is then crucial to understand how the brain processes information and originates these behaviours.

The term 'connectome' was first used independently by Sporns et al. (2005) and Hagmann (2005) to refer to a mapping of the connections in the human brain. The term was inspired by the genome, namely a map of the human genetic code: in the same way, the idea behind the connectome is to produce a "comprehensive structural description of the network of elements and connections forming the human brain" [Sporns et al. (2005)]. This description can be seen as a network structure, with *nodes* — corresponding to single, well-delineated brain units — being connected by *edges*, corresponding to the actual connections through which these units communicate.

Three different 'types' of brain connectivity can be defined, depending on what is considered to be the 'connection' between two nodes of the network: these are structural, functional and effective connectivity. Structural (or anatomical) connectivity refers to the physical

presence of anatomical connections between sets of neurons or neuronal elements, creating a physical network. Functional connectivity is defined as "temporal correlations between remote neurophysiological events" [Friston (1994)] arising from brain units at different scales — from single neurons to neuronal populations to brain areas. In a functional connectome, the measure of connection between two brain areas is the correlation between their activity, as measured with different methods — from BOLD functional MRI, which measures the variation in blood oxygenation due to neuronal activity, to more direct measurements of electrical activity such as electro-encephalography (EEG). Effective connectivity refers to "the influence one neural system exerts over another" [Friston (1994)] and models direct causal effects between neural units [Sporns (2013)].

Sotiropoulos and colleagues [Sotiropoulos and Zalesky (2017)] subdivide the process of computing a connectome in two steps: the first step is to define the nodes which will form the network, and the second step is to find the edges connecting them. One of the main challenges in the compilation of the connectome is the definition of the structural elements which will become the nodes and edges of the final network structure. A structural network of the human brain could be defined at different scales, from the micro-scale — where nodes are the single neurons and edges are the synapses linking them — to the macro-scale, where nodes and edges are anatomically distinct brain regions and the WM pathways connecting them together. On one hand, at the micro-scale, single neurons and synapses are far too numerous to be considered as network elements and are also subject to rapid plasticity-induced changes [Sporns et al. (2005)]. On the other hand, brain regions are difficult to delineate, and there exist no single 'universal' parcellation scheme to define which nodes to use for the network. Despite these difficulties, the macro-scale is usually chosen as the best scale for the computation of connectivity networks.

At this scale, the nodes of the network are single cortical brain regions, as defined by a 'parcellation' scheme, namely a subdivision of the brain cortex into separate, definite regions with respect to some fixed criterion. Several such schemes exist; the criteria used for cortical subdivision can be anatomical - e.g. separation based on cortical folding, sulci and gyri, as done in Desikan et al. (2006) and Destrieux et al. (2010) - or relying on integration of different information; for example, Schaefer et al. (2017) defines a parcellation based on the subdivision of the cortical area in seven functional subnetworks, while Glasser et al. (2016) integrates information from cortical folding, myelin content maps and resting state fMRI to generate a parcellation from a dataset of 210 subjects. The appropriate number of regions which a parcellation should include is also a matter of discussion, and may depend on the application for which the connectome is to be used [Cammoun et al. (2012)]; for

this reason, in the last years, multi-scale parcellation schemes have been created through successive hierarchical subdivision of a coarse parcellation into finer schemes (see for example Cammoun et al. (2012), Schaefer et al. (2017)).

2.2 Estimation of structural connectivity

Once the nodes of a connectome have been defined with respect to some scheme or criterion, it is necessary to estimate the edges of the connectome network, i.e. the actual connections between nodes. As described before, the kind of connection depends on the type of connectivity being investigated: for structural connectivity, the edges will represent WM fibre pathways, while for functional connectivity the nodes will be considered connected if there is a statistical correlation between their electrical activities.

The most widespread non-invasive method to study structural connectivity in vivo is diffusion-weighted imaging (DWI), an MRI technique which maps the motion of water molecules along the different brain tissues. While in the cerebrospinal fluid (CSF) and gray matter (GM) water motion does not significantly prevail in any direction (*isotropic* diffusion), in WM, water molecules move preferentially along the direction of axons and fibre tracts (*anisotropic* diffusion). The patterns followed by the water thus reflect the underlying tissue structure, allowing the tracing and reconstruction of WM fibre tracts. The sensitization of the image to diffusion is obtained by varying the homogeneity of the MRI magnetic field with gradient pulses applied in several directions (see Appendix A for details on DWI acquisition).

Several methods exist to reconstruct WM fibre pathways from DWI data. The process needed for this reconstruction is composed of two steps: the first is the estimation of the WM fibre orientations in each voxel of the DWI volume, which are then used as input to tractography methods which propagate curves following the water diffusion direction throughout the brain, thus approximating the axonal pathways between cortical regions. The first and simplest method for estimation of diffusion directions is Diffusion Tensor Imaging (DTI) [Basser et al. (1994)], which assigns a single diffusion direction to each voxel; more complex models estimate a Fibre Orientation Direction (FOD) for each voxel, describing the fibre distribution at the given location [Sotiropoulos and Zalesky (2017)]. These advanced models allow a better characterization of the water diffusion patterns throughout the brain tissue and, coupled with probabilistic tractography techniques, produce WM tract reconstructions of higher quality and anatomical plausibility than the classical DTI model, which in turn allows to obtain more precise representations of structural connectivity [Farquharson et al. (2013)].

2.3   Estimation of functional connectivity

Functional connectivity can be estimated from data acquired through several methodologies: one of the most common acquisition methods is blood-oxygenation level dependent fMRI (BOLD-fMRI), which exploits the fluctuations in blood oxygen content caused by neuronal firing to estimate functional activity from a specific brain area. The functional correlation between brain regions can be computed either on data acquired with the subject at rest (resting-state BOLD-fMRI), or by administering specific stimuli to the subject and recording the brain's response to the specific task (task-based BOLD-fMRI). Usually task-based BOLD-fMRI is used to investigate specific functional subnetworks, because of the specificity of the brain's reaction to different stimuli and tasks; resting-state BOLD-fMRI is the method of choice to study global functional connectivity. The first direct comparison of structural and functional connectivity [Koch et al. (2002)] was done on data extracted from resting-state BOLD-fMRI, compared with structural connectivity from DTI data. Many fMRI studies have also defined functional networks involved in particular cognitive tasks, such as working and autobiographic memory [Addis et al. (2007)]; separate evidence of the existence of corresponding structural subnetworks has been provided by parallel tractography studies [Audoin et al. (2007)].

While BOLD-fMRI offers high reliability in space accuracy, it is an indirect method of estimating brain activity and has a poor temporal resolution (at the second scale), because of the slow response of the BOLD signal to neuronal activation [Lei et al. (2010)]. More direct methods of brain activity estimation exist, with a higher temporal resolution (millisecond scale): magneto-encephalography (MEG) records the magnetic fields produced by electrical neuronal activity, while electro-encephalography (EEG) directly measures voltage fluctuations due to neuronal currents. Because of the different time scale, these methodologies measure different neuronal processes; however, independent studies using either fMRI, MEG or EEG to estimate functional activation have reached the same conclusions [Hamandi et al. (2008); Garcés et al. (2016)]. Graph theory analyses have been applied to the study of functional connectivity with MEG, surface and depth-EEG studies of brain connectivity [Reijneveld et al. (2007)]. Bassett and colleagues [Bassett et al. (2006)] used wavelet decomposition of MEG signal to demonstrate that small-world properties of functional networks in healthy subjects were maintained at different time scales, in both rest and task conditions.

As mentioned before, while fMRI presents a low temporal resolution and indirectly estimates brain function through blood oxygenation, EEG directly records electrical activity from neuronal populations, but suffers from poor spatial resolution and volume conduction

effects, due to the separation of the electrodes from the brain. To overcome these drawbacks, stereo-electroencephalography (SEEG) is used: this is an invasive recording methodology, which acquires high SNR signals through intra-cerebral electrodes implanted in the subject's brain. This technique is commonly used in patients suffering from drug-resistant focal epilepsy during pre-surgical evaluations for resection of the epileptogenic zone; the data acquired through the electrodes present a high Signal-To-Noise ratio, and the signal source can be easily reconstructed through segmentation of a post-implant CT scan [Narizzano et al. (2017)]. However, because of its invasiveness, it is obviously not applicable on healthy volunteers.

The first part of this thesis has focused on the estimation and comparison of structural connectivity — computed through advanced diffusion analysis and probabilistic tractography — and functional brain connectivity from SEEG data in the healthy adult. The aim of this first work was to investigate whether the higher quality of SEEG data and WM reconstructions from advanced tractography would allow to gain more insight into the link between structure and function for normal, healthy adult data than what has been done using BOLD-fMRI and classical DTI. The SEEG data were stripped of all pathological, non-typical activity in order to study only the normal activity contained in the signals: in this way, we were able to compare the functional data with DWI data from healthy subjects.

2.4 The estimation of structural connectivity in the paediatric clinical environment

As introduced in Section 2.2, DTI is the most widespread method of estimating WM fibre orientation from DWI data, but the model it is based on does not allow to reconstruct more than one fibre tract passing through a voxel. It is thus unsuitable for the reconstruction of a variety of fibre configuration, such as crossing or 'kissing' fibres, and for the correct determination of fibres' cortical terminations [Abhinav et al. (2014)]. Many methods have been developed in order to overcome this limitation (for example, see Daducci et al. (2014) for a review), based on different models and each with specific requirements as far as data acquisition and computational burden for the reconstruction of WM pathways.

Constrained Spherical Deconvolution (CSD) was first introduced by Tournier et al. (2004) and successively refined in Tournier et al. (2007). This model belongs to the family of methods which compute a Fibre Orientation Distribution (FOD) for each voxel, modelling the distribution of WM axons at the given location; probabilistic tractography (PT) algorithms

can then be applied to these FODs to integrate the orientation information and obtain so-called 'streamlines', which represent WM fibre pathways in the brain. This enables CSD to fully represent any configuration of WM tracts, such as crossing or fanning fibres, producing reconstructions that are more faithful to the real WM anatomy than those obtainable with DTI [Toselli et al. (2017)]. (see Appendix A for details on DTI limitations and the CSD model).

CSD is often applied to studies of specific WM tracts and the effects on function and behaviour of microstructural damage or injury. Liégeois and colleagues [Liégeois et al. (2013a); Liégeois et al. (2013b)] studied which tractography-derived measures best predicted language outcome and presence of dysarthria after childhood brain traumatic injury; Northam and colleagues [Northam et al. (2012)] evaluated the relationship between WM microstructure and speech deficits in adolescents born very preterm, with a spectrum of brain injuries; Gordon and colleagues [Gordon et al. (2012)] studied reorganization of motor pathways and cortical motor activity caused by an arterial ischaemic stroke in the perinatal period in an 11-year-old child.

Among the several advanced diffusion methods existing, CSD combines good quality of WM reconstructions with less stringent requirements — in terms of acquisition characteristics and time needed for both the exam and the processing — than other methods such as Diffusion Spectrum Imaging [Wedeen et al. (2008)], which has very high hardware requirements and quite long acquisition and processing times. However, in order to fully exploit the capabilities of the CSD method, specific acquisition parameters are still required, including a strong MRI magnetic field (i.e., 3T or above), a high number of gradient directions along which to acquire the signal (from a minimum of 30 up to 60 and more), and high values of the b parameter, which measures the 'sensitivity' of the DWI sequence to the water diffusion (optimal value, 3000 s/mm^2 [Tournier et al. (2013)]; see Appendix A for the role of the b parameter in a DWI acquisition).

These protocols require a longer acquisition time than most acquisitions commonly done in clinical environments, where there exist strict time constraints on the maximum exam length and often on the available hardware (MRI scanners, processing stations, etc.), and are thus often unfeasible. This is especially true in the case of paediatric clinical environments: for exams on children and neonates, the time requirements are even more strict than for adults. Moreover, paediatric DW imaging is challenging, especially in neonates (see Yepes-Calderon et al. (2017) for a discussion). For any imaging sequence, the overall image quality is lower than that of an adult image, because the neonatal brain has a lower myelin content than the adult brain, and neonatal GM and WM have a similar water content. For the same reason, the

average diffusivity is higher in the neonatal brain than in the adult brain [Hüppi and Dubois (2006)]. Since it is difficult to keep a non-sedated neonate immobile during the exam session, short DWI acquisition sequences with few gradient directions and low b-values are usually applied, so as to keep the examination as short as possible.

For all these reasons, DTI is commonly used to evaluate WM structure in neonates and children in the clinical environment, since it is easily applicable on acquisition sequences commonly used in this setting and produces acceptable results, despite its limitations. Advanced tractography methods are not applied often in the clinical setting, because they are too demanding in terms of scan duration, especially in children and neonates. Among the main factors that influence the choice of processing methodology in a diffusion study, magnet field strength and the parameters of the DWI acquisition sequence (mainly the number of gradient directions and the b-value) greatly influence image quality, and thus significantly impact on the yield and applicability of the method in individual cases.

In the last two years, a few studies involving neonates and unmyelinated infants have used CSD-PT. Pieterman et al. (2016) investigated the change in connectivity of specific tracts in neonates in the first weeks of life; the images for this study were acquired on a 3T scanner, with a DWI sequence well suited to the application of CSD-PT (64 gradient directions and a b-value of 2500 s/mm^2). Batalle et al. (2017) studied brain connectivity and development in 65 neonates under 46-week post-menstrual age, by performing CSD-PT on DWI data acquired on a 3T scanner with multiple b-values, which allows to further improve the characterization of the signal and the subsequent WM reconstructions. Salvan and colleagues [Salvan et al. (2017)] analysed the microstructure of the arcuate fasciculus in 43 preterm neonates at term-equivalent age, correlating it with linguistic skills at 2 years of age: again, the study was conducted on a 3T scanner, with high angular resolution data acquired with 64 gradient directions and a b-value of 2500 s/mm^2. 33 of the 43 neonates were sedated orally during scans. All these studies were performed with hardware and acquisition sequences specific for the application of CSD-PT; the optimal conditions for this kind of studies cannot be reproduced in the clinical environment, where often low-field scanners (1.5T) and insufficient processing tools are found. Sequences acquired on 1.5T MR scanners at low b-values (around 1500 s/mm^2) are usually processed with DTI analysis to determine diffusion metrics such as fractional anisotropy (FA), using deterministic tractography to extract connectivity measures.

The second part of this work focused on the adaptation of CSD-PT analyses for the paediatric clinical environment, in collaboration with the Neuroradiology Unit of the Giannina Gaslini Hospital in Genova. The aim of this second part of the work was to allow clinicians

to investigate WM structure and connectivity using advanced diffusion techniques, in order to fully exploit their advantages over classical DTI analyses. These methodologies were then applied to a specific type of brain congenital malformation, partial agenesis of the corpus callosum, in order to investigate the modifications to structural connectivity that this pathology can cause, and to try to explain the functional and behavioural symptoms presented by patients suffering from it. Agenesis of the corpus callosum is among the most common congenital malformations of the human brain [Bedeschi et al. (2006)], presenting an extreme heterogeneity in causes and presentation [Dobyns (1996)]. The formation of the corpus callosum — a thick bundle of WM fibres which is the main connection between the brain's hemispheres — can begin as early as 6 weeks of gestation [Schell-Apacik et al. (2008)], and investigations of the mechanisms determining the causes of this pathology could shed light on the development processes of this important part of the brain. The final aim of this section of the work was to compute brain structural connectivity with the same methods used on healthy adult data in the first part of the work, in order to make it possible to repeat the same correlation analysis on paediatric functional data in future.

2.5   Organization of the work

The main objective of this thesis was to study the relationship between structural and functional connectivity in the human brain at different ages of the human lifespan, in particular in healthy adults and both healthy and pathological neonates and children.

The first section of the thesis is focused on the image processing methods on which my PhD work is based. Chapter 3 details the analysis pipeline I have developed during the PhD, integrating different neuroimaging toolboxes in a single software which is currently in use at the Gaslini hospital for research purposes.

The second section of the thesis, containing the main projects I have worked on during the PhD, is subdivided in two parts, reflecting the two parts of the work I have conducted. Part I describes the analysis of the relationship between structural and functional connectivity in healthy adults, with structural data from DWI and CSD-PT analyses and functional data from SEEG (Chapter 4), while Part II contains the description of my work on adapting and testing CSD-PT reconstruction and connectivity analysis on paediatric clinical data. In particular, Chapter 5 describes the feasibility testing and adaptation of CSD-PT and tract-density imaging (TDI) to paediatric data acquired with a 1.5T scanner and a suboptimal acquisition sequence at the Giannina Gaslini Hospital in Genova; Chapter 6 contains the application of the tested and validated methods to a specific pathological case – a group of

children suffering from partial agenesis of the corpus callosum, a condition in which the corpus callosum is not formed completely before the birth, but only a section of it is missing. We compared these subjects with a group of matched healthy controls and investigated how modifications to the brain's structure changes connectivity and produces functional symptoms in the patients. Chapter 7 contains a discussion of the main results of this work of thesis, and a brief explanation of the future research activity which is the natural continuation of this work. At the end of this thesis, Appendix A describes in more depth the structural analysis methods I have used in this work, namely the DTI method, its main limitations and how the CSD-PT method overcomes them; Appendix B contains supplementary material for the work described in Chapter 6.

Chapter 3

Analysis pipeline: the Brain Tractography App (BTractApp)

All the CSD-PT analyses, tractography computations and structural connectivity studies in this thesis were executed with an integrated analysis pipeline which I developed and maintained during my PhD, and which is currently also being used by clinicians at the Gaslini hospital in Genova. The pipeline started as a tool to execute simple tractography on DWI data, and is thus called Brain Tractography App (BTractApp), even if it now includes also connectome generation, network statistic computation and other WM microstructural analysis tools.

The BTractApp pipeline integrates several neuroimaging tools commonly used both in research and clinical environments: the FSL toolbox, Freesurfer's `recon-all` function to produce brain parcellations, the MRtrix3 toolbox, plus MATLAB scripts using the BCT toolbox to execute some group-level network analyses and produce group-consensus connectomes and graph-based measures for a group of subjects. The pipeline can analyse single subjects or groups, with the possibility of selecting which subjects in a folder to analyse and which to skip; it can work on DICOM or Nifti input images, and produces several types of output files (from Nifti images to different types of tractogram files, comma-separated-value files for connectomes, ASCII text files for group network statistics, etc.). It is divided into sections, roughly defining different stages of the analysis. Each stage can be executed or not, depending on the input data and on the aim of the analysis. At each stage, the pipeline will check if all the input files for that section are present and, if not, will stop with an error message to the user.

In addition to the software and toolboxes used for this thesis, BTractApp integrates also the DKE and AMICO toolboxes for WM microstructural analysis. This section of the

pipeline was not used for the studies described in this thesis, but it was implemented and integrated as an option into the analysis workflow for future use in research activity which was planned together with the Gaslini Unit.

BTractApp is written in the Python language, to integrate different toolboxes in a transparent way to the user: it can be executed both by command-line and using the graphical interface, developed with the Tkinter toolbox in Python. Each stage of the analysis requires several parameters to be set: this can be done either through the graphical interface (where the main parameters for each method and algorithm are adjustable) or through a single text configuration file, which can be then fed to the command-line version of the pipeline. Different configuration files can be set, either subject-specific or group-specific. The default parameters are the ones tested and selected for the analysis on paediatric data during my work at the Giannina Gaslini hospital [Toselli et al. (2017)], but the pipeline has been successfully applied also to adult data from the HCP project and other types of input data. A scheme of the pipeline is shown in Figure 3.1.

3.1   Preprocessing

The first stage of the analysis for any kind of study is the preprocessing of the raw data. For this step, the BTractApp pipeline uses the FSL toolbox [Jenkinson et al. (2012)], which is one of the most used toolboxes in the imaging community, and some functionalities from the MRtrix3 toolbox [Tournier et al. (2012)].

The only required input data is the diffusion weighted data: other input can include a T1-weighted anatomical volume, and a diffusion weighted volume acquired with $b = 0$ and a phase encode direction opposite to the one used in the main diffusion weighted sequence (the so-called "blip-up-blip-down" acquisition), in order to apply eddy currents correction to the main data. The raw input images can be both in DICOM and Nifti format: the pipeline will adapt the first steps of the preprocessing accordingly. If the diffusion weighted images are in Nifti format, the diffusion scheme adopted in the acquisition must be provided separately, through two files listing the b-values and the acquisition directions used in the exam (FSL's `bvals` and `bvecs` files). If these files are not present, FSL cannot obtain this information from the data: the pipeline will thus stop with an error.

The main steps of the preprocessing stage are: denoising, Gibbs ringing removal, bias field removal, motion and eddy correction. All the steps are independent of each other and the user can choose which ones to perform, according to the input data. Almost all of them are applied to the DWI volumes.
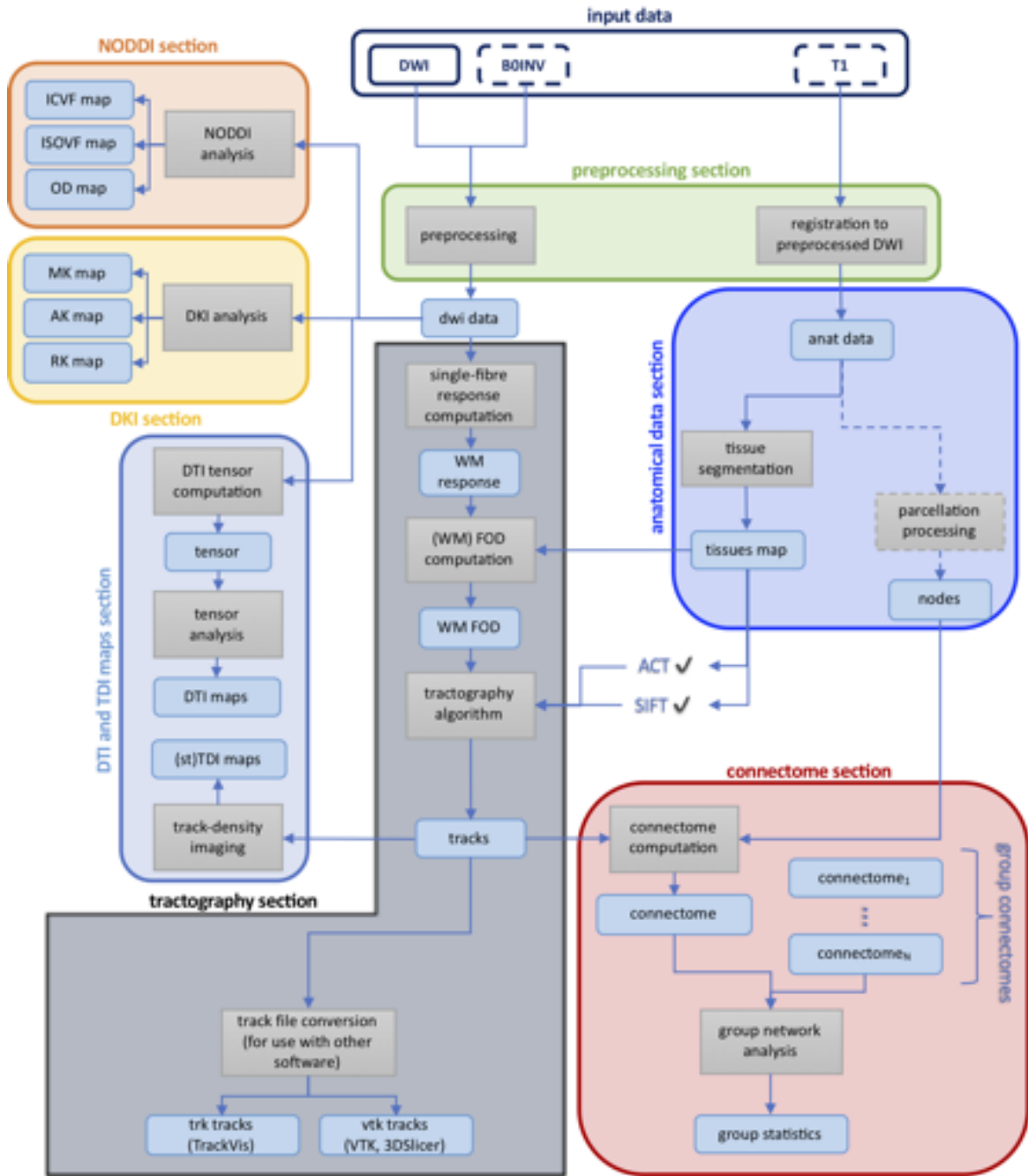
Figure 3.1 Scheme for the BTractApp processing pipeline. Dashed lines for input data indicate optional volumes (the only required volume is the DWI volume). 'B0INV' indicates blip-up-blip-down sequence, either full 4-D volume or single $b = 0$ image acquired with opposite phase direction than DWI volume. Grey squares represent processing steps, while blue rounded squares represent data produced by the pipeline. The scheme represents the analysis for a single subject; in the connectome section, the group network statistics computation can be executed only if the analysis is being run on a group of subjects, and will be the last step performed by the pipeline. The dashed rectangle and arrow lines for the parcellation step indicates that it is an external processing step, which must be done separately from the BTractApp software and the results of which will be then fed to the pipeline. The scheme includes the optional NODDI and DKI processing sections: these were not applied in any of the studies described in this work, but were implemented and tested for future use in collaboration with the Neuroradiology Unit at the Gaslini hospital.

The denoising step is done using the `dwidenoise` function from the MRtrix3 toolbox, which will also output a map of the estimated noise to allow the user to better check the results. The next step is the removal of the so-called Gibbs ringing artefacts, which appear as thin parallel lines close to high-contrast interfaces in an image. The removal of these artefacts is done with the MRtrix3 `mrdegibbs` function. After this removal, the preprocessing proceeds with the MRtrix3 `dwipreproc` function, which tries to apply motion and eddy current correction to the image.

The `dwipreproc` script itself uses functions from the FSL library, namely `eddy`, `topup` and `applytopup`, in order to correct the DWI images for motion, eddy current-induced distortion and susceptibility-induced distortion The last correction (applied by the `eddy` function) can be done only if the DWI acquisition includes a so-called "blip-up-blip-down" sequence - that is, an additional acquisition of one or more volumes (typically, one or more pairs of spin-echo $b = 0$ EPI volumes, or a full DWI volume equal to the original one) having the same readout time as the DWI volumes, but the exact opposite phase encoding direction. These additional images are used by `eddy` to estimate the inhomogeneity field of the DWI volumes, and to correct the distortion it causes. If this additional sequence is not present in the input data, the `dwipreproc` script will perform motion and eddy current correction only. BTractApp allows the user to select whether to apply the inhomogeneity field estimation, and to provide the additional sequence to the algorithm: if the option to correct for inhomogeneity is selected, but the additional sequence is not present, BTractApp will warn the user with a message and will proceed with the motion and eddy corrections only.

The last step of the DWI preprocessing stage is the removal of the bias field caused by the B1 inhomogeneity. This is done with the `dwibiascorrect` MRtrix3 script, which uses either the `N4` algorithm from the ANTs toolbox (http://stnava.github.io/ANTs/) or the FAST function from FSL for the bias correction. The algorithm to be used can be selected by the user with a parameter in the BTractApp GUI or configuration file. The estimated bias field will also be computed and saved as a Nifti file.

At the end of the preprocessing stage, the final, preprocessed DWI volumes will be saved as a Nifti file and as a `.mif` file, a format specific to MRtrix3 which encodes more information than the traditional Nifti (for example, DWI `.mif` files can encode the diffusion directions and b-values in their header, while Nifti files cannot maintain information about the diffusion acquisition sequence and need external text files for this information). The `.mif` format is used throughout the BTractApp pipeline for all analysed data, in order to fully exploit the MRtrix3 functionalities; all the "final" outputs from processing steps (e.g.

the preprocessed DWI data, brain masks, anatomical data, parametric maps and more) are also saved as Nifti, for use with other image-viewing or analysis software.

After preprocessing, if an anatomical T1 sequence is present, it will be registered to the preprocessed DWI data using the FLIRT tool from FSL. This is done to ensure that all subject's data is analysed and processed in the same space. The registration is done by default with a rigid transformation (6 degrees of freedom) and with normalized mutual information as cost function, but the user can modify these choices if needed. The transformation is computed, then applied separately to the T1 volume maintaining the original resolution and field of view, in order to avoid reducing the original voxel dimensions and cropping sections of the anatomical image not present in the DWI field of view.

As a last step of the preprocessing stage, a binary brain mask is computed from the preprocessed DWI data using the `dwi2mask` MRtrix3 function: this mask will be used in all the subsequent steps in order to define which voxels contain brain tissue.

3.2   Connectivity analysis

The connectivity analysis panel is composed of all the processing steps needed to produce a structural, whole-brain connectome for a single subject or a group of subjects. It also includes mapping of diffusion parameters and super-resolution track-density maps [Calamante et al. (2010)].

3.2.1   Tractography

The default behaviour for the tractography stage is to produce a whole-brain tractogram from the preprocessed DWI data, using the parameters chosen by the user and set through either the GUI or the configuration file. The whole tractography stage is composed of functions from the MRtrix3 toolbox.

The first step is the computation, for each voxel, of a Fibre Orientation Distribution (FOD) which describes the orientation distribution of the water molecules in the selected voxel. This is done in two steps: first the single-fibre response is estimated from the DWI data, and then the actual FODs are estimated using the computed responses.

The single-fibre response is computed using the `dwi2response` script with the `dhollander` algorithm for unsupervised estimation of WM, GM and CSF [Dhollander et al. (2016)]. This algorithm will compute three separate responses, one for each brain tissue (WM, GM and

CSF), without the need for an additional T1 image for tissue segmentation (as does the `msmt_5tt` algorithm of the same toolbox).

The computed responses are then used for the FOD estimation, using the `dwi2fod` command. This command offers two algorithms for the computation: `csd` and `msmt_csd`. The first algorithm requires so-called single-shell DWI data, namely from an acquisition scheme with a single non-zero b-value applied along all acquisition directions, coupled with a single WM-response, and will produce a single FOD computed as if all the voxels in the data contained WM. This can be inappropriate in voxels containing a mixture of WM and other tissues. The second algorithm provided by the MRtrix3 toolbox requires DWI data from a multi-shell acquisition scheme, with several non-zero b-values applied to different subsets of the acquisition directions (the so-called 'shells'): more precisely, it needs as many distinct b-values and as many tissue responses as the number of tissue FODs to be estimated. The $b = 0$ volumes are included in the count, so a single-shell sequence will be enough to produce two separate FODs (WM and CSF: the GM response will inherently not be used in the fit), while in order to have three separate tissue FODs a multi-shell sequence with two non-zero b-values will be needed. BTractApp will automatically detect the number of non-zero b-values in the data and provide the `msmt_csd` algorithm with all the computed tissue responses or only the WM and CSF ones depending on the acquisition scheme detected. The result of this step will then be two or three tissue FODs, depending on the data: for multi-shell acquisitions, all three tissues will have a FOD response, while for single-shell data only the WM and CSF FODs will be computed.

The WM FODs are then provided to the tractography algorithm, to produce the final tractogram. This is done with the `tckgen` command, which accepts a wide variety of parameters and input data.

The first and main input to the tractography is the file with the computed WM FODs, which provide the distribution of directions to be tracked in each voxel. The MRtrix3 toolbox provides different tracking algorithms, both deterministic and probabilistic: BTractApp applies the default one, a probabilistic streamlines method applying second order integration called `iFOD2` [Tournier et al. (2010)]. The main parameters for this method are: number of streamlines for the final tractogram (default is 10 millions); maximum angle between successive steps of the tractography algorithm (selected default is 50°); FOD amplitude limit, under which the streamline is terminated (default is 0.1); maximum streamline length (default is 200).

BTractApp allows the user to select and use two frameworks which can improve the quality and anatomical plausibility of the resulting tractogram: these are the Anatomi-

cally Constrained Tractography framework (ACT; [Smith et al. (2012)]) and the Spherical-deconvolution Informed Filtering of Tractograms (SIFT; [Smith et al. (2013)]). The first framework provides mechanisms to influence streamline termination and whether or not a generated streamline is anatomically plausible and can therefore be retained in the final tractogram or needs to be rejected; these mechanisms can be integrated in the tractography step by selecting the ACT option either in the BTractApp GUI or with the configuration file. ACT requires a tissue segmentation of an anatomical volume in order to derive prior anatomical knowledge and structural information and to incorporate that information in the tracking process: if the ACT option is selected in BTractApp and a T1 anatomical volume is present in the subject's folder, the software will automatically trigger the generation of the segmentation volume using the `5tt` command from MRtrix3.

SIFT is a method which needs to be applied on a computed tractogram, and it will filter out streamlines from this original tractogram in order to improve the biological accuracy of a streamline reconstruction. This is done by finding a subset of the original streamlines which best matches the DWI data, correcting some of the biases inherent to the streamline seeding and generation process and producing a second tractogram in which the density of the streamlines better represents the density of the underlying biological connections [Smith et al. (2013)]. SIFT requires only the DWI data as input, but can accept also a tissue segmentation volume (the same used for the ACT step) to incorporate also structural and anatomical information. Since SIFT works by filtering out streamlines from a first tractogram to produce a second, more precise one, the first tractogram must contain a very high number of streamlines, which will then be reduced in the second reconstruction: often the SIFT algorithm is applied reducing the number of streamlines of about an order of magnitude [Calamante et al. (2012)]. For this reason, the default number of streamlines to be retained in the SIFT-ed tractogram for BTractApp is 2 millions against an original number of 10 million, but both numbers can be modified by the user.

DTI and TDI maps

The last processing stage included in the tractography section of BTractApp is the generation of parametric maps from the DWI data. The first maps that can be selected by the user are the classical DTI diffusion parameters: mean and radial diffusion (MD and RD) and eigenvalues maps (λ_1, λ_2 and λ_3). To compute these, the software will first estimate the DTI diffusion tensor for the DWI volume (command `dwi2tensor`), and then compute the selected maps with the `tensor2metric` command. Other maps that can be produced are track-density maps, using the so-called Track-Density Imaging (TDI) framework developed by Calamante

et al. (2010). These maps are computed from the tractography reconstruction, and assign to each voxel a gray-level value representing the number of streamlines traversing it in the reconstruction. If the relevant option is selected, another TDI map can be produced, with each voxel containing not a grey value but a RGB value, representing both the streamline density and the main direction in the voxel (DEC-TDI maps). These maps can also be computed from a so-called 'short-track' tractogram, which is a streamline reconstruction in which the maximum streamline length is set to a very small value: this type of tractogram produces a TDI or DEC-TDI map in which the longer, denser WM tracts do not have an image contrast much higher than thinner tracts, and thus are more legible than normal TDI maps, avoiding over-saturation of main WM tracts. If the short-track maps are selected, BTractApp will automatically trigger the generation of the short-track tractography, using the same parameters as the normal one and the selected number of short streamlines (default is ten times the number for the original tractogram [Calamante et al. (2012)]) and maximum length (default is computed to be about ten times the voxel size [Calamante et al. (2012)]).

All these maps can be used either alone, for the investigation of DTI parameters and WM structure, or they can be used to 'weigh' the connectome computed in the next step in different ways; for example, it is possible to obtain connectivity matrices in which the weight of an edge is the average FA value along the fibres connecting the corresponding nodes. This can be done with any image or map the values of which can be sampled along the streamlines, producing weights for the resulting edges.

3.2.2   Structural connectome

After the tractography computation, BTractApp allows the user to select one or more parcellation schemes for which to compute a connectome matrix from the tractogram. The available parcellation schemes are the Desikan-Killiany [Desikan et al. (2006)] and Destrieux [Destrieux et al. (2010)] schemes from Freesurfer, the BCI parcellation scheme from BrainSuite and the Schaefer parcellation scheme [Schaefer et al. (2017)], based on the subdivision of the brain in 7 functional subnetwork proposed by Yeo et al. (2011). The parcellation data needs to be computed by the user with the relevant software, separately from the BTractApp processing, and included in the subject's data: BTractApp assumes that the Freesurfer data from the segmentation of the brain according to the Desikan and Destrieux atlases are contained in the subject's base directory, in a folder named `recon-all` having the same structure as Freesurfer's original results folder, while the data for the BrainSuite parcellation should be

placed in a folder named `brainsuite` and the data for the Schaefer parcellation is contained in a folder named `schaefer`.

For each selected parcellation scheme, BTractApp will convert the labelled volume computed by the external software into the `.mif` format used by MRtrix3, converting the labels with respect to a lookup table contained in the BTractApp default files, and will compute the connectivity graph given by considering the relabelled parcels as nodes and the final tractogram from the tractography step as edges. The edge weights will be the number of streamlines connecting each pair of nodes. The user can select options to set the diagonal of the resulting connectomes to zero (namely, ignore self-connections), to normalize the edge weights by dividing them for the sum of the corresponding nodes' volume and length, and to compute a representative streamline for each edge and a mesh surface for each node, for visualization purposes.

If the 'batch' version of the software is used to analyse a group of subjects, it will provide the user with the possibility to select and execute a group network analysis on the group's subjects, using one or more of the selected parcellation schemes. This analysis has been implemented in MATLAB, using the Brain Connectivity Toolbox (BCT; https: //sites.google.com/site/bctnet/), and integrated in the software: it includes the computation of a group 'consensus' connectome (as defined in Owen et al. (2013); see for example Severino et al. (2017)) and the computation of several network measures both on a binarized version of the computed networks and on the original weighted ones.

3.3   Future applications: WM microstructural analysis

The microstructural analysis stage of the pipeline is independent of the tractography and connectivity analysis, and can be executed alone after the preprocessing stage. This analysis stage was implemented and tested on both adult and paediatric data, as a propaedeutic step for future research projects. The maps produced in this stage can integrate the WM analysis on development or specific pathologies.

The two microstructural models integrated in the analysis pipeline are the Diffusion Kurtosis Imaging (DKI) and the Neurite Orientation Dispersion and Density Imaging (NODDI). Two external toolboxes have been integrated in BTractApp to execute the relative analyses: for DKI, I tested and integrated the Diffusional Kurtosis Estimator (DKE, http://academicdepartments.musc.edu/cbi/dki/dke.html), while for the NODDI analysis I chose the AMICO toolbox (https://github.com/daducci/AMICO) developed by Daducci et al. (2015).

Both models require a multi-shell acquisition sequence to be estimated. BTractApp will allow the user to select the microstructural analyses prior to starting processing; if any of the two analyses have been selected, it will then check the data acquisition scheme and stop execution with an error if the scheme is not multi-shell.

3.3.1   Diffusion Kurtosis Imaging

Kurtosis is a mathematical quantity which measures how much a given probability distribution differs from the Gaussian curve: a positive kurtosis corresponds to a distribution with fatter tails and a more peaked shape than a Gaussian, while a negative kurtosis describes a distribution with thinner tails and a lower, flatter top. This concept can be translated into diffusion imaging to study how the presence of barriers and compartments in the brain (e.g. cell membranes, separation into intracellular and extracellular spaces, etc.) alters the diffusion of the water molecules so that it is no longer precisely Gaussian. The characterization of the difference between the actual diffusion probability density function and perfect Gaussian diffusion can be useful to characterize brain tissue both in health and pathology [Jensen and Helpern (2010)]. As with diffusion, DKI can compute the mean kurtosis in a voxel (MK) and axial and radial kurtosis (AK and RK), defined as the kurtosis along the main diffusion direction (major eigenvector of the diffusion tensor) and the mean of the kurtosis along the other two minor eigenvectors, respectively.

The analysis of DKI parameters is especially interesting in the neonatal and developmental stages of the brain, to study the maturation of different areas of the brain and how this can be influenced and modified by pathology. Paydar and colleagues [Paydar et al. (2014)], in an analysis of the brains of children between 0 and 2 years of age, showed that mean kurtosis detects significant microstructural changes consistent with known patterns of brain maturation in both WM and GM, past the plateau reached by classical FA measures around 2 years of age which is commonly taken as the end of the brain myelination period.

The toolbox integrated in BTractApp for kurtosis analysis is DKE (version 2.6). The software can be run as a command line script, providing it with a configuration text file containing all the parameters and paths for the data to be processed. BTractApp provides a GUI to set the parameters' values, automatically creates the appropriate configuration file - selecting the preprocessed DWI data as input - and feeds it to the DKE script. The kurtosis maps are estimated and placed in a folder called `kurtosisData`, in the subject's original folder.

3.3.2 Neurite Orientation Dispersion and Density Imaging

The NODDI model [Zhang et al. (2012)] describes the overall diffusion in a voxel as composed of diffusion patterns from three separate components: an intracellular compartment, an extracellular compartment, and an isotropic component. From the diffusion in these compartments, NODDI estimates three output parameters: intracellular volume fraction (ICVF), orientation dispersion index (ODI) and extracellular (or isotropic) volume fraction (ISOVF). In particular, ICVF and OD model the microstructural components of the FA index from the classical DTI model: axonal packing density and variation in the main diffusion orientation in a voxel. A variation in one of these two indices can cause modifications in the FA value computed by DTI: the NODDI model allows to discriminate the two parameters for a more precise investigation of microstructural WM changes.

The computation of NODDI parameters has been integrated in BTractApp using the AMICO framework. The framework is written in Python, and thus its integration in the BTractApp code was straightforward: the software uses the AMICO functions in order to compute NODDI parametric maps for the preprocessed DWI data. The parameters for the NODDI model can be set in BTractApp's configuration file, or selected from the GUI. The software will compute all three of the parametric maps (ICVF, ODI and ISOVF), in Nifti compressed format (`.nii.gz`) and will save them in a folder called `AMICO` in the subject's original folder.

Part I

Relationship between network-level structural and functional connectivity in the healthy adult

Chapter 4

Correlation of network-level structural and functional connectivity in healthy adults

4.1 Introduction

The aim of this first part of the work was to investigate the relationship between structural and functional connectivity in the healthy adult brain.

Healthy adult data is often used as 'baseline' data to test and apply any processing or analysis method in brain imaging. This is often done in order to provide a description of the structure and function of the brain in a normal state, both to create an atlas for reference and to improve diagnostic accuracy [Job et al. (2017)]. We chose to first analyse the relationship between structural and functional connectivity in the adult brain not only for this reason, but also because healthy adult data poses less challenges than other types of data, such as paediatric or pathological data.

The novelty of this part of the work is due to the method through which functional connectivity is estimated: stereo-electroencephalography (SEEG), a technique in which the neural activity is registered using intra-cerebral electrodes directly implanted in the patient's brain. This technique is commonly used in patients who suffer from drug-resistant epilepsy, but not on healthy subjects due to its invasiveness. SEEG presents a higher resolution than fMRI and MEG and directly records electrical activity in the brain. In this study, we used data from SEEG recordings of epileptic patients to compute the functional connections between regions of the brain: in order to be able to study only the 'healthy' brain activity recorded by

these electrodes, all non-typical brain activity present in the recorded signals was removed, so that only typical, 'healthy' functional data was used to infer connectivity. This allowed us to compare the functional connectivity thus obtained with structural connectivity from healthy subjects, and to infer information about the relationship between these two 'modalities' of brain connectivity in the healthy adult.

In this work, we wanted to investigate how structural and functional connectivity are related not only at the single-edge level, but at different levels of network granularity, from global similarity to community structure to single-node and edge correlation. Studies have shown that even when there is only a small edge-to-edge correlation between structural and functional networks, nonetheless significant relationships between structural and functional network patterns can emerge through indirect, network-level interactions [Mišić et al. (2016)]. A global, edge-to-edge correlation analysis can thus be insufficient to understand the interaction between brain structure and function. We chose to study node-level connectivity to understand whether the relationship between structural and functional connectivity varies for different nodes or is constant across the brain, and whether there are specific brain regions which present more similar connectivity patterns than others. We also chose to investigate community structure in both network types and how the optimal communities are related between structural and functional networks. Finally, we analysed the weights distribution for both structural and functional networks to study how well it was approximated by different known distributions, in particular the power-law and log-normal distributions, which have been found by several works to well approximate neuronal connectivity [Buzsáki and Mizuseki (2014)].

4.2 Materials and Methods

4.2.1 Diffusion-weighted data and structural connectivity

The diffusion-weighted data we used to compute the structural connectivity was part of the WU-Minn HCP Data Release of the Human Connectome Project (https://www. humanconnectome.org/study/hcp-young-adult). This HCP data release includes high-resolution 3T MR scans from young healthy adult (age range 22-35 years). We selected 57 subjects (26 men) from the release and, for each subject, downloaded: pre-processed DWI data acquired at 3T and pre-processed T1 anatomical data registered to the DWI volume; two parcellations of the subject's brain into cortical and subcortical regions, obtained with Freesurfer using the Desikan and the Destrieux atlases [Desikan et al. (2006); Destrieux et al. (2010)]; and

a binary brain mask separating the subject's brain from the background. Details about the acquisition parameters and the pre-processing steps applied on the released data can be found in the relevant paper by Sotiropoulos et al. (2013).

Constrained spherical deconvolution and probabilistic tractography were performed on the pre-processed diffusion-weighted images by using the MRtrix3 package [Tournier et al. (2012)]. For each subject, a whole-brain tractography consisting of 50 million streamlines was generated, by using the Anatomically Constrained Tractography framework (ACT) [Smith et al. (2012)]. The seeds used for generating streamlines were distributed uniformly in the grey/white matter interface. The tractograms were filtered by using the Spherical deconvolution Informed Filtering of Tractograms (SIFT) [Smith et al. (2013)], and the final result consisted of 5 million streamlines for each subject.

In order to study how much the correlation between structural and functional connectivity is dependent from the choice of parcellation scheme, we chose to use three different brain parcellations, with different numbers of parcels: the Desikan scheme [Desikan et al. (2006)], the Schaefer scheme [Schaefer et al. (2017)] and the Destrieux scheme [Destrieux et al. (2010)]. The Desikan and Destrieux parcellations are included in the Freesurfer toolbox (https://surfer.nmr.mgh.harvard.edu) and are composed of 68 and 148 cortical parcels respectively. Subject-specific parcellations obtained with these schemes are included in the HCP data release and were downloaded for each of the subjects used for the SC computation.

The Schaefer parcellation is a multi-resolution scheme, based on the subdivision of the brain cortex into seven functional networks defined by Yeo et al. (2011): different sub-parcellations of the main scheme exist, with 100, 200, 400, 600, 800 and 1000 parcels. For this work, we chose to use only the coarsest parcellation scheme, composed by 100 parcels, which we will indicate simply as 'Schaefer' in the following. This parcellation was not included in the HCP processing pipeline, and thus subject-specific parcellations with this scheme were not present. In order to obtain them, we downloaded the `.annot` files specific for the parcellation from the group's GitHub (https://github.com/ThomasYeoLab/CBIG/tree/master/stable_projects/brain_parcellation/Schaefer2018_LocalGlobal), together with the surface data of Freesurfer's `fsaverage6` subject. From the `fsaverage6` surfaces and the Schaefer annotation files, we projected the parcellation onto each HCP subject's surface data using the command `mri_surf2surf` from Freesurfer, thus creating two Schaefer annotation files for each HCP subject (left and right hemisphere). We then re-projected the annotation files onto a volume in subject-specific space using the command `mri_aparc2aseg`. This produced, for each subject, a volume labelled with the Schaefer labels, plus the labels referring to Freesurfer's `aseg` parcellation of the subcortical areas. Finally, from this volume

we removed the subcortical labels, maintaining only the cortical areas which we used for the computation of the structural connectivity matrices.

For each subject's tractogram we obtained three structural connectivity matrices, one for each parcellation scheme, with the `tck2connectome` command of the MRtrix3 toolbox. The computed matrices were symmetric, and the diagonal (representing self-connections) was set to zero; the weight of each edge was taken to be the number of tractogram streamlines connecting the corresponding brain parcels.

4.2.2   SEEG data and functional connectivity

For a detailed description of the functional data acquisition and processing, see Arnulfo et al. (2018). SEEG data was recorded from 67 subjects affected by drug resistant focal epilepsy. We acquired mono-polar local field potentials (LFPs) from brain tissue with platinum–iridium, multi-lead electrodes, with shared reference in the WM far from the putative epileptic zone. We acquired an average of 10 minutes of uninterrupted spontaneous activity with eyes closed with a 192-channel SEEG amplifier system (NIHON-KOHDEN NEUROFAX-110) at a sampling rate of 1 kHz. Before electrode implantation, the subjects gave written informed consent for participation in research studies and for publication of their data.

We excluded electrode contacts (1.3 ± 1.2, range 0-10) that demonstrated non-physiological activity from analyses. We employed a referencing scheme where electrodes in GM were referenced by the contacts located in the closest WM [Logothetis et al. (2012)], which was proven optimal for preserving phase relationship between SEEG contact data [Logothetis et al. (2012)]. Since one same WM contact can be used for referencing multiple cortical contacts, we rejected derivations with shared reference. The final number of channels analysed was on average 110 ± 25 for each subject and 7491 in total.

Prior to the main analysis, SEEG time series were filtered with 18 Finite Impulse Response (FIR) band pass filters with central frequency ranging from 2.50 to 320Hz. We excluded all 50Hz line-noise harmonics using a band-stop equiripple FIR filter with 1% of maximal band-pass ripples and 3 up to 8Hz width for the stop band parameters.

Due to possible filtering artefacts around epileptic spikes and the resultant increase in synchrony, we discard periods of 500ms containing Interictal Epileptic Events. We defined such periods as the temporal windows where at least 10% of cortical contacts demonstrated abnormal concurrent sharp peaks in more than half of the 18 frequency bands. Such episodes were excluded from within- and cross-frequency synchrony analysis.

We estimated inter-areal phase-phase interactions at individual subject level using the Phase Locking Value (PLV) [Ray et al. (2008)]. Finally, for each parcellation scheme, we morphed individual contact-PLV values via the median operation, separately for each frequency, to group-level inter-regional PLV matrices where regions were the parcels from the selected atlas. During this 'morphing' step, we excludes from the computation of the median all contact-PLV values which were not present in at least 3 subjects, and which were not sampled at least 20 times in total. This was done in order to remove from the matrices computation contact-PLV values which were sampled only a small amount of times, and might thus be due to noise or artefacts in the registrations.

4.2.3 Network analysis

At a global level, we analysed the average SC and FC connectivity matrices obtained by averaging over all subjects, thus producing a single SC average matrix and 18 average FC matrices, one for each acquisition frequency. We then computed Pearson's correlation coefficient between the average SC matrix and every FC average, for all three parcellation schemes.

SC edge weights were computed by counting the number of streamlines between two brain parcels, and thus SC edge weights equal to zero indicated the absence of any physical connection between the corresponding regions. In FC matrices, however, edge weights were obtained as measures of correlation between electrical activities of brain areas, which are never perfectly equal to zero. The zero value had thus a 'filler' function in FC matrices: if a FC edge had a value of zero, this indicates that the correlation between the corresponding two brain areas could not be computed, because of the specific electrode distribution in the patient. For this reason, in all the global analyses described in the following, we considered only edges which were non-zero in FC matrices, masking the SC matrices accordingly before computation of Pearson's correlation.

To assess the statistical significance of the correlation, we computed Pearson's correlation between randomly rewired SC and FC matrices, obtained using the `null_model_und_sign` function from the BCT, which randomly rewires graphs maintaining weight, degree and strength distributions.

We computed the same Pearson's correlation coefficient between the average SC connectivity matrix and 500 bootstrapped average FC matrices, obtained by randomly resampling the FC subjects pool with replacement, to select 67 FC matrices used to compute new bootstrapped averages for all frequencies. These bootstrapped matrices were compared with the

original SC matrix, and we computed 95% confidence intervals from the results of these comparisons.

In order to study how correlation varies at different network densities, we selected the FC acquisition frequency which produced the highest correlation value for all parcellation schemes (14.14 Hz) and we studied how this correlation varies when only part of the edges is present. The SC and FC matrices were thresholded so that only the edges with weight greater than a given percentile were retained, and the global analysis described above was repeated on these thresholded matrices. This was done for a range of percentile values from 10 to 90, with a step of 10, giving nine pairs of SC and FC matrices with decreasing density. The computation of confidence intervals over bootstrapped FC averages and the analysis over rewired matrices was also repeated.

From this first comparison, we found that the Schaefer parcellation scheme is the one for which the correlation is highest, for all FC frequencies: for the following analyses, we limited ourselves to this specific parcellation scheme.

Comparison with log-normal distribution

The log-normal distribution and other skewed, heavy-tailed distributions - such as the power-law distribution - are often found in biological organisms and processes, especially in the brain [Buzsáki and Mizuseki (2014); Sporns (2013)]. Checking the distribution of the measured data against such models can help confirm the data is significant, well-distributed and responding to known properties. We chose to study the weight distributions for SC and FC in order to compare them with these well-known models and estimate the goodness of their fit. First we plotted the decimal logarithm of the SC and FC edge weights, sorted in descending order, to visualize the shape of the distribution. We then fitted both SC and FC data at all acquisition frequencies with four different distributions: power law, truncated power law, exponential and log-normal. For each distribution fitting, we first computed the maximum likelihood estimate (MLE), which is the estimated set of parameters which maximizes the fit of the given distribution to the data.

To estimate the goodness of each fit, we computed three quantities: the Akaike information criterion (AIC), the Bayesian information criterion (BIC) and the Root Mean Square error (RMS). The AIC is a means for model selection which estimates the quality of the fit of a model with respect to other models, and was defined by Akaike (1974) as:

$$AIC = 2k - 2\ln(\hat{L}) \tag{4.1}$$

where k is the number of estimated parameters in the model and $\hat{L}$ is the maximum of its likelihood function. Given a set of candidate models for fitting the data, a smaller AIC value indicates the preferred model. The BIC is similar to the AIC, but with a penalization term for the number of parameters defined as $ln(n)k$, while in the AIC it is $2k$. Finally, the RMS is a measure of accuracy for a fitting and is defined as the square root of the second sample moment of the differences between predicted values and observed values.

Parcel-wise analysis

We analysed parcel-wise correlation by comparing a node's SC pattern (i-th row of the SC matrix for node i) with the corresponding FC pattern (matrix row). We computed a Pearson correlation value between SC and FC for each node at each FC frequency, thus obtaining a 100×18 matrix where rows represented nodes and columns represented FC frequencies. Each value quantified how the SC pattern of a given node correlated with the corresponding FC pattern at a given frequency.

To analyse how parcel-wise correlation varied with FC frequency, we computed the covariance matrix of the 100×18 matrix obtained in the previous step: the result was an 18×18 matrix M, in which each element M_{ij} represented how the correlation pattern of all nodes at frequency i varied with respect to the correlation pattern at frequency j. From this matrix, we obtained a clusterization of FC frequencies with respect to their covariance, applying a k-means clusterization on the matrix with $k = 4$, based on the covariance matrix. From the clustering, we found four FC frequencies ranges inside which the correlation between SC and FC varied in a similar way: $[2.5 - 9.99]$ Hz, $[14.14 - 28.28]$ Hz, $[39.99 - 159.99]$ Hz and $[190.27 - 319.99]$ Hz. We then recomputed parcel-wise correlation coefficients, this time from the four average FC matrices obtained by averaging FC matrices of frequencies in the same cluster.

Modularity analysis

We used the Leiden community detection algorithm [Traag et al. (2018)] to subdivide the SC and FC matrices in communities and compute the modularity value of these partitions. We analysed separately left and right hemisphere connections, for several reasons: first, inter-hemispheric coverage in FC SEEG acquisitions is very poor, and the electrode implants are quite different from left to right hemisphere, producing uneven sampling between the hemispheres. Moreover, the two hemispheres have different functional roles, which might influence their module organization and thus the results of a joint analysis. Lastly, the

Schaefer parcellation scheme is not perfectly symmetrical, presenting some parcels in one hemisphere which are not present in the other; to obtain a more precise study of each hemisphere's organization, we chose to separate the data from left and right in the modularity analysis.

For the partition of the networks into communities, we chose to use the Leiden algorithm instead of the widely used Louvain one [Blondel et al. (2008)] because the Leiden algorithm has been shown to uncover better partitions than the Louvain one, while also being faster. The Leiden algorithm is made available as a Java package (https://github.com/CWTSLeiden/networkanalysis) and, among other parameters, requires the definition of a 'resolution' parameter for the quality function to be optimized, which can be either the constant Potts model or the modularity. We chose the modularity as our quality function and studied the behaviour of each network's community structure when the resolution parameter (γ) varies. To do this, we applied the modularity analysis with different values of γ, starting from 0.8 and ending at 2.3 with increments of 0.1. The default value for γ is 1, for both Louvain and Leiden methods; smaller values tend to detect bigger modules, while higher values detect smaller modules. For each value of γ we computed a consensus partition of the network and its modularity value, which varies between 0 and 1 and measures the 'goodness' of the partition: partitions with modularity close to 1 have dense connections between nodes in the same module, and sparse connections between nodes in different modules, indicating optimal interconnection of nodes inside modules and optimal inter-module separation.

To obtain a single 'consensus' partition of each SC and FC networks, we applied the Leiden algorithm to 500 bootstrapped averages for the SC matrix and the FC matrix at each frequency. The partitions obtained for the bootstrapped averages were then combined with a consensus clustering approach [Lancichinetti and Fortunato (2012)]. Each partition is represented as a binary square matrix, where each element is set to 1 or 0 depending respectively on whether the corresponding nodes are in the same module or not. This is done to eliminate the arbitrary numbering of modules from the representation, thus making the partitions directly comparable to each other. The set of matrices is then averaged across the repetitions to obtain a matrix with values close to 1 when the respective pair of nodes frequently co-occurred in the same module across the set and values close to 0 when the respective pair of nodes rarely co-occurred in the same module. The resulting co-occurrences matrix is a weighted network, which is then used again as input to the Leiden method to compute a final consensus partition scheme. We then computed the modularity value for the obtained consensus scheme at each given γ value, hemisphere and connectivity (SC or FC at each frequency).

4.3   Results

4.3.1   Structural and functional average matrices show the same global structure

The average connectome matrices for SC and FC (Schaefer parcellation scheme), with the corresponding standard deviations, are shown in Figure 4.1. The matrices were averaged over all subjects; for FC, the average was computed separately for each acquisition frequency. We chose to show the average matrix with a frequency of 14.14 Hz, since this frequency produced the highest correlation with SC connectivity for all parcellations; we selected the Schaefer parcellation because it was the scheme for which we obtained the highest correlation coefficients for all FC frequencies (see Figure 4.2a).

4.3.2   Global Pearson correlation coefficient shows positive correlation between average structural and functional networks

In Figure 4.2a we show that the Pearson correlation coefficient between global average SC and FC matrices has a peak at FC frequency of 14.14 Hz, for all three parcellation schemes. The Schaefer parcellation scheme was the one for which the correlation was always greater than for the other two schemes, for all FC frequencies; the parcellation scheme with the lowest correlation across frequencies was the Destrieux one. The maximum correlation value was 0.56 for the Schaefer parcellation, 0.51 for the Desikan and 0.46 for the Destrieux scheme (all $p < 0.05$, Pearson correlation test). The correlation coefficients obtained from randomly rewired matrices are very close to zero, which further shows that the correlation found in the original data is significant.

The Pearson correlation coefficient computed between the average SC matrix and the average FC at 14.14 Hz did not vary significantly for different values of density thresholding (Figure 4.2b). The matrices were thresholded by removing the weaker edges to retain from 90% to 10% of the edges, and the global correlation analysis was repeated on these nine pairs of networks. We found that the correlation coefficient remains almost constant at varying network densities, decreasing slightly just for networks containing the strongest 10% edges. The comparison of average SC with randomly rewired average FC matrices produces again correlation values very close to zero, confirming that the correlation of original data is significant.

In Figure 4.2c we plot the strongest 30% SC weights against the strongest 30% FC weights at 14.14 Hz, on a decimal logarithmic scale, for all parcellation schemes. By
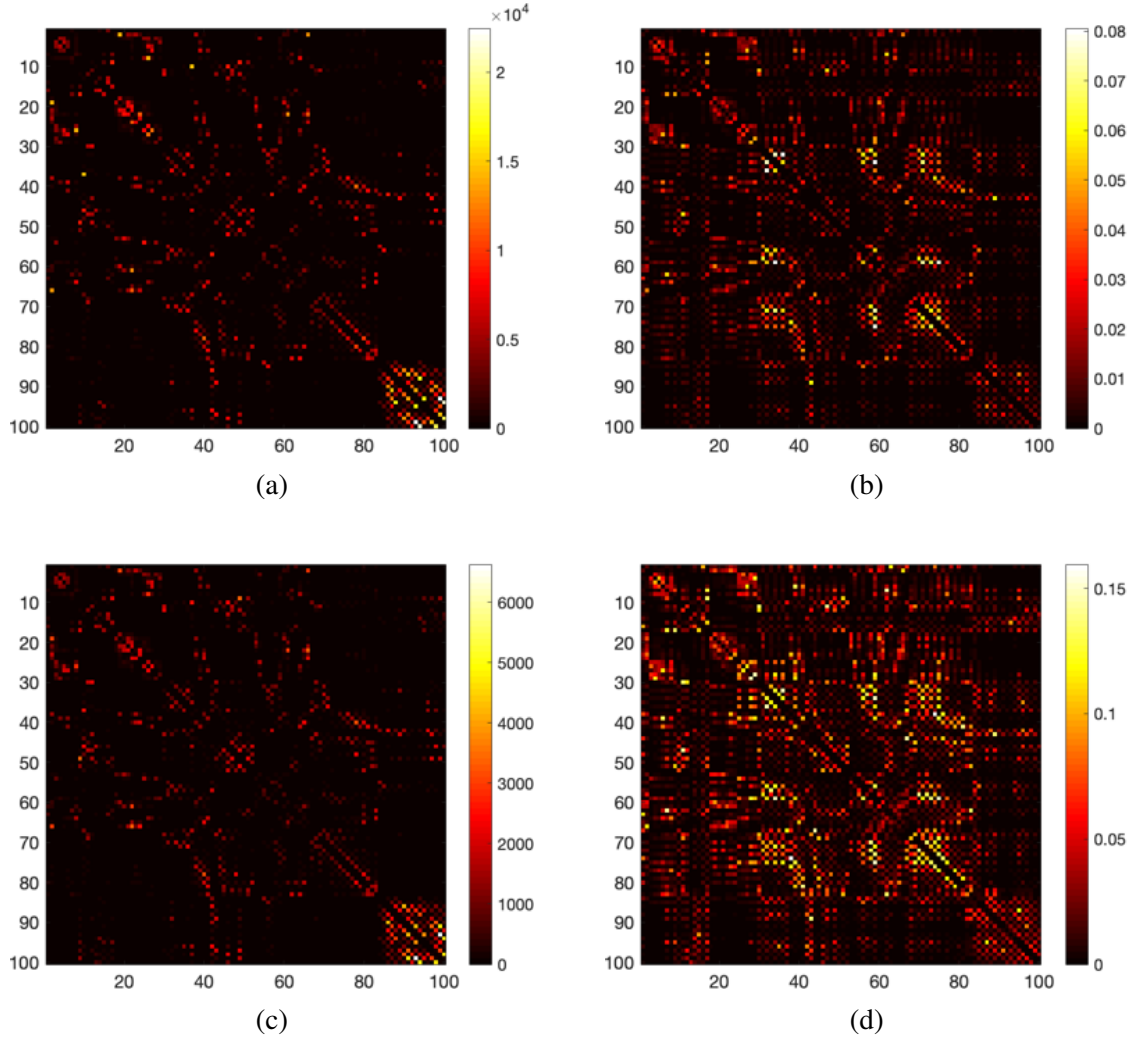
Figure 4.1 Average SC (a) and FC (b) matrices and corresponding standard deviations ((c) and (d)). The average FC matrix shown in this Figure has an acquisition frequency of 14.14 Hz, since this frequency resulted to be the one which better correlates with the average SC connectivity (see Figure 4.2a).

analysing the weights' distribution, we can determine that the data support the correlation computed in the previous analysis, without outlier data which could drive the correlation.

4.3.3 Structural and functional weights follow log-normal distribution

In Figure 4.3 we summarise the results of the comparison between edge weights distribution for SC and FC and log-normal distribution. The decimal logarithms of the sorted edge weights for SC and FC, plotted in Figures 4.3a and 4.3b, show that the shape of the weights distributions reflects a log-normal distribution.

The results of the fitting of SC and FC weights with four different distributions are shown in Table 4.3c and Figure 4.3d. In Table 4.3c, bolded values indicate the minimum of the AIC and the RMS, showing that the best fit among the four distributions was found for the power-law and log-normal distributions. In Figure 4.3d we plotted the four quantities computed for each fitting across FC frequencies; again, the fittings which produced the smallest AIC and RMS are the power-law and the log-normal distributions.

4.3.4 Functional node weights show high variability in right temporal lobe, structural variability focused in optical region

The average and standard deviation of the node strength for SC and FC data, plotted in Figure 4.4, show a high average and variability in functional strengths localised in the right temporal lobe, while for the structural weights only few nodes localised in the optical region show a high strength and a high variability. Again, the FC acquisition frequency of 14.14 Hz was chosen because of its high correlation with SC connectivity (see Figure 4.2a). The high node strength and variability for FC in the right temporal lobe may be caused by the uneven sampling of the two hemispheres: as is often the case, the patients' right hemispheres presented more electrodes than the left, due to the higher presence of eloquent cortex in the left hemisphere and thus the higher risk of functional damage for implants in the left hemisphere. With respect to SC node strength, slightly higher variability is found in nodes in the optical region of the brain.

4.3.5 Spatial variability in node-wise Pearson's correlation shows variability in correlation between SC and FC at different brain locations

We used Pearson's correlation coefficient to compare the SC and FC connectivity patterns of each single node, obtaining a 100×18 matrix of node-wise correlation coefficients (Figure 4.5a). Each row of the matrix represents a parcellation node, and each column is a FC acquisition frequency. The value (i, j) is the Pearson correlation coefficient of the SC connectivity pattern for node i (namely the i-th SC matrix row) with the FC connectivity pattern for the same node at frequency j (j-th FC matrix row). This allowed to analyse how single nodes' connectivity patterns varied across FC frequencies.

We found that the correlation between SC and FC could vary significantly across nodes, with few nodes showing very low correlation coefficients (minimum coefficient 0.25) and

other nodes - localised mainly in the regions comprised in the Default Mode Network [Greicius et al. (2003)] - presenting very high correlation values (maximum coefficient 0.97). We also found that the correlation variation seemed to identify ranges of FC frequencies across which the node-level correlation patterns were similar. For this reason, we chose to further investigate the covariance of node connectivity patterns across frequencies, in order to reduce the dimensionality of the FC data from 18 frequencies to a smaller number of 'frequency ranges' across which SC-FC correlation was coherent.

The covariance matrix obtained by computing Pearson's correlation coefficients between parcel-wise correlation patterns at different pairs of frequencies is shown in Figure 4.5b. Both rows and columns represent FC frequencies; the values represent the correlation coefficients computed on the matrix in Figure 4.5a, where rows (nodes) are variables and columns (frequencies) are observations. We found that the frequencies can be grouped together with respect to their correlation coefficients, obtaining ranges of frequencies where parcel-wise correlation patterns vary in a very similar way.

We applied a k-means algorithm ($k = 4$) on the covariance matrix to compute these groups, obtaining four ranges of frequencies with similarly varying correlation patterns: $[2.5 - 9.99]$ Hz, $[14.14 - 28.28]$ Hz, $[39.99 - 159.99]$ Hz and $[190.27 - 319.99]$ Hz. We then recomputed parcel-wise correlation coefficients as done for Figure 4.5a correlating SC data with four FC matrices obtained by averaging FC data across the four frequency ranges. The results of this last analysis are reported in Figure 4.5c, where rows of the matrix represent nodes and columns represent the four frequency ranges. In Figures 4.5d and 4.5e we show parcel-wise correlation values for two of these ranges: respectively, range $[2.5 - 9.99]$ Hz, which gave the lowest average correlation value ($r = 0.717$), and range $[14.14 - 28.28]$ Hz, which gave the highest correlation value ($r = 0.787$).

4.3.6   Structural network strongly modular with few big communities, good correspondence with Yeo's functional subdivision

We show in Figure 4.6a how the modularity and the number of modules for the structural connectivity vary with different values of γ; the modularity has a maximum for values of γ close to 1, which produce a partition in five modules for both hemispheres.

The left and right partitions which produced the highest modularity values are shown in Figure 4.6b. Both partitions were composed of 5 modules: the left partition had a modularity value of 0.81 and corresponded to a γ value of 1, while the right partition had a modularity value of 0.74 and was obtained with $\gamma = 1.10$.

The Schaefer parcellation is based on the subdivision of the brain into seven functional subnetworks defined by Yeo et al. (2011): for this reason, we investigated also the SC partition schemes composed by seven modules, to compare them to the original seven functional subnetworks. For the left hemisphere, partitions with seven modules were obtained for all $\gamma \geq 2$; the one with the highest modularity value (0.66) corresponded to $\gamma = 2.3$. For the right hemisphere, partitions with seven modules were obtained for all $\gamma \geq 1.7$, and the highest modularity (0.68) was obtained with $\gamma = 2$. We show both partition schemes in Figure 4.6c: the white lines superimposed onto the brain's hemispheres represent the boundaries of Yeo's original parcellation. We found that the 7 modules obtained on the SC average matrix are well aligned with the boundaries defined by Yeo and colleagues.

4.3.7 Functional modularity lower than structural, fewer and bigger modules for maximum modularity

In Figure 4.7a we show the modularity values and the number of detected modules for partitions obtained with different combinations of FC acquisition frequency ranges (columns) and γ values (rows). The analysis was executed separately for left and right hemispheres.

The partitions which produced the highest modularity value for each hemisphere are shown in Figure 4.7b. The left partition (modularity 0.50) contained only two modules and was obtained on the FC acquisition range $[14.14 - 28.28]$ Hz and a γ value of 0.8, while the right partition (modularity 0.58) contained five modules and corresponds to a FC acquisition range $[2.5 - 9.99]$ Hz and $\gamma = 1.5$.

As done with the SC analysis, we considered also the partition with the highest modularity value among those comprised of seven modules, which we show in Figure 4.7c. For the left hemisphere, the highest modularity value among partitions with seven modules was 0.46, obtained on the averaged FC for range $[39.99 - 159.99]$ Hz and $\gamma = 2.1$. For the right hemisphere, the partition with seven modules and highest modularity (0.55) corresponded to an acquisition range of $[2.5 - 9.99]$ Hz and $\gamma = 2$. Again, the edges of the 7-module FC partitions align well with Yeo's boundaries.

4.3.8 Good correspondence between structural and functional community partitions

In order to compare the SC and FC modules, we used the `partition_distance` function from the BCT toolbox. This function computes, for a given pair of module partitions, the

normalized variation of information (*nVI*) and the normalized mutual information (*nMI*). These quantities are defined in Meilă (2007) as follows:

$$nVI = [H(X) + H(Y) - 2MI(X,Y)] \ / \ \log(n)$$

$$nMI = 2MI(X,Y) \ / \ [H(X) + H(Y)]$$

(4.2)

where *X* and *Y* are the two partitions, *H* is the entropy, *MI* is the mutual information and *n* is the number of nodes in the partitions. We compared SC partitions for varying γ with corresponding FC partitions for all γ and acquisition frequency; the results of the comparison are shown in Figure 4.8a, where the matrix rows represent γ values and the columns represent FC frequency ranges. The matrices on the left show the distribution of *nMI* values, while the matrices on the right show the *nVI* values; top matrices correspond to the analysis for the left hemisphere, while bottom matrices correspond to the right hemisphere.

The maximum value for the *nMI* indicator in the left hemisphere was 0.79. This corresponded to $\gamma = 2.1$ for SC and $\gamma = 1.3$ for FC. The FC frequency range for this partition was $[39.99 - 159.99]$ Hz, and both partitions were composed of 5 modules; the corresponding minimum value for the *nVI* indicator was 0.17. For the right hemisphere, the maximum *nMI* value was 0.73, corresponding to a SC partition with 7 modules and a FC partition with 6 modules ($\gamma = 2.3$, $[14.14 - 28.28]$ Hz) (Figures 4.8b and 4.8c). The corresponding minimum value for the *nVI* indicator was 0.25.

(a)

(b)

(c)
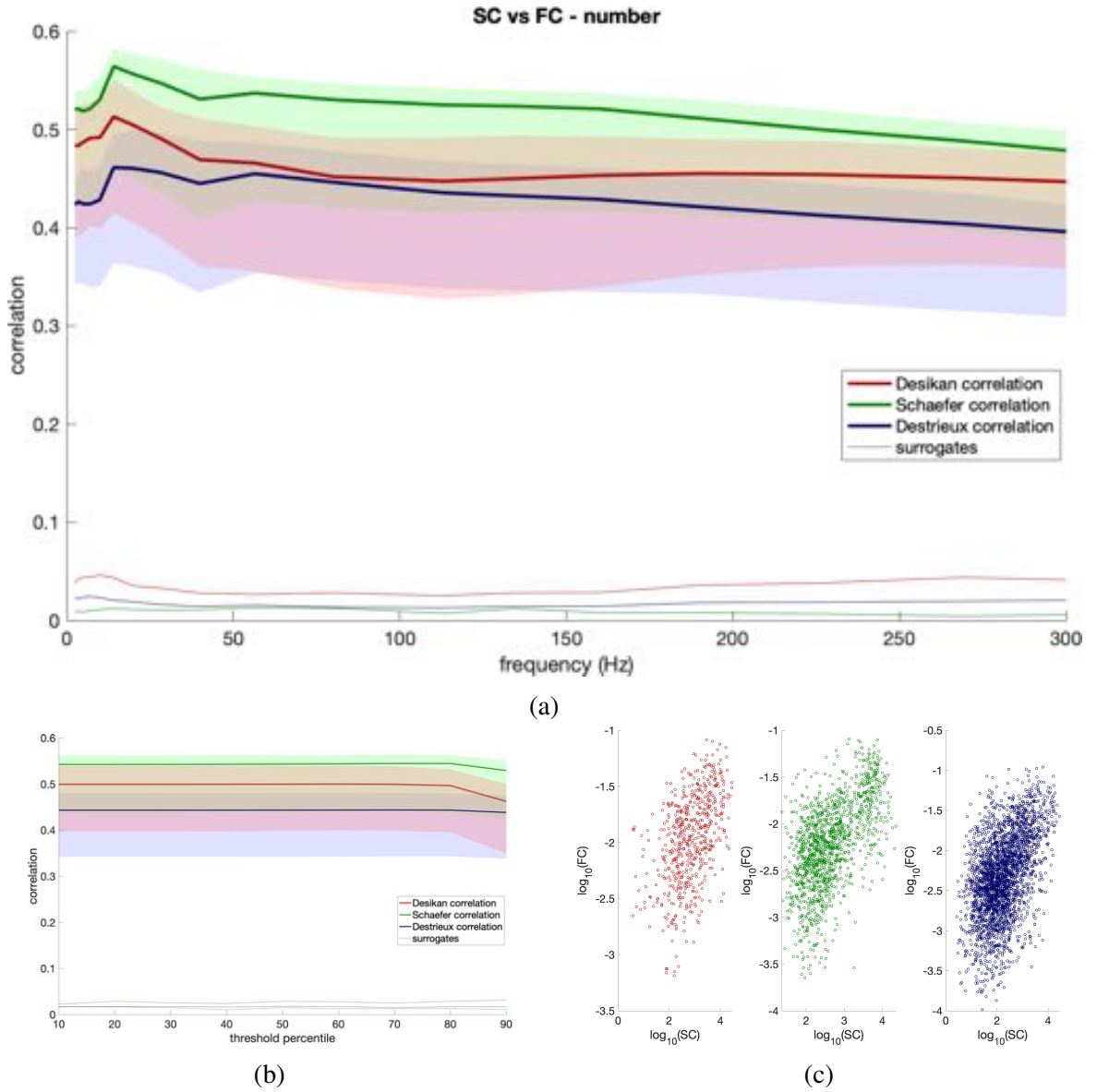
Figure 4.2 (a) Pearson's correlation coefficient (thick lines) between average SC and FC matrices, for the three parcellation schemes used: Desikan (red), Schaefer (green) and Destrieux (blue). 95% confidence intervals were computed from 500 bootstrapped FC averages and are shown as shaded areas around the main lines. Correlation of average SC matrix with randomly rewired average FC matrices is also reported (thin lines, same colours as the main lines). (b) Analysis of correlation at different network densities between average SC and FC matrices, with FC frequency 14.14 Hz. Thick lines and shaded areas represent the Pearson correlation and 95% confidence intervals over bootstrapped FC averages for the three parcellations, plotted over the percentile thresholds used; thin lines show the correlation of SC matrix with randomly rewired FC matrices, for the same density thresholds. (c) Scatter-plots of the decimal logarithm of average SC weights (*x*-axis) against decimal logarithm of average FC weights at 14.14 Hz (*y*-axis) for the three partition schemes. For all the global correlation analyses, only edges which were non-zero in the average FC matrices were considered.
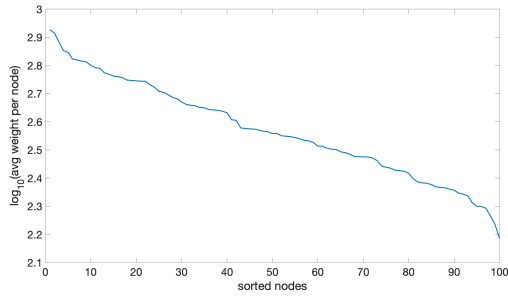
(a)
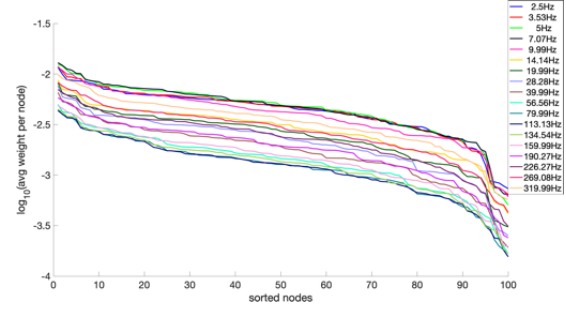
(b)

	pow	tpow	exp	log-normal
MLE	-27093	-26581	-33888	-26208
AIC	54189	53167	67778	**52419**
BIC	54195	53180	67785	52432
RMS	**0.533**	3.0764	84.7498	1.2993

(c)
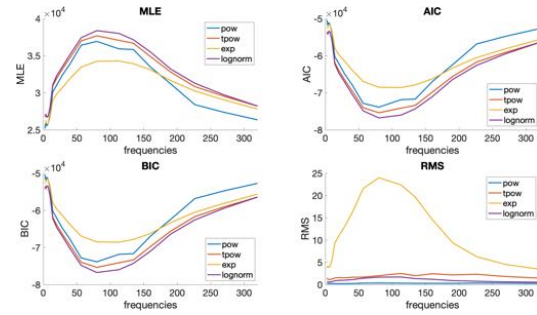
(d)

Figure 4.3 (a) Decimal logarithm of edge weights for the average SC matrix, sorted in descending order. (b) Decimal logarithm of edge weights for the average FC matrix at different acquisition frequencies, sorted in descending order. Figures (a) and (b) show that the weight distribution for both SC and FC at all frequencies is similar in shape to the log-normal distribution. (c) Maximum likelihood estimate (MLE), Akaike information criterion (AIC), Bayesian information criterion (BIC) and root mean square error (RMS) for the fitting of SC weights with four different distributions: power-law (pow), truncated power-law (tpow), exponential (exp) and log-normal. Bolded values represent the smallest AIC and RMS values, indicating goodness of fit. (d) Plot of Maximum likelihood estimate (MLE), Akaike information criterion (AIC), Bayesian information criterion (BIC) and root mean square error (RMS) for the fitting of FC weights at different frequencies with four different distributions: power-law (pow), truncated power-law (tpow), exponential (exp) and log-normal. The distribution which best fits the data is the one with smaller AIC and RMS: from the plot, these are the power-law and log-normal distributions.
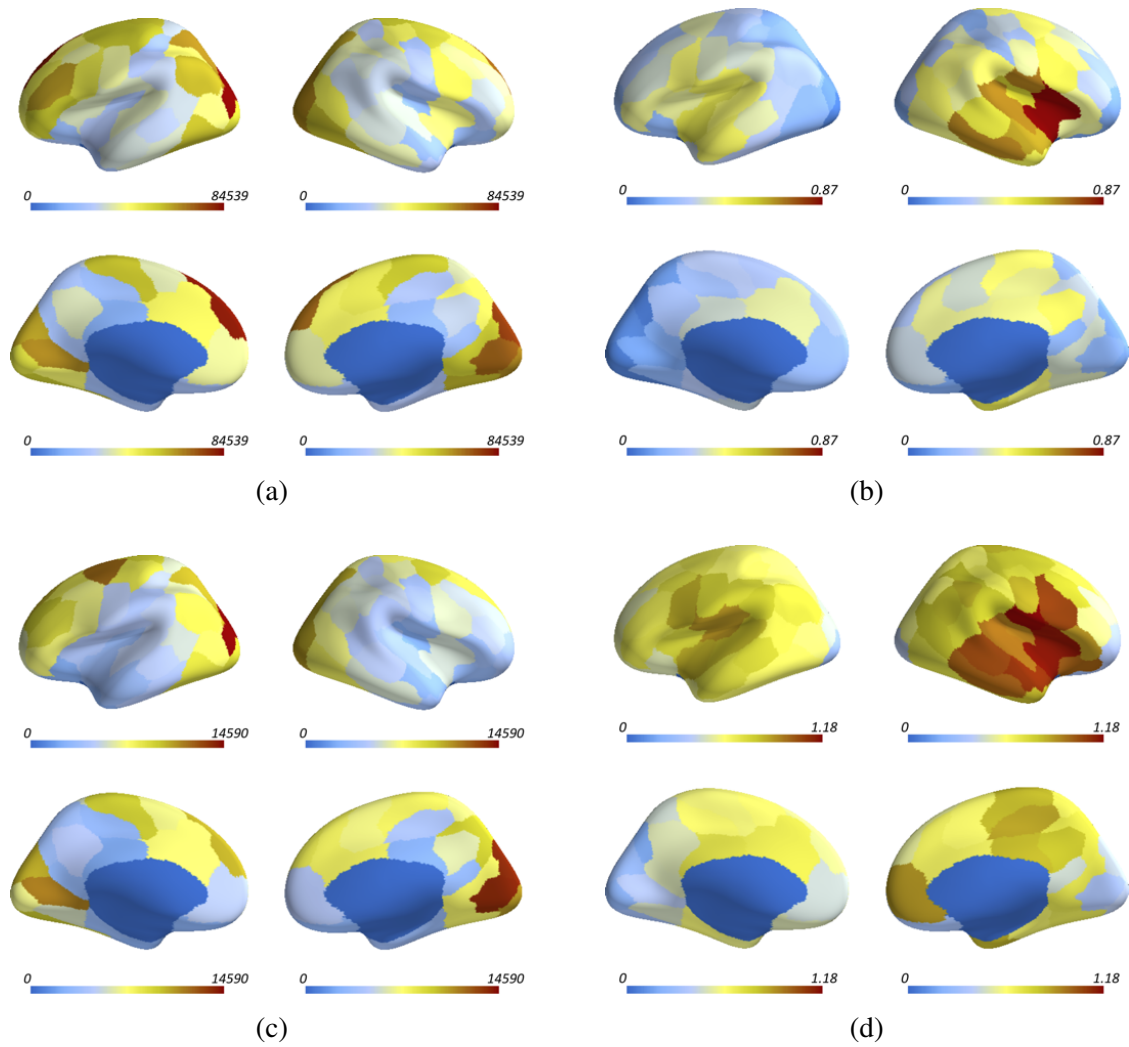
Figure 4.4 Average node strengths for SC (a) and FC (b) and relative standard deviations ((c) and (d)). For FC, we chose to show the data at 14.14 Hz, since this frequency resulted to be the one which better correlates with the average SC connectivity (see Figure 4.2a).
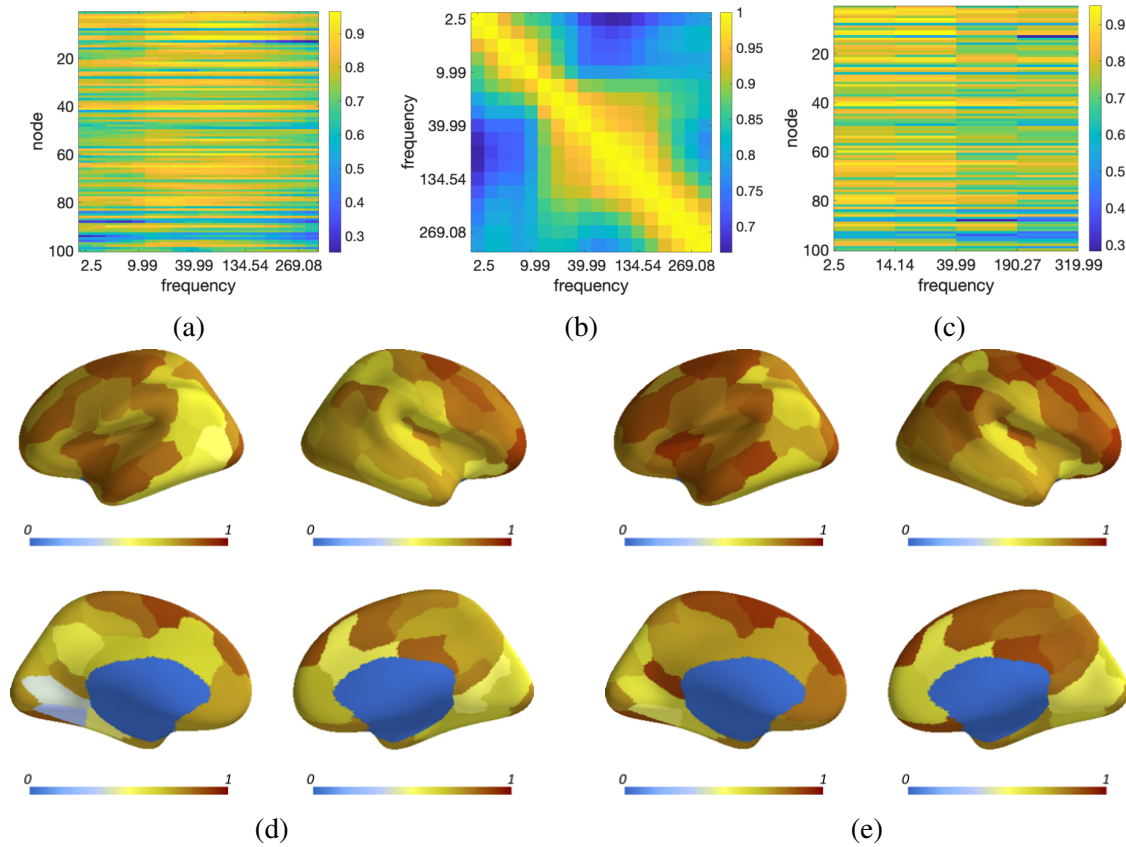
Figure 4.5 (a) Parcel-wise SC vs FC correlation matrix for all nodes (rows) and all frequencies (columns). (b) Covariance matrix for all FC frequencies. (c) Parcel-wise SC vs FC correlation for all nodes (rows) and four frequency clusters individuated form the covariance matrix, with the k-means algorithm ($k = 4$). (d) Parcel-wise correlation SC vs FC coefficients averaged over the first frequency cluster (range $[2.5 - 9.99]$ Hz), which produced the lowest average correlation coefficient ($r = 0.717$). (e) Parcel-wise correlation SC vs FC coefficients averaged over the second frequency cluster (range $[14.14 - 28.28]$ Hz), which produced the highest average correlation coefficient ($r = 0.787$).
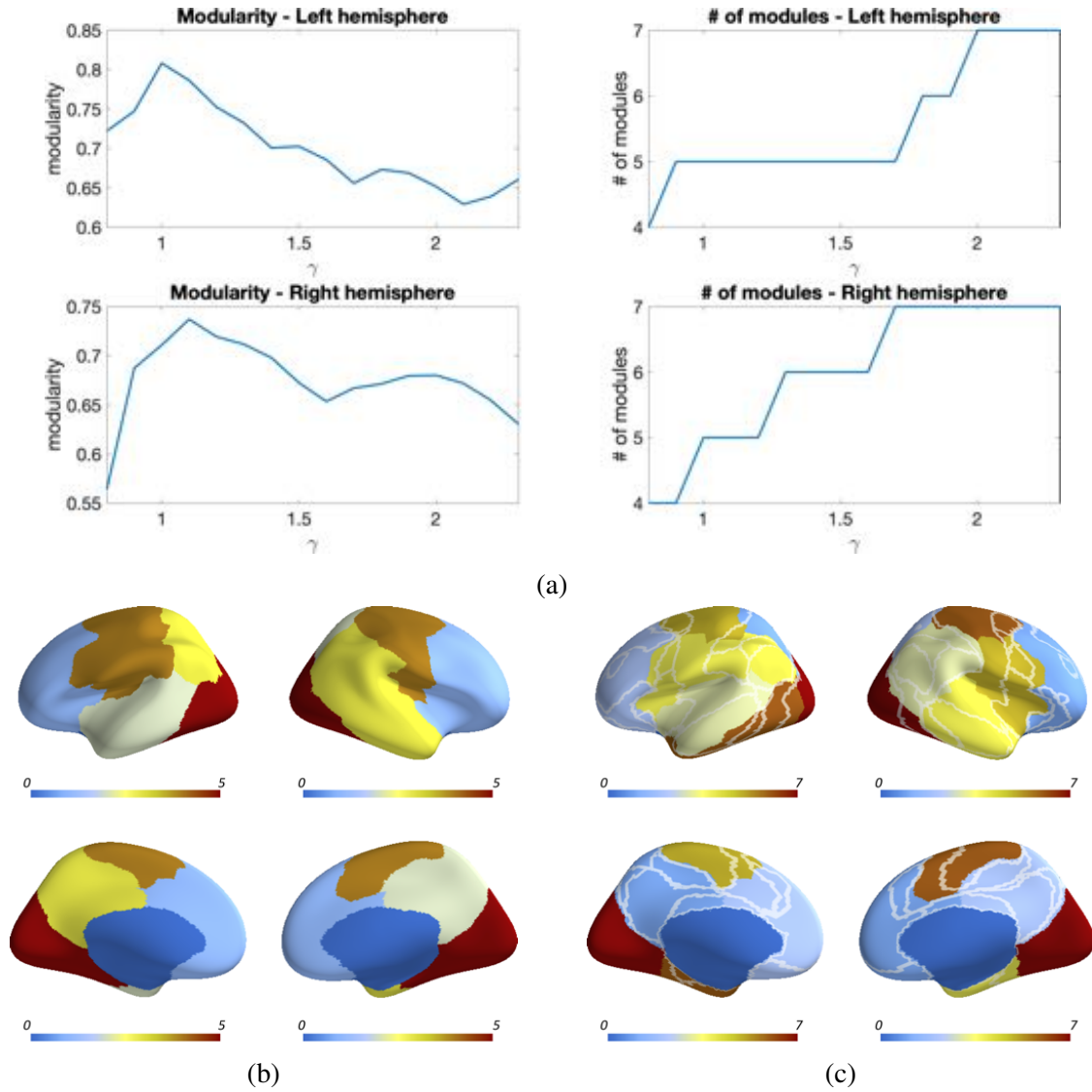
Figure 4.6 (a) Modularity values (left plots) and number of detected modules (right plots) against γ value for SC matrices, Schaefer parcellation. Computation was done separately for left (top plots) and right hemisphere (bottom plots). (b) SC partitions for left and right hemispheres which produced the highest modularity values (0.81 for the left hemisphere, 0.74 for the right hemisphere). The left partition was obtained with $\gamma = 1$, while the right partition with $\gamma = 1.10$. (c) SC partitions for left and right hemispheres which produced and the highest modularity values among the partitions comprised of seven modules (0.66 for the left hemisphere, 0.68 for the right hemisphere). The left partition was obtained with $\gamma = 2.3$, while the right partition with $\gamma = 2$. The white lines superimposed onto the brains represent the boundaries of Yeo's original parcellation.

(a)

(b)   (c)
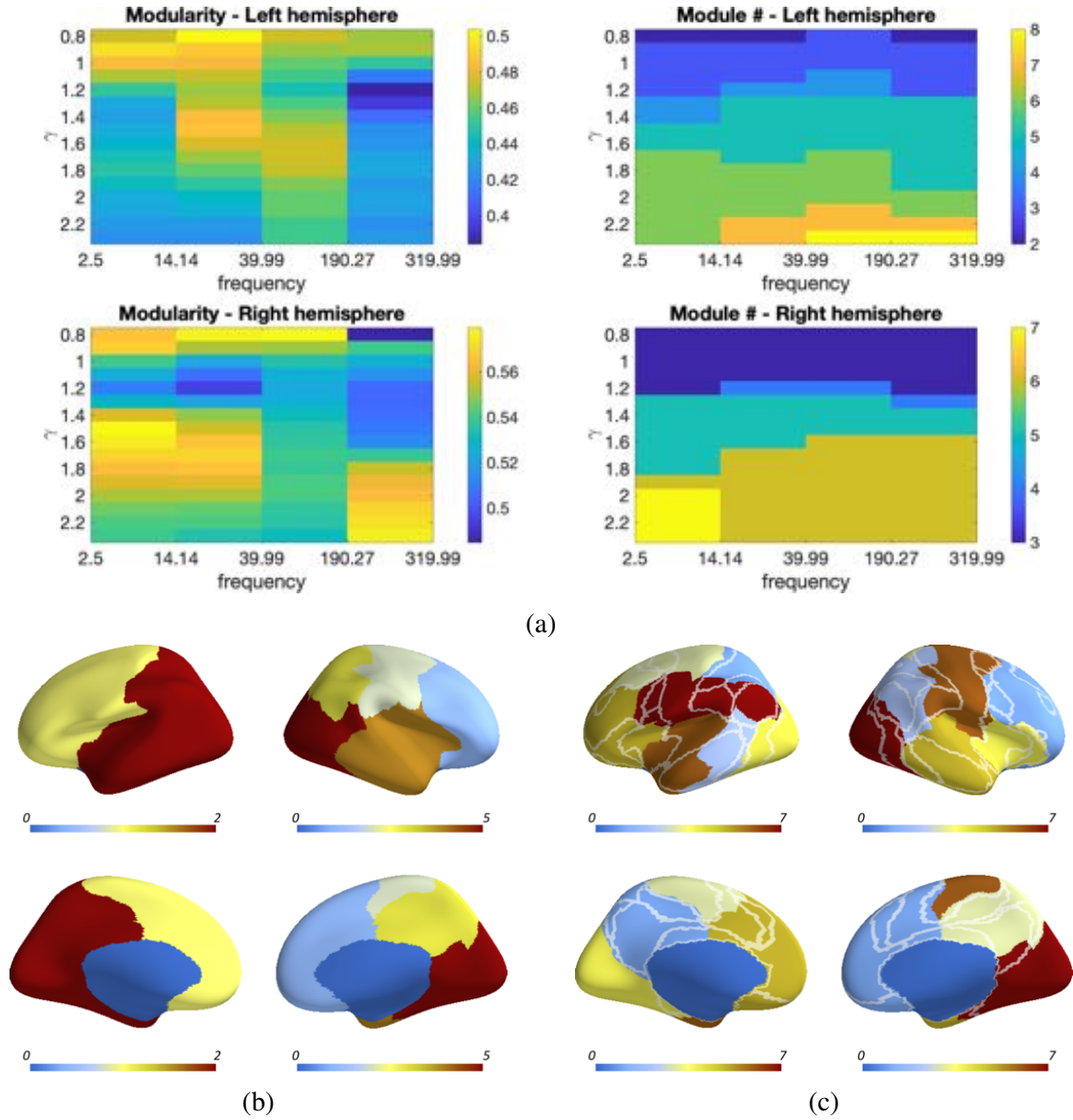
Figure 4.7 (a) Modularity values (left image) and number of detected modules (right image) against γ value for FC matrices, Schaefer parcellation. Computation was done separately for left (top plots) and right hemisphere (bottom plots). The matrices' rows represent different values of γ, while the columns represent FC acquisition ranges, as computed in Subsection 4.3.5. (b) FC partitions for left and right hemispheres which produced the highest modularity values (0.50 for the left hemisphere, 0.58 for the right hemisphere). The left partition was obtained with a FC averaged over the $[14.14 - 28.28]$ Hz range and with $\gamma = 0.8$, while the right partition with the $[2.5 - 9.99]$ Hz range and $\gamma = 1.5$. (c) FC partitions for left and right hemispheres which produced and the highest modularity values among the partitions comprised of seven modules (0.46 for the left hemisphere, 0.55 for the right hemisphere). The left partition corresponds to a FC acquisition range of $[39.99 - 159.99]$ Hz and $\gamma = 2.1$, while the right partition had a range of $[2.5 - 9.99]$ Hz and $\gamma = 2$. The white lines superimposed onto the brains represent the boundaries of Yeo's original parcellation.

(a)

(b)   (c)
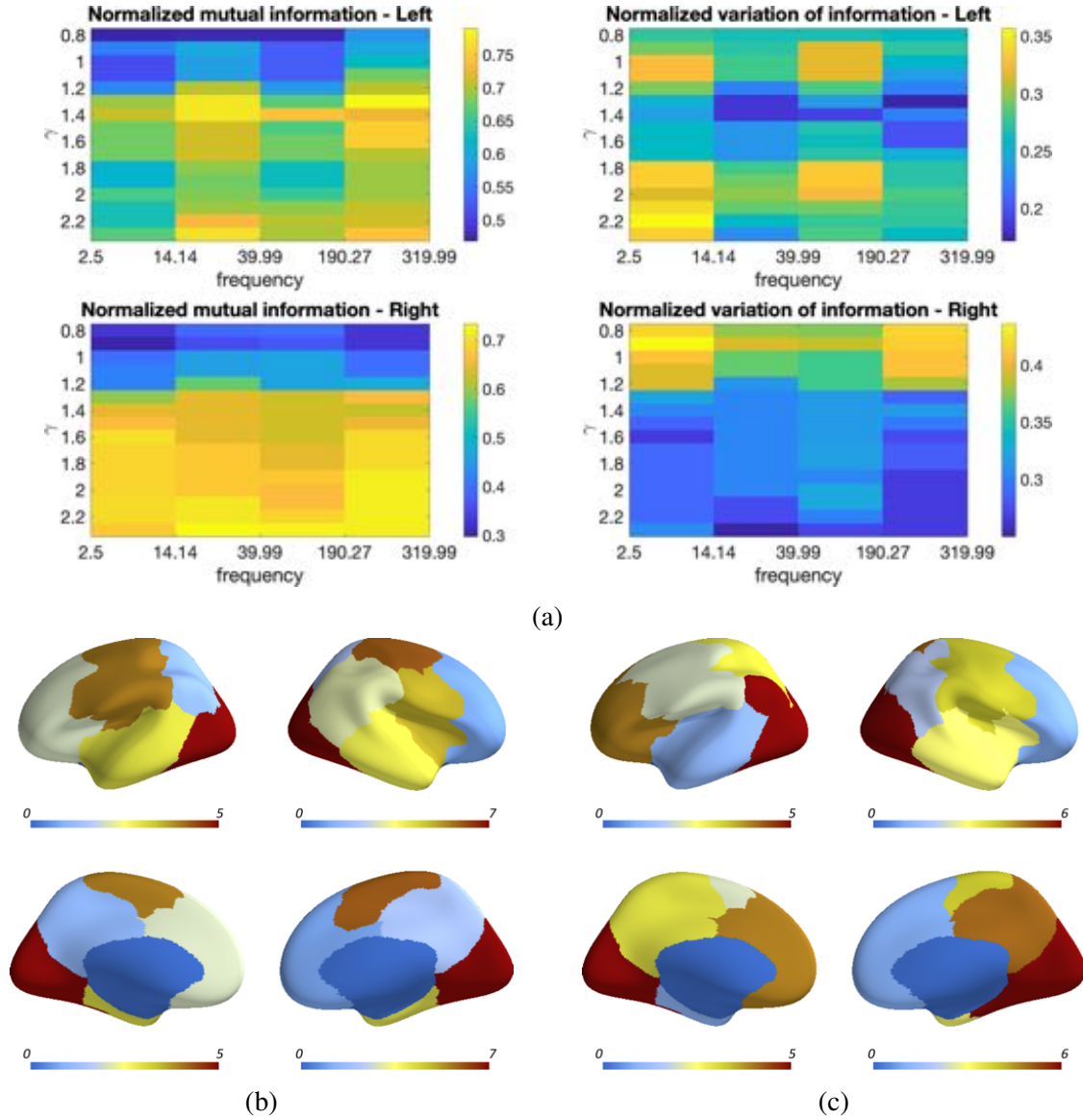
Figure 4.8 (a) Normalized mutual information (nMI, left column) and normalized variation of information (nVI, right column) for the comparison of SC and FC module partitions. The comparison was executed separately for left (top row) and right hemisphere (bottom row). (b) and (c) Left and right SC (b) and FC (c) partitions which produced the maximum *nMI* value (0.79 for the left, 0.73 for the right) and the minimum *nVI* value (0.17 for the left, 0.25 for the right). The left SC and FC partitions were composed of 5 modules; the right SC partition was composed of 7 modules, while the right FC partition had 6 modules.

Part II

Network-level structural and functional connectivity in the healthy and pathological child

Chapter 5

Feasibility of advanced WM structural reconstruction on paediatric data at low magnetic field and low *b*-value

5.1 Introduction

As introduced in Chapter 2, while functional connectivity can be computed from EEG or SEEG recordings also in paediatric patients with the same modalities as adult patients [Cossu et al. (2008); Taussig et al. (2014); Vanhatalo and Kaila (2006)], the computation of paediatric structural connectivity through advanced diffusion analysis methods is not as straightforward. This is true especially in the clinical environment, which often cannot not provide the necessary equipment and processing power for this type of analysis, and where classical DTI is almost always the preferred method of WM analysis in children, despite its known shortcomings [Farquharson et al. (2013)].

CSD-PT has been shown to reconstruct WM fibre tracts with higher precision and completeness than DTI [Küpper et al. (2015); Beare et al. (2016); Stefanou et al. (2016)], and has been increasingly used to study WM alterations and functional impairments in children. For example, Murray et al. (2016) used this method to analyse the correlation between WM abnormalities and changes in attention ability in children born very preterm, while Thompson et al. (2016) studied structural connectivity in very preterm children at 7 years of age and found it correlates with impaired intelligence and movement. Both Thompson et al. (2014) and Kelly et al. (2014) used CSD to study DTI scalar values and tract volume in the optic radiation of children born very preterm and to correlate them with visual outcome. Some

studies have started to apply CSD-PT to paediatric subjects for connectivity studies: for example, Mormina et al. (2016) used CSD-PT to evaluate the structural organization in a 17-year-old patient with cerebellar agenesis, while Backes et al. (2014) investigated the correlation between functional and structural connectivity in children with rolandic epilepsy compared with healthy controls, and Scheck et al. (2015) studied the connectivity of the anterior cingulate tract in children with unilateral cerebral palsy.

All these studies applied MRI acquisition parameters in line with the recommendations for CSD-PT described in Tournier et al. (2013). During my PhD I collaborated with the Giannina Gaslini hospital in Genova, with the aim of applying CSD-PT for the investigation of structural connectivity in neonatal and paediatric data. We chose to apply the method to data commonly available in a paediatric hospital: since the equipment present in the clinical environment often cannot fulfil the requirements for these methodologies, we chose to acquire data with hardware and acquisition sequences which are commonly found in these environments. The MRI scanner we used for the data acquisition was a 1.5T machine, a low field compared with the optimal 3T required for advanced analyses, and the acquisition sequence we selected had only 34 gradient directions and a b-value of 1000 s/mm^2, producing data which was suboptimal for the application of these methods. To our knowledge, no other study had been performed at the time with CSD-PT on unmyelinated subjects scanned at 1.5T with a low b-value and a small number of gradient directions.

Our aim was first to test the feasibility of CSD-PT on the data available in a typical paediatric clinical environment, and to adapt the preprocessing and processing steps and all the parameters used for the analysis, in order to obtain the best possible WM reconstructions of specific WM tracts with these methodologies, and compare their quality and anatomical accuracy with DTI reconstructions. If the diffusion analysis thus adapted could be applied also on this type of suboptimal data with good results, it could substitute DTI for WM analysis both in diagnostic processes and for the investigation of structural connectivity in patients, opening the way for more advanced studies with clinical data.

5.2 Materials and methods

5.2.1 Subjects and image acquisition

We analysed the DWI studies of 50 subjects (29 males) subdivided into three groups: 8 neonates (group I, mean age 11.63 $\pm$ 5.3 days), 20 infants (group II, from 1 month to 2 years old, mean age 5 $\pm$ 4.32 months), and 22 children and adolescents from 2 to 17 years

old (group III, mean age 8.18 $\pm$ 4.82 years). All subjects were originally admitted at the hospital for minor symptoms (e.g. headaches, minor head trauma) and were diagnosed as neurologically and developmentally normal by experienced paediatric neurologists, having normal MRI findings.

For each subject, a DWI sequence was acquired on a 1.5T scanner (Philips Intera Achieva version 2.6, Best, the Netherlands). The acquisition sequence was an axial single-shot spin-echo echo-planar sequence commonly used in clinical practice. Acquisition parameters were as follows: 60 axial slices; slice thickness, 2 mm; acquisition matrix, 128 $\times$ 128 (in-plane resolution, 1.75 $\times$ 1.75 mm); TR = 8129 ms; TE = 80 ms; averages = 1. The signal was acquired along 34 non-collinear directions of space, using a b-value of 1000 s/mm^2. One measurement without diffusion weighting ($b = 0$ s/mm^2) was also performed. The average duration of the acquisition sequence was 5 min 34 s. Neonates belonging to group I were fed before MRI examination to achieve spontaneous sleep and were spontaneously breathing during examination. For groups II and III, subjects under 6 years of age or who were uncooperative were sedated during examinations. For all subjects, heart rate and oxygen saturation were monitored by pulse-oximetry throughout the examination. For both sedated and non-sedated subjects, the duration of the examination was the same, in order to keep the sedation period as short as possible. All brain MRI studies were obtained with axial sections parallel to the bicommissural line, and included additional 3-mm-thick T2-weighted images on the three planes of space and a 3D T1 anatomical sequence, with different acquisition parameters based on patient age. These sequences were used to assess the presence of brain lesions or malformations.

5.2.2   Whole-brain tractography and track-density maps

All DWI images were preprocessed with FSL tools [Jenkinson et al. (2012)], correcting for subject movement artefacts and eddy currents. Fibre tracking was performed using the MRtrix package (https://github.com/MRtrix3/mrtrix3) [Tournier et al. (2012)]. CSD was performed on the preprocessed DWI images in order to estimate the FODs in each voxel, using a maximum harmonic degree (λ_{max}) of 6, which was the maximum value allowed by the data, as described in Tournier et al. (2009). From these FODs, streamlines were computed using the `iFOD2` algorithm, developed by Tournier et al. (2009) and made available by the MRtrix toolbox.

As a first step, we computed a whole-brain tractogram for each subject. Each tractogram was composed by 2 million streamlines, with a maximum number of generation trials for the algorithm of 200 million.

The tractography algorithm requires the setting of several parameters, which influence the quality of the resulting tractograms: the default values for these parameters are usually chosen as the ones producing the best results for healthy adult data, which is the 'default' data most often used to test processing algorithms. Because of this, we tested different combinations of tracking parameters in order to see their effect on the reconstructions obtainable from paediatric data, following the work of Tournier et al. (2012) and Tournier et al. (2010). Step size was set to the default value of 0.9 mm (about 0.5 times the voxel size, as recommended for the `iFOD2` algorithm in Tournier et al. (2009)), which was shown to be a good compromise between quality of the results and computational time. As performed in the study by Tournier et al. (2012), we tested different values for the cut-off threshold (FOD amplitude value under which the streamlines are terminated) and for the maximum angle between successive tracking steps. In order to find the best combination of values for these parameters, we produced whole-brain tractograms for six representative subjects selected at random from the three groups (two neonates from group I, two infants from group II, and two children from group III), using different combinations of parameters. One expert neuroradiologist examined the results for each combination of values and rated them on a 5-point scale (1, non-diagnostic tracks; 2, poor quality; 3, fair quality; 4, good quality; 5, excellent quality). The combination of parameters which obtained on average the highest scores in this preliminary test was selected as the 'default' for the subsequent analyses. The cut-off threshold was set to be 0.2, while the maximum angle between steps was $50°$. Table 5.1 shows the results of the rating for the different combinations of values.

The maximum and minimum streamline lengths were set, respectively, to 200 mm (about ten times the size of the DWI voxel) and 9 mm (about 5 times the voxel size), as suggested in the toolbox documentation. The generated streamlines were anatomically restrained with a binary brain mask computed directly from the DWI images with the MRtrix toolbox: streamlines were terminated when they exited the mask. The same brain mask was also used as a seeding mask: generation points for the computed streamlines ("seeds") were uniformly distributed in the mask, and streamlines were propagated from each seed bidirectionally until termination. The average computation time for this first step (including preprocessing, up to the generation of the whole-brain tractograms) was of 30 min on an iMac desktop workstation (8-core Intel Core i7 @3.5 GHz, 32 GB RAM).

Max angle	FOD amplitude	Score frequency				
		1	2	3	4	5
10°	0.1	100%	-	-	-	-
	0.2	100%	-	-	-	-
	0.3	100%	-	-	-	-
	0.4	100%	-	-	-	-
30°	0.1	33.3%	66.7%	-	-	-
	0.2	-	-	100%	-	-
	0.3	16.7%	83.3%	-	-	-
	0.4	100%	-	-	-	-
50°	0.1	-	-	66.7%	33.3%	-
	0.2	-	-	-	66.7%	33.3%
	0.3	-	16.7%	83.3%	-	-
	0.4	100%	-	-	-	-
70°	0.1	-	-	100%	-	-
	0.2	-	-	-	100%	-
	0.3	-	66.7%	33.3%	-	-
	0.4	100%	-	-	-	-
90°	0.1	-	-	100%	-	-
	0.2	-	100%	-	-	-
	0.3	-	100%	-	-	-
	0.4	100%	-	-	-	-

Table 5.1 Average scores for whole-brain CSD-PT tractograms obtained with different values of FOD amplitude threshold (0.1, 0.2, 0.3 and 0.4) and maximum angle between tracking steps (10°, 30°, 50°, 70°, 90°). For visualization purposes, a dash ("-") marks cells where the score frequency was 0.0%.

From the whole-brain tractograms, we computed for each subject a gray-scale super resolution track-density imaging (TDI) map and a directionally encoded colour TDI map (DEC-TDI map) [Calamante et al. (2010), with a spatial resolution of 0.5 mm. DEC-TDI maps were coloured by assigning red to the right–left direction, green to the anterior–posterior direction, and blue to the inferior–superior direction. In order to improve visualization of the maps, we applied a short-track method to produce short-track DEC-TDI maps (stDEC-TDI maps) as previously reported by Hoch et al. (2016). Short-track TDI and DEC-TDI maps allow to better visualize low-intensity fibre tracts and assess the quality of the tractography results. The short maximum length of the reconstructed tracks lowers the TDI contrast in these maps, allowing to better visualize low-intensity structures without over-saturating high-intensity tracts. In order to maintain the contrast-to-noise ratio, the number of streamlines generated for these maps needs to be about one order of magnitude greater than the number

used for normal TDI maps [Calamante et al. (2012)]: we computed the maps from tractograms composed of 20 million streamlines. The rest of the parameters were the same used for the whole-brain tractograms mentioned earlier (FOD amplitude threshold, 0.2; maximum angle between steps, $50°$; step size, 0.9 mm), but the maximum streamline length was set to 20 mm in order to fully exploit the advantages offered by this technique.

5.2.3 Eigenvector maps and anatomical analysis of conventional and stTDI data

To provide comparison with the computed TDI and stDEC-TDI maps, we used the MRtrix3 toolbox to compute the DTI diffusion tensors in each subject. From these diffusion tensors, we computed a colour-coded map of the principal eigenvector (EV map) for each subject, in order to compare it with the stDEC-TDI map. EV maps encode, in each voxel, the main direction of diffusion within the voxel, together with its magnitude. The maps were colour-coded with respect to this main diffusion direction in the same way as the DEC-TDI and stDEC-TDI maps (red for left–right, green for anterior–posterior, blue for inferior–superior) and had the same voxel size as the DWI data.

A team of neuroradiologists with experience on paediatric neuroimaging studies reviewed all MRI studies to perform an image quality assessment. For each subject, they characterized anatomical detail in axial MRI sections from the conventional MRI protocol, EV maps, and short-track TDI parameter maps at 5 canonical anatomical levels of the brain: corpus callosum, internal capsule, rostral midbrain, middle pons, and rostral medulla (similar to the work by Hoch et al. (2016)). The TDI maps were then labelled by consensus according to the standard anatomical texts of Duvernoy's Atlas of the Human Brain Stem and Cerebellum [Naidich et al. (2009)] and of WM atlas mapping [Catani and de Schotten (2008)].

5.2.4 ROI placement and reconstruction of WM tracts

In order to evaluate the performance of CSD, we used a probabilistic tractography method to reconstruct three main WM tracts: the cerebellar-thalamic tracts (CTT), the corticopontocerebellar tracts (CPCT), and the corticospinal tracts (CST). Because of their important roles in voluntary movement control, these tracts are among the main constituents of the WM pathways most commonly investigated by tractography. In particular, the CTT is the main efferent tract from the cerebellum, the CPCT constitutes the main afferent pathway from the cerebral cortex to the cerebellum, and the CST originates from the precentral areas and

descends through the centrum semiovale and ipsilateral posterior limb of internal capsule to the brainstem.

The tracts were reconstructed using either a single or a multiple regions of interest (ROI) approach depending on the specific tract, according to WM atlas mapping [Catani and de Schotten (2008)]. In each subject, ROIs were drawn separately for the right and left sides on computed DEC-TDI maps, taking advantage of the improved anatomical visualization offered by these maps.

In detail, (i) for the CPCT, we placed a seeding ROI in the middle cerebellar peduncle on the coronal plane and an inclusion ROI in the posterior limb of the internal capsule on the axial plane; (ii) for the CTT, we placed a seeding ROI in the superior cerebellar peduncle on the coronal plane; and (iii) for the CST, we placed the seeding ROI on the posterior limb of the internal capsule, and an additional ROI was placed in the cerebral peduncle, on the right and left sides separately, on the axial plane. The ROIs were drawn by a single operator during a single session, in order to reduce inter-subject variability. All the ROIs were drawn so as to completely include the anatomical structures mentioned earlier, as previously described by Lim et al. (2015), thus ensuring that the considered tract would be included in the final reconstruction while diminishing the influence of the ROI choice on the final tract reconstructions [Huang et al. (2004)].

Tractography was performed for each tract with the same algorithm and parameters used to compute the whole-brain tractograms. Each tract was composed of 10000 streamlines, with a maximum number of generation trials for the algorithm of 1 million. All selected tracts were also reconstructed with a combination of traditional DTI and deterministic tractography (Fibre Assignment by Continuous Tracking (FACT), Mori et al. (1999)), in order to validate the CSD reconstruction results and to compare the quality of the tracts obtained with the two methods, using the same ROI placement. The DTI analysis and deterministic tractography were performed using the MRtrix package, which implements the deterministic tractography method on the diffusion-weighted images. Parameters were left at their default values for the toolbox, as defined in the study by Tournier et al. (2012). These parameters were found to give the best results for the data, as determined by visual inspection of the results. In particular, the FA threshold (value under which streamlines were terminated) was 0.1 and the maximum angle between steps was $9°$. As for CSD tractography, the maximum streamline length was set to 200 mm. Again, each tract was composed of 10000 streamlines, with a maximum trial number of 1 million. For both methods and all tracts, reconstructions were obtained by seeding streamlines uniformly inside the selected ROIs and propagating them

bidirectionally until termination. The same brain mask used for the whole-brain tractograms was used to terminate streamlines when they exited the brain.

5.2.5   Qualitative analysis of reconstructed tracts

A team of neuroradiologists independently reviewed all tractography results using Trackvis (http://trackvis.org/), a software program that allows interactive visualization of tractography reconstructions. The neuroradiologists performed a track quality assessment by using a 5-point scale (1, non-diagnostic tracks; 2, poor quality; 3, fair quality; 4, good quality; 5, excellent quality). The evaluations were based on the presence of false-positive and false-negative tracts and anatomical accuracy of the reconstructed bundles [Beddy et al. (2011)].

5.2.6   Statistical analysis

For each tract and reconstructing technique, frequencies and percentages of the quality score were calculated across subjects. The average weighted score was computed for each tract and for each evaluator as the average of all scores weighted by their frequency. Chi-square test was used to compare qualitative scores of CSD and DTI tracts. Inter-observer agreement was evaluated using the Cohen's kappa test [Cohen (1960)]: a value of $K > 0.70$ indicated excellent, 0.40 to 0.70 fair-to-good (moderate), and < 0.40 poor agreement [Fleiss et al. (2003)]. Statistical analysis was performed with SPSS Statistics for Mac 21.0 (IBM, Armonk, NY, USA). Results were considered significant at $p < 0.05$.

5.3   Results

5.3.1   EV Maps, Short-Track TDI, and DEC-TDI Maps

Good quality directionally encoded colour track density maps were obtained in all patients, as determined by visual inspection. Short-track TDI and DEC-TDI maps better depicted the brain anatomy compared with the conventional images, showing consistent concordance with available anatomical atlases and previous studies [Hoch et al. (2016); Naidich et al. (2009); Catani and de Schotten (2008)]. The EV maps allowed to visualize the main fibre tracts in older children, while they presented a more blurred appearance for unmyelinated neonates; the distinguishable level of detail was lower in the EV maps than in stDEC-TDI for all subjects.

Figures 5.1-5.3 demonstrate axial images of the brain at 5 discrete anatomical levels on conventional imaging, EV maps, and stDEC-TDI maps in one representative case of each age group, respectively.

Figure 5.1 EV maps and stDEC-TDI maps at 5 canonical brain levels (rostral medulla, middle pons, rostral midbrain, internal capsules, corpus callosum) in a 6-day neonate. Axial T2-weighted images (upper row) and corresponding EV maps (middle row) and stDEC-TDI images (bottom row). Conventional color scheme: blue (inferior-superior), green (antero-posterior), and red (left-right). Note that even in an unmyelinated brain the corticospinal tract is clearly visible from the bulbar level to the centrum semiovale in the stDEC-TDI map (arrowheads), while it is more difficult to distinguish in the EV maps especially at the bulbar level (first column).

In particular, even in unmyelinated or partially myelinated brains, several WM bundles could be clearly discriminated in the stDEC-TDI maps (Figures 5.1 and 5.2), while the same bundles were harder to distinguish in the EV maps, especially at the brainstem levels. In older children, WM tracts and nuclear groups could be visualized with greater anatomical detail in the stDEC-TDI maps than in the EV maps, again particularly in the brainstem (Figure 5.3). By comparing zoomed versions of the EV and stDEC-TDI maps, the advantage in visualization offered by the stDEC-TDI maps is clear: the reduced voxel size allows to easily visualize and distinguish the WM tracts even when zooming the image, while the EV
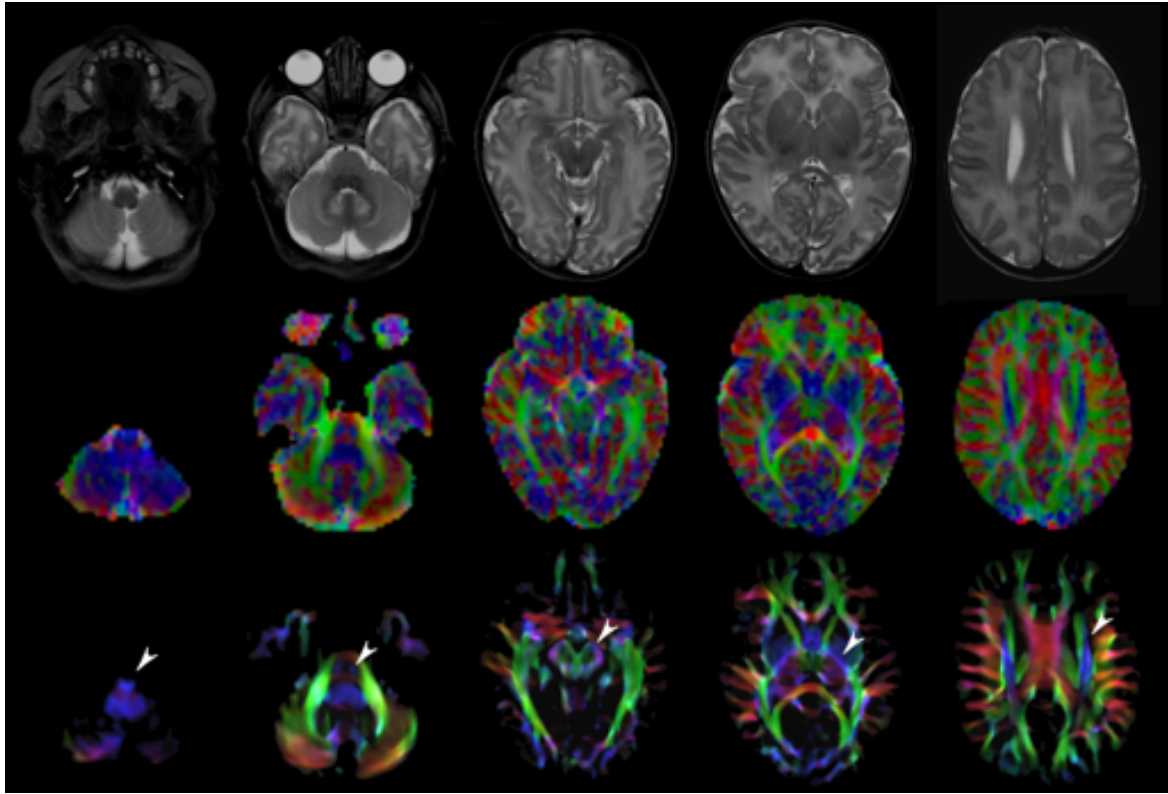
Figure 5.2 EV maps and stDEC-TDI maps at 5 canonical brain levels (rostral medulla, middle pons, rostral midbrain, internal capsules, corpus callosum) in a 16-month-old infant. Axial T2-weighted images (upper row) and corresponding EV maps (middle row) and stDEC-TDI images (bottom row). Conventional color scheme: blue (inferior-superior), green (antero-posterior), and red (left-right). The stDEC-TDI images clearly show the genu (thin arrow) and splenium (empty arrow) of the corpus callosum in red. The anterior columns of the fornix (arrowhead) are depicted in light blue. The anterior portion of cingulum (thick arrow) is coloured in green. The main WM tracts are distinguishable also in the EV maps, but the quality is lower; the corticospinal tract is almost not distinguishable from non-WM voxels at the bulbar level (first column), while in the stDEC-TDI map it is clearly visible and distinguished from the background.

maps appear blurred and with a stair-step effect. The different anatomical structure is more confused and less easily discriminated in the zoomed EV maps (Figure 5.4).

5.3.2   CSD and DTI reconstruction of white matter tracts

All tracts were reconstructed with CSD-PT, showing a 100% success rate for CSD-PT fibre tractography reconstruction. DTI fibre reconstruction also showed a 100% success rate, but the reconstructions obtained with CSD-PT received higher quality scores more frequently
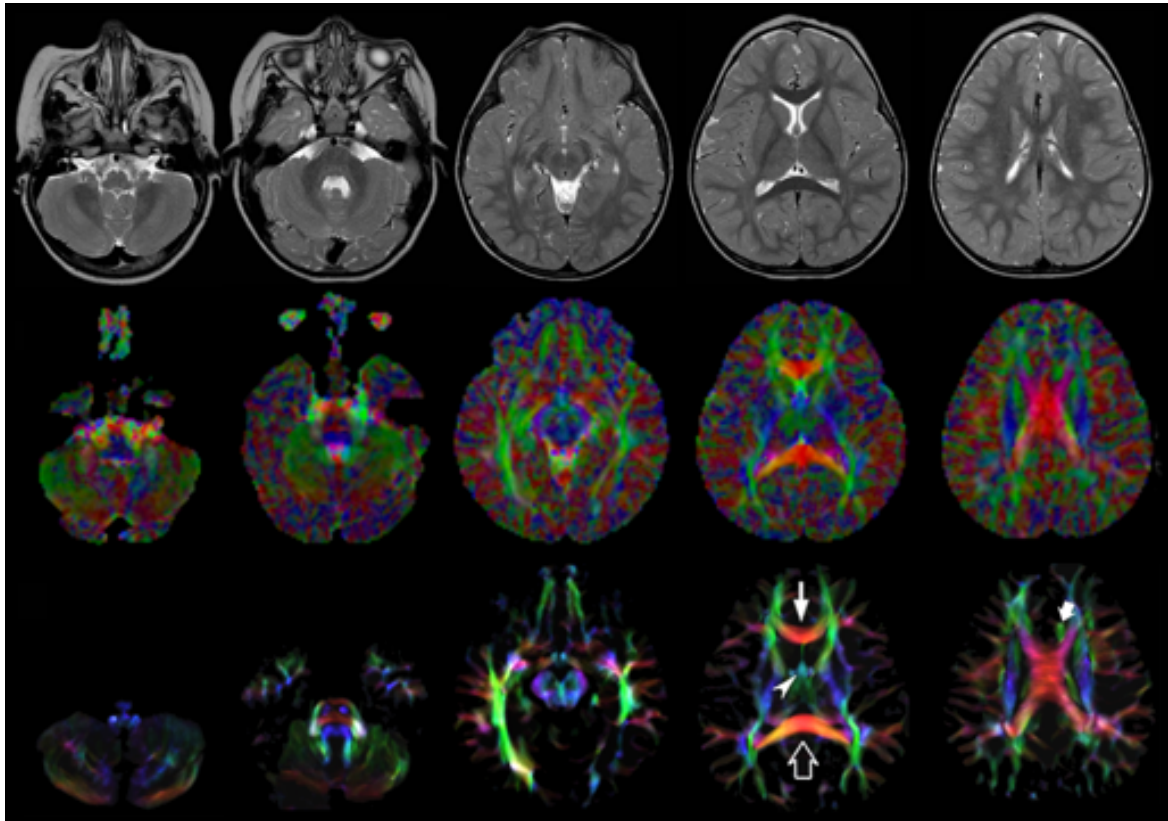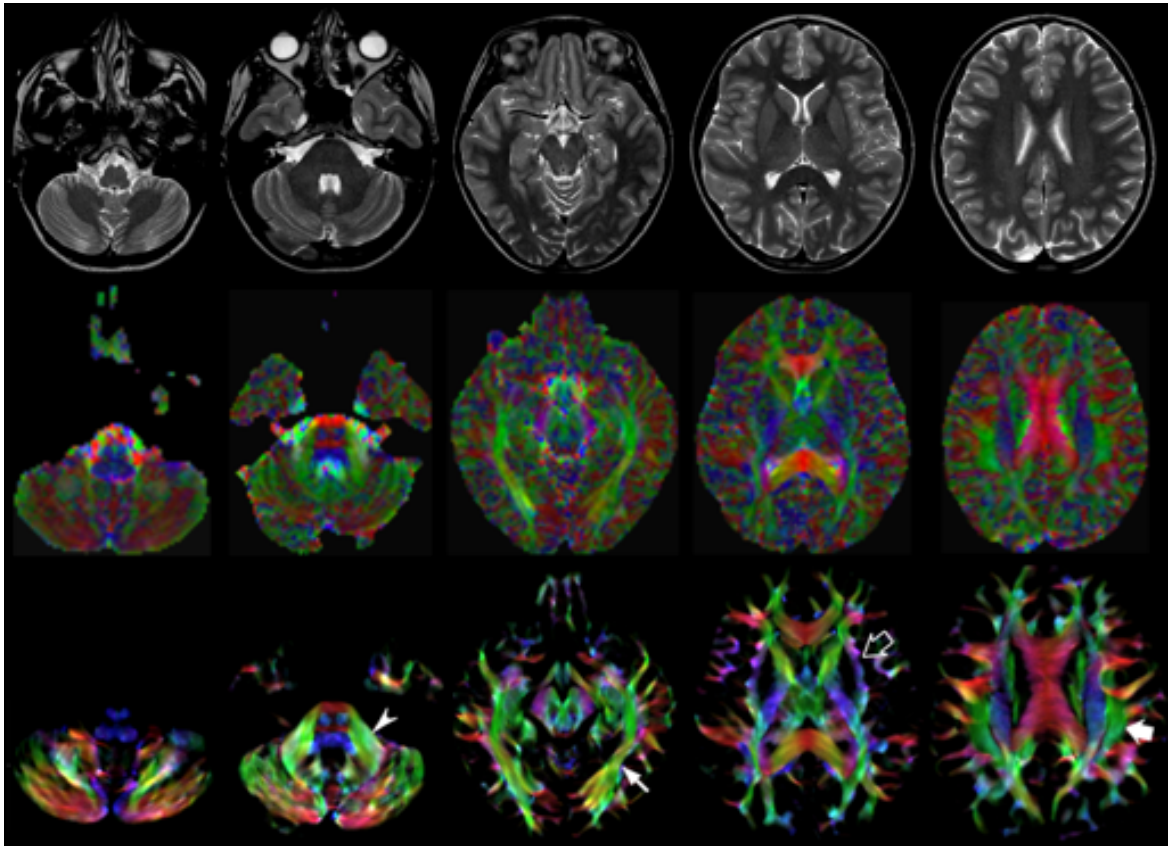
Figure 5.3 EV maps and stDEC-TDI maps at 5 canonical brain levels (rostral medulla, middle pons, rostral midbrain, internal capsules, corpus callosum) in a 10-year-old child. Axial T2-weighted images (upper row) and corresponding EV maps (middle row) and stDEC-TDI images (bottom row). Conventional color scheme: blue (inferior-superior), green (antero-posterior), and red (left-right). The stDEC-TDI maps show the middle cerebellar peduncles in green (arrowhead), the inferior longitudinal fasciculi in green (thin arrow), the external capsules in blue-green (empty arrow), and the superior longitudinal fasciculi in green (thick arrow). As in the infant case, the visualization is enhanced in the stDEC-TDI maps and the quality is higher; non-WM voxels show no values, while in the EV maps the WM structures are harder to distinguish from the background voxels.

than the DTI reconstruction. A summary of visual assessment results and inter-reader agreement evaluation are reported in Table 5.2.

Figures 5.5-5.7 demonstrate CTT, CPCT, and CST reconstructions using both methods in one representative case of each age group, respectively.

While all the considered fibre tracts are reconstructed successfully, the DTI tracts appeared thinner and with a reduced volume with respect to known anatomy, especially in the infant (Figure 5.6) and neonate (Figure 5.5). CSD-PT tracts, on the contrary, were fully reconstructed even in unmyelinated neonates, showing the full volume of the WM structures.
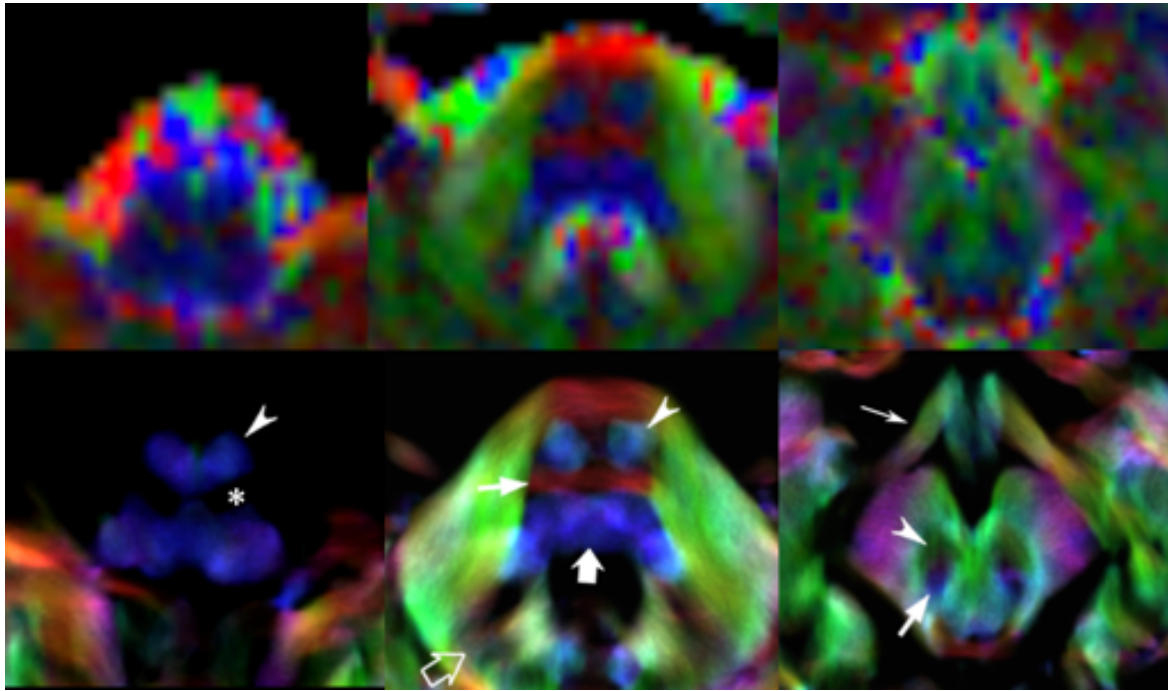
Figure 5.4 EV maps and stDEC-TDI maps, magnified view at 3 brainstem levels (rostral medulla, middle pons, rostral midbrain) in an 8-year-old child. Upper row: EV images. Lower row: stDEC-TDI images. Conventional color scheme: blue (inferior-superior), green (anteroposterior), and red (left-right). First column: at the bulbar level, the corticospinal tract is on the anterior surface of the pyramids (arrowhead), adjacent to the inferior olivary nucleus (asterisk). In the EV map, non-WM voxels show and 'blur' the corticospinal tract, making it more difficult to distinguish. Second column: at mid-pons level, the pyramidal tract (arrowhead) is clearly separated from the transverse pontocerebellar fibres (thin arrow) and ascending pathways (thick arrow). Note the dentate nuclei (empty arrow), almost not recognizable in the EV map. Third column: at rostral midbrain, the central tegmental tract (arrow) is located posteriorly to the red nuclei (arrowhead). Note the optic tracts coloured in green (thin arrow). The smaller voxel size of the stDEC-TDI maps allows to visualize all the structures correctly even at a zoomed level, while the EV maps at the same level of magnification appear blurred and with a stair-stepped effect.

The resulting average scores with the relative standard deviations are reported in Table 5.3. Average scores for CSD-PT tracts were always higher than DTI scores, with a difference ranging from 0.7 to 1.4 points. The difference between scores for the two methods was always significant ($p < 0.05$ for all tracts and all readers) (Table 5.2).

Figure 5.8 shows the frequency of the scores assigned to all tracts for the different reconstruction methods and for both evaluators. No reconstruction was scored with 1 or 2 points, confirming the 100% success rate for both reconstruction methods; however, lower scores were more frequently awarded to DTI reconstructions, while the frequency of higher scores was higher for CSD-PT reconstructions.

Tract	Method	Reader 1			Reader 2			Cohen's K	p-value
		Score	Frequency	p-value χ^2	Score	Frequency	p-value χ^2	Cohen's K	p-value
CTT	DTI	3	18 (36%)		3	15 (30%)		0.60	**< 0.001**$*$
		4	32 (64%)		4	35 (70%)			
		5	0 (0%)	**< 0.001**$*$	5	0 (0%)	**< 0.001**$*$		
	CSD-PT	3	3 (6%)		3	2 (4%)		0.66	**< 0.001**$*$
		4	28 (56%)		4	27 (54%)			
		5	19 (38%)		5	21 (42%)			
CPCT	DTI	3	25 (50%)		3	22 (44%)		0.72	**< 0.001**$*$
		4	25 (50%)		4	28 (56%)			
		5	0 (0%)	**0.008**$*$	5	0 (0%)	**0.025**$*$		
	CSD-PT	3	2 (4%)		3	5 (10%)		0.62	**< 0.001**$*$
		4	35 (70%)		4	32 (64%)			
		5	13 (26%)		5	13 (26%)			
CST	DTI	3	43 (86%)		3	38 (76%)		0.66	**< 0.001**$*$
		4	7 (14%)		4	12 (24%)			
		5	0 (0%)	**0.039**$*$	5	0 (0%)	**0.024**$*$		
	CSD-PT	3	1 (2%)		3	0 (0%)		0.57	**< 0.001**$*$
		4	20 (40%)		4	25 (50%)			
		5	29 (58%)		5	25 (50%)			

Table 5.2 Quality scores with relative frequencies and inter-reader agreements for the DTI and CSD-PT reconstructions of CTT, CPCT and CST tracts. Legend: CTT, cerebellar thalamic tract; CPCT, corticopontocerebellar tract; CST, corticospinal tract; CSD, constrained spherical deconvolution; DTI, diffusion tensor imaging; p-value χ^2, p-value for the Chi square test. The 5-point scale: 1, non-diagnostic; 2, poor quality; 3, fair quality; 4, good quality; 5, excellent quality. Only scores from 3 to 5 are reported because no reconstruction was scored with 1 or 2 points.

No reconstruction obtained with DTI received the highest score of 5 points, while CSD-PT reconstruction was scored 5 points on average in 40% of the comparisons for CTT, 26% of the comparisons for CPCT, and 54% of the comparisons for CST. For CSD-PT reconstructions of CST, the highest score of 5 points was the most frequently awarded for both readers, while the most frequent score for DTI reconstructions of the same tract was of 3 points. A moderate-to-excellent inter-reader agreement was observed for all qualitative evaluations, with values ranging between 0.6 and 0.7.
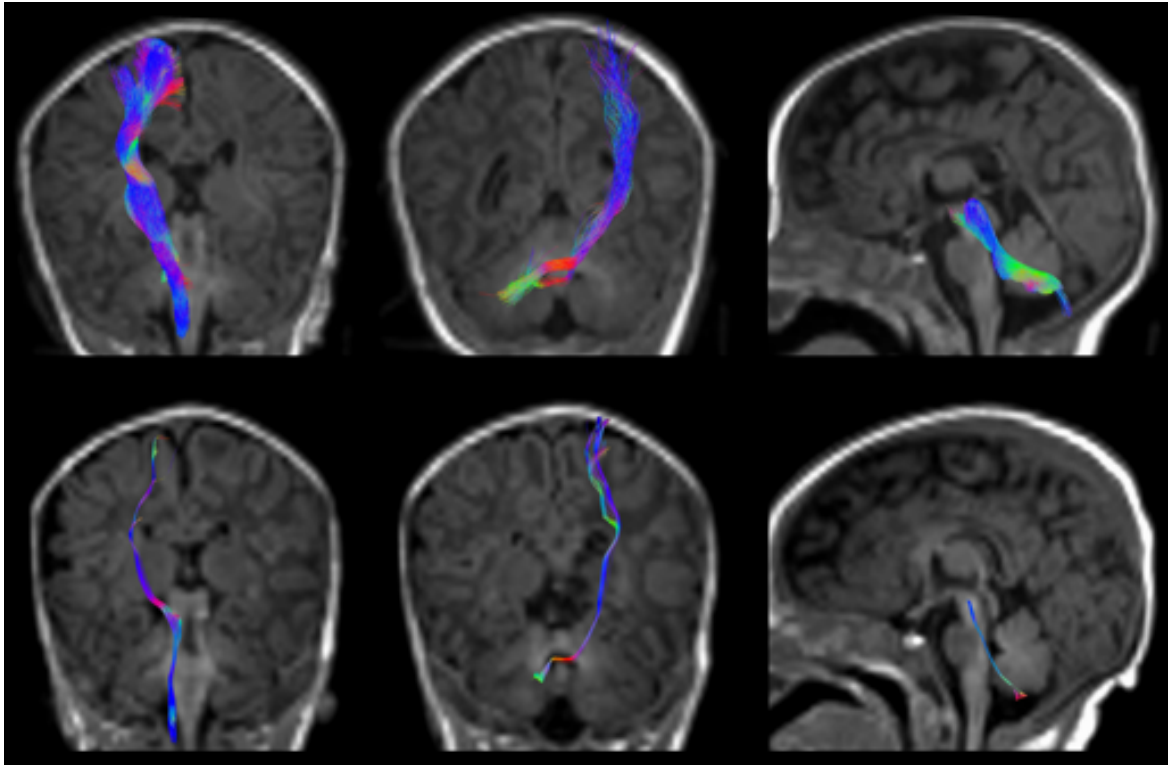
Figure 5.5 CSD-PT (upper row) and DTI (lower row) reconstructions of the CST (first column), CPCT (second column), and CTT (third column) in a 10-day-old neonate. All tracts are reconstructed with both techniques but the quality of CSD-PT tracts is superior to that of DTI.

Tract	Method	Reader 1	Reader 2
CTT	DTI	3.64 ± 0.48	3.70 ± 0.46
	CSD-PT	4.32 ± 0.59	4.38 ± 0.57
CPCT	DTI	3.50 ± 0.51	3.56 ± 0.50
	CSD-PT	4.22 ± 0.51	4.16 ± 0.58
CST	DTI	3.14 ± 0.35	3.24 ± 0.43
	CSD-PT	4.56 ± 0.54	4.50 ± 0.51

Table 5.3 Average scores and standard deviations for the DTI and CSD-PT reconstructions of CTT, CPCT and CST tracts.
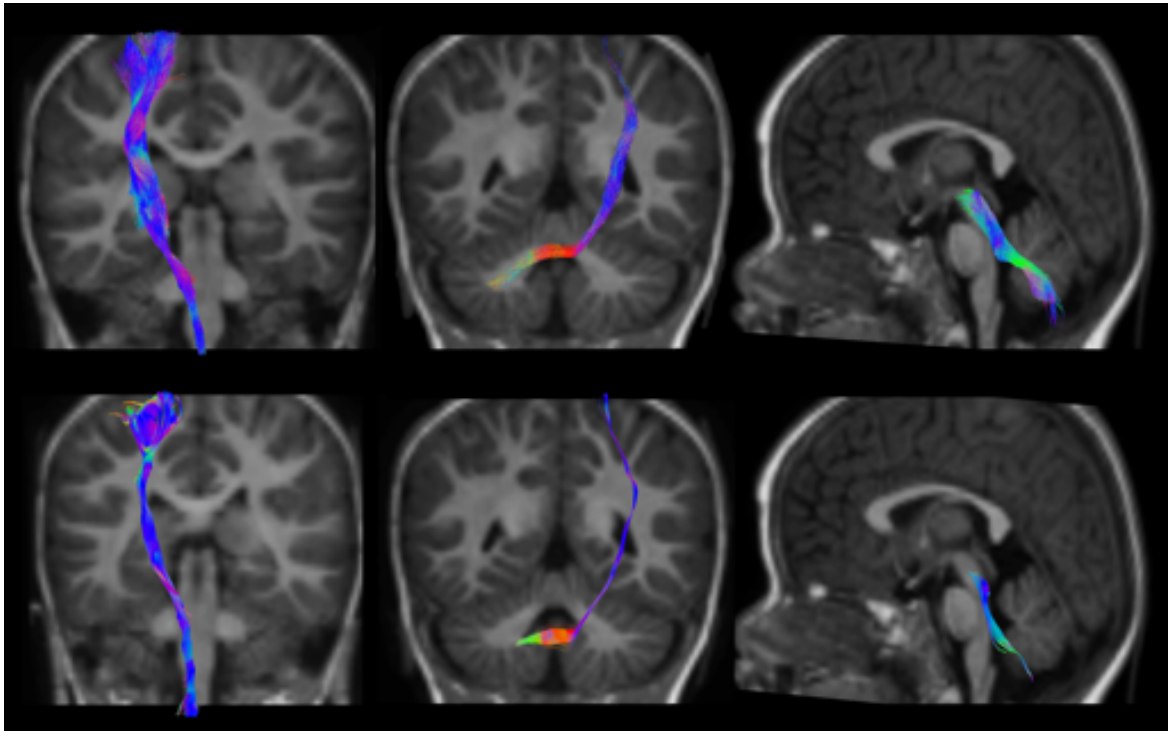
Figure 5.6 CSD-PT (upper row) and DTI (lower row) reconstructions of the CST (first column), CPCT (second column), and CTT (third column) in a 12-month-old infant. All tracts are reconstructed with both techniques but the quality of CSD-PT tracts is superior to that of DTI.
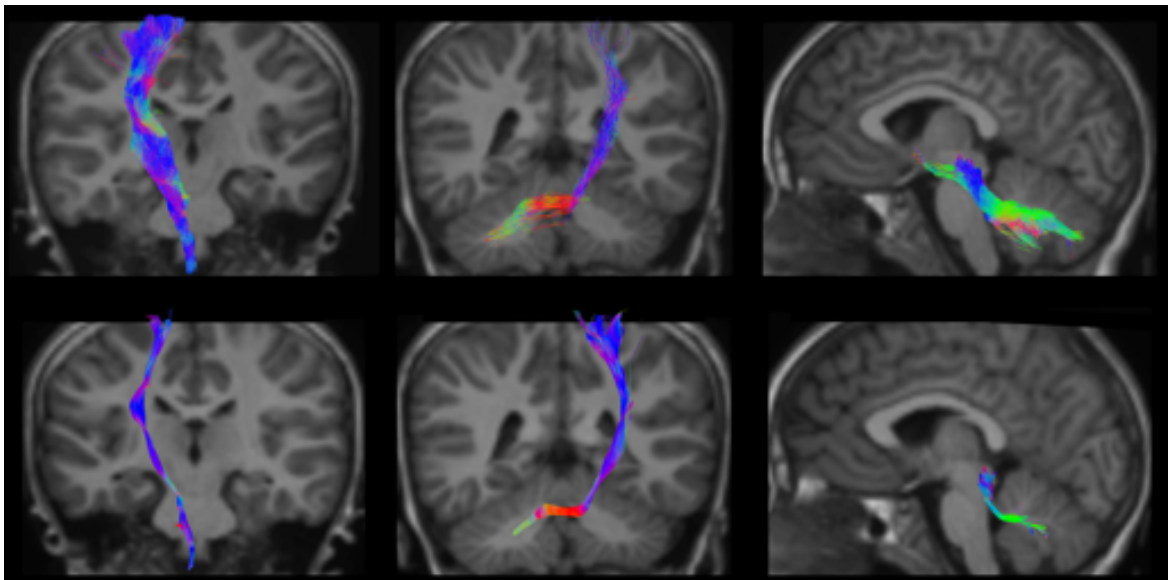
Figure 5.7 CSD-PT (upper row) and DTI (lower row) reconstructions of the CST (first column), CPCT (second column), and CTT (third column) in a 6-year-old child. All tracts are reconstructed with both techniques but the quality of CSD-PT tracts is superior to that of DTI.
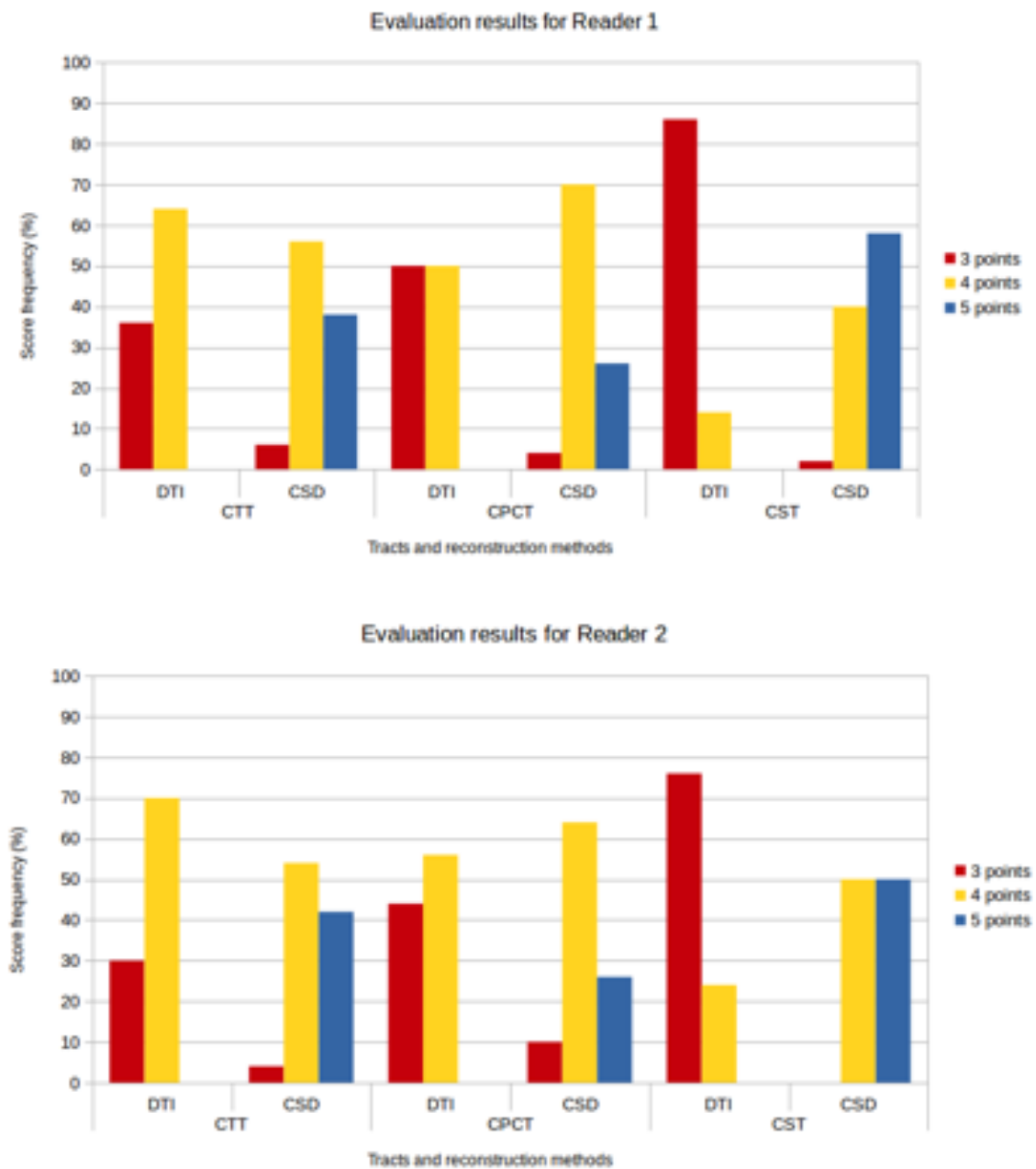
Figure 5.8 Score frequency histograms for all tracts and reconstruction methods. Top plot: results for Reader 1, bottom plot: results for Reader 2. Only scores from 3 to 5 points are reported in the plots, because no reconstruction was rated 1 or 2 points.

Chapter 6

Modifications of network-level structural connectivity in children with segmental callosal agenesis

6.1 Introduction

In Chapter 5 we showed that CSD-PT can be successfully applied to paediatric clinical data from healthy subjects to obtain WM fibre tracts reconstructions, with better results than with classical DTI. The subsequent step in my work was then to apply this reconstruction methodology to a group of pathological subjects. The objectives of this part of the work were: i) to further confirm the applicability of CSD-PT on this kind of data, even in pathological cases, where normal anatomy is disrupted; ii) to exploit the capabilities of CSD-PT to investigate how WM modifications brought on by a specific malformation can influence structural connectivity with respect to normal, healthy connectivity.

In collaboration with the Gaslini hospital, we chose to study structural connectivity modifications in a specific congenital defect: segmental agenesis of the corpus callosum (segACC). This is a peculiar form of partial callosal agenesis (ACC) characterized by the absence of the central portion of the corpus callosum — a thick tract of commissural fibres which connects the brain's hemispheres — with disconnection between the anterior (genus) and posterior (splenium) corpus callosum [Raybaud and Girard (1998), Raybaud (2010)]. On conventional imaging, the anterior and posterior segments appear, respectively, as genual and splenial remnants, while the intermediate segment is a thin lamina, usually corresponding to the hippocampal commissure [Raybaud (2010)] These features were traditionally considered

the result of an early destructive insult during central nervous system development. Indeed, for many years, the prevailing theory held that the corpus callosum developed in an anterior-to-posterior direction, starting with the genu, followed by the body, splenium, and finally the rostrum [Barkovich and Kjos (1988)]. According to this model, segACC can only be explained by an acquired disruptive event occurring after corpus callosum development has been completed. On the other hand, segACC has been described in siblings and in patients with no evidence of cerebral lesions, suggesting a malformative rather than acquired origin [Raybaud and Girard (1998)]. New theories on the bicentric origin of the corpus callosum have further supported the malformative hypothesis [Raybaud (2010)]. Nevertheless, little is still known about the structural connectivity pattern and clinical-genetic phenotypes associated with this callosal malformation.

The first investigations of callosal malformation were done with anatomical MR scans [Barkovich and Kjos (1988)] and DTI with FACT tractography [Lee et al. (2004)], showing the connectivity pattern of Probst bundles and revealing the presence of aberrant heterotopic callosal tracts in partial ACC. More recently, advanced diffusion analysis allowed to characterize the wide variability of callosal connections in partial ACC [Wahl et al. (2009)]. The structural connectivity framework has greatly improved the characterization of WM abnormalities in patients with ACC, revealing different patterns of global and local connectivity and greater inter-individual variation of brain network organization compared with healthy subjects [Owen et al. (2013); Meoded et al. (2015); Jakab et al. (2015)].

In this study, we aimed to determine the impact of segACC on large-scale brain networks, comparing network topologic properties related to integration and segregation among children with this malformation relative to healthy controls, and we applied network-based statistics to quantify connectivity differences. In particular, we hypothesized that the absence of the central callosal portion would reduce the long-range global connectivity and increases the short-range local connectivity in patients with segACC. We also expected to find increased variability of node degree spatial distribution and correlation strengths in patients with segACC compared with controls. Finally, we postulated that the modular organization of the segACC brain is different compared with healthy controls.

6.2   Materials and Methods

6.2.1   Image acquisition and preprocessing

This was a single-centre retrospective case-control study, performed with Gaslini Institute review board approval and parental written informed consent. We reviewed the MR imaging studies, clinical information, and genetic data of 8 children consecutively diagnosed with segACC between 2010 and 2015 (5 males; mean age at MR imaging, 3.9 years; range, 22 days to 5.11 years). Connectome analysis was performed in the 5 patients with segACC older than 2 years of age, because no major reorganization of structural modules is usually observed after this age [Hagmann et al. (2010)]. We selected 10 age- and sex-matched controls who underwent brain MR imaging with DTI for transient febrile convulsion, minor trauma, or headaches; all had normal brain anatomy, psychomotor development, and neurologic examination.

MR imaging was performed on a 1.5T scanner with an 8-channel head coil and included a 3-mm-thick axial T2 volume, FLAIR, and DWI; a 3-mm-thick coronal T2 volume; sagittal 0.6-mm-thick 3D driven equilibrium; and a 3D turbo field echo T1 volume. DWI data was collected along 34 non-collinear directions by using an axial single-shot spin-echo echo-planar sequence, with b-values of 0 and 1000 s/mm^2, TR = 9203ms, TE = 71 ms, section thickness 2 mm, FOV = 240 $\times$ 240 mm, matrix size = 128 $\times$ 128. Uncooperative patients were sedated during the examinations.

The FMRIB Diffusion Toolbox 3.0 (http://fsl.fmrib.ox.ac.uk/fsl/fslwiki/FDT) was used to correct DWI raw data for motion artefacts and eddy current distortion and to calculate the tensor and DTI metrics maps. Subsequently, we used the FMRIB Linear Image Registration Tool (FLIRT; http://www.fmrib.ox.ac.uk/) to perform linear registration between the reference $b = 0$ images and the 3D-T1 volume. Non-brain tissue was removed by using the MRtrix3 package (https://github.com/MRtrix3/mrtrix3).

6.2.2   Probabilistic tractography and connectivity matrix computation

CSD-PT was performed on the preprocessed diffusion-weighted images by using the MRtrix3 package [Tournier et al. (2012)]. For each subject, a whole-brain tractography consisting of 3 million streamlines was generated, using the Anatomically Constrained Tractography framework (ACT) [Smith et al. (2012)]. The seeds used for generating streamlines were distributed uniformly in the gray/white matter interface. The tractograms were filtered by

using the Spherical Deconvolution Informed Filtering of Tractograms (SIFT) [Smith et al. (2013), and the final result consisted of 1.5 million streamlines for each subject.

Fibre segmentation was performed by using TrackVis 0.5.1 (www.trackvis.org) with a manually drawn multi-ROI approach, following the callosal fibre segmentation method described by Wahl et al. (2009) (Figure B.1 in Appendix B). Qualitative analysis was performed by a team of paediatric neuroradiologists who evaluated the anatomic course of reconstructed tracts on superimposed 3D-T1 and the presence of other brain anomalies.

The 3D-T1 was automatically segmented by using FreeSurfer 5.1.0 (http://surfer.nmr.mgh.harvard.edu/) in 84 regions (68 cortical and 16 subcortical), representing the network nodes used as seeds for connectome construction [Fischl et al. (2004)]. To compare the structural connectivity studies of patients and controls, we modified the virtual callosotomy approach used by Owen et al. (2013) simulating the segACC in each matched control (partial virtual callosotomy — PVC). In particular, in MRtrix3, we placed a manually drawn exclusion mask on the mid-sagittal plane over the exact callosal segment corresponding to the patient's agenetic callosum portion. The size and shape of the mask varied for each pair of matched controls on the basis of the specific type of segACC, effectively removing only the streamlines passing through the corresponding agenetic callosal segment.

The connectome edges were calculated by using probabilistic tractography performed with MRtrix3. The tracking results of each of the seeds were masked by each of the other 83 regions, referred to as targets, to obtain a connection strength between each seed and target pair, with the total number of streamlines connecting two regions as the connection strength. The 84×84 connection matrices were symmetric about the diagonal, and the matrix diagonal was set to zero. The connection strength was then divided by the sum of voxels in the seed and target regions to account for differences in volumes between various cortical and subcortical regions.

Individual and consensus connectomes were created for the 3 groups of subjects: patients with segACC, controls with PVC, and controls without PVC. In particular, we thresholded each individual connectome to remove the weakest connections, setting to zero all connection strengths that were $< 0.5\%$ of the maximum strength [Owen et al. (2013)]. The individual connectomes were then binarized setting to 1 all the non-zero connections. For each group, a consensus connectome was obtained by averaging the thresholded matrices of all subjects in the group; subsequently, all connections that were present in $< 75\%$ of the subjects in the group were removed from the group's consensus matrix. The consensus matrices were then binarized by setting to 1 all the non-zero connections.

6.2.3   Network and statistical analysis

For topology analysis, we calculated measures of structural segregation (clustering coefficient, transitivity, local efficiency, and modularity) and integration (mean degree, characteristic path length, mean normalized betweenness, global efficiency, and cost) for the binarized individual and consensus connectomes of subjects with segACC, PVC and controls, with the Brain Connectivity Toolbox (https://sites.google.com/site/bctnet).

In each group, hub nodes were separately identified for individual and consensus connectomes. A node in a single network (individual or consensus) was marked as a hub if its degree was 1 standard deviation higher than the mean degree of its network. To test the hypothesis that the segACC brain has higher within-group variability compared with controls, we assessed the spatial distribution of node degree by transforming the degrees of the 84 nodes in each connectome into a vector and by using the correlation coefficient in a pair-wise fashion between all individuals in each group [Owen et al. (2013)]. To measure network similarity, we calculated the connection strength correlation coefficient between each individual connectome and its group consensus connectome, as well as between every pair of individual connectomes in each group [Owen et al. (2013)].

Modularity and mean participation coefficient (quantifying the diversity of inter-modular connections) were calculated for each partitioning of the consensus and individual connectome [Rubinov and Sporns (2010)] To evaluate the stability of modular assignment, we computed the mean Hubert-Rand Index [Hubert and Baker (1977)] for each of the 3 groups: i) between the modular assignment for each of the individual connectomes and the assignment for the consensus connectome, and ii) pair-wise between the modular assignments for the individual connectomes [Owen et al. (2013)]. The Hubert-Rand index is an adjustment of the Rand index (measuring the similarity of two partitions of a dataset) that takes into account the probability of both agreement and disagreement between partitions [Hubert and Baker (1977)].

To subdivide the networks into non-overlapping modules, we applied the Louvain community detection algorithm with an iterative fine-tuning method by using the function provided by the Brain Connectivity Toolbox. The iterations were stopped when the modularity value did not change between steps.

Network-based statistics was performed to evaluate the differences in subnetworks between patients and PVC controls [Zalesky et al. (2010)]. The statistical model included a design matrix of 5 patients and 10 controls. We used a contrast vector [1, -1] to test for an increase of subnetwork connectivity in controls compared with patients, and a contrast vector [-1, 1] to test for the opposite hypothesis. A t-test was applied to assess the statistical

significance of between-group comparisons of the network metrics. For each metric, the data labels were randomly reassigned between the two groups and t-values were computed for each relabelling A total of 5000 permutations were performed to estimate the null distribution, and associations with $t > 3$ were analysed by network-based statistics. A family-wise error rate-corrected significance level of $p \leq 0.01$ was used.

To assess the statistical significance of between-group comparisons of the network metrics and the measures of connectome variability, we used a non-parametric permutation testing procedure. For each metric, the data labels were randomly reassigned between the two groups and t-values were computed for each relabelling, for a total of 5000 permutations. p-values were calculated on the basis of the distribution of t-values obtained from the permutations and were adjusted for multiple comparisons with a false-discovery rate correction. Statistical significance was set at $p < 0.05$. Data was analysed by using SPSS Statistics for Mac 21.0 (IBM, Armonk, New York).

6.3 Results

Clinical, genetic, and neuroradiological characteristics of patients with segACC are described in Table B.1 in Appendix B. On conventional imaging, in most patients (7/8; 87.5%), the agenetic segment corresponded to the posterior callosal body and the splenium was hypoplastic. In one patient (1/8; 12.5%), the anterior callosal body was additionally involved. Probst bundles were noted in all patients (8/8; 100%) at the level of the agenetic callosal segment on coronal images. The anterior commissure was hypoplastic in four cases (4/8; 50%). A colpocephalic appearance of the lateral ventricle was evident in three patients (3/8, 34.5%).

On constrained spherical deconvolution tractography, no callosal fibre tracts were detectable at the level of the thin lamina corresponding to the agenetic segment. Three malformative subtypes were identified on the basis of the relationship of the hippocampal commissure (HC) with the callosal remnants (Figure 6.1 and Figure B.2 in Appendix B): the HC lay beneath the anterior callosal remnant in three patients (segACC type I), while in three other patients, it was attached to the posterior callosal remnant (segACC type II). Finally, in two patients, the intermediate segment of the commissural plate was made of green-coded longitudinal bundles corresponding to the fornices joined in the midline, forming the HC (segACC type III).

According to the projection areas, the intermediate agenetic segment corresponded to fibres projecting to the parietal lobe in all patients with segACC and healthy controls after
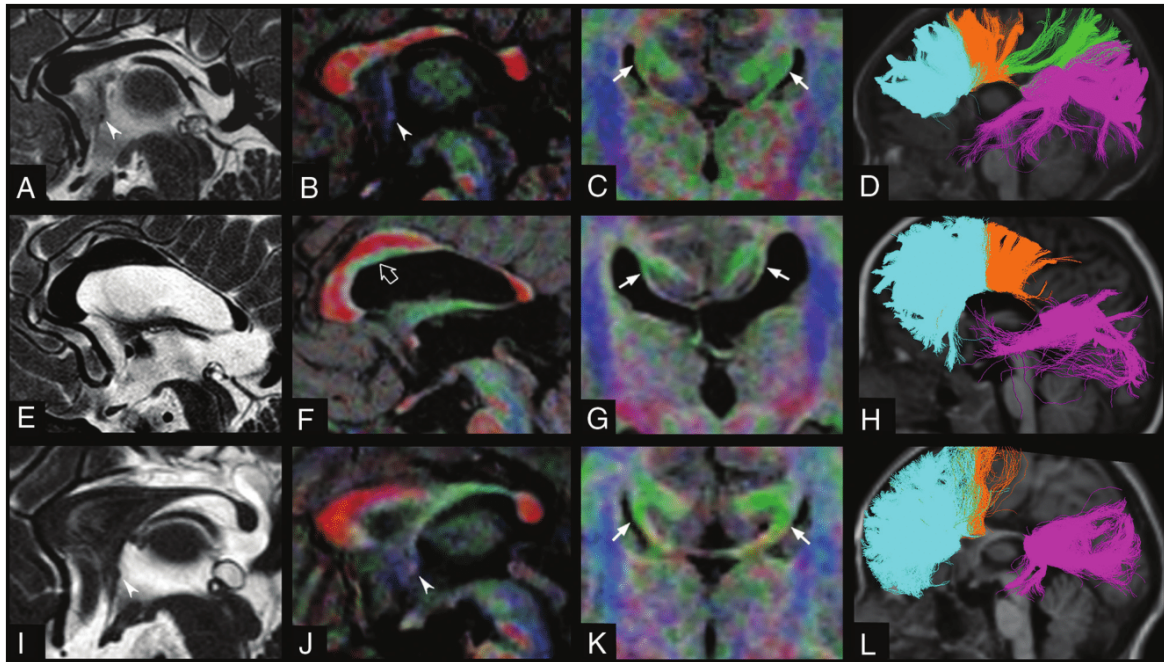
Figure 6.1 The 3 subtypes of segmental agenesis of the corpus callosum: SegACC type I in a 2-year-old girl (patient 3, A–D), segACC type II in a 5.4-year-old boy with Klippel-Feil syndrome (patient 5, E–H), and segACC type III in a 5.7-year-old boy with septo-optic dysplasia (patient 6, I–L). Midline sagittal T2 driven equilibrium (A, E, and I) and corresponding fractional anisotropy color directional maps fused with 3D-T1 (B, F, and J) reveal the focal absence of the posterior part of the callosal body in all patients. Hypoplasia of the anterior commissure may be associated, as shown in patient 3 (A and B, arrowhead) and patient 6 (I and J, arrowhead). Note the presence of a green-coded longitudinal bundle located in the inferior part of the anterior callosal segment, corresponding to an ectopic callosal bundle in patient 5 (F, empty arrow). Coronal fractional anisotropy color directional maps fused with 3D-T1 (C, G, and K) demonstrate Probst bundles, with variable thickness, at the level of agenetic callosal segments in the 3 patients (arrows). Tractographic reconstructions of callosal fibres overlaid on T1 (D, H, and L) show the homotopic callosal connections in the three patients. (D) In segACC type I, the anterior callosal remnant contains fibres connecting the anterior frontal, posterior frontal, and parietal lobes, while the posterior callosal segment contains fibres connecting the parieto-occipitotemporal lobes. In segACC types II (H) and III (L), the anterior callosal segments exclusively contain frontal callosal fibres, while the posterior callosal remnants contain fibres connecting the parieto-occipitotemporal lobes. In segACC type III (L), the intermediate segment of the commissural plate is made of green-coded bundles, corresponding to the fornices joined in the midline, forming the hippocampal commissure. The callosal fibres are coloured according to their projections to specific lobar areas (i.e., light blue for anterior frontal callosal fibres, orange for posterior frontal callosal fibres, green for parietal callosal fibres, and violet for occipitotemporal callosal fibres).

PVC. The hypoplastic posterior callosal remnants consistently connected the occipitotemporal lobes, while the anterior remnants always connected the frontal lobes, including the frontal associative regions and, in all except one case, the motor areas. In the three patients with segACC-type I, the anterior callosal remnants also contained splenial fibres connecting

	Consensus connectomes			Individual connectomes [Mean (SD)]			*P* values	
	Control	PVC	SegACC	Control	PVC	SegACC	SegACC vs Controls	SegACC vs PVC
Assortativity	0.03	−0.02	0.02	−0.02 (0.03)	−0.05 (0.03)	−0.02 (0.04)	0.815	0.379
Global efficiency	0.45	0.42	0.38	0.54 (0.02)	0.52 (0.02)	0.48 (0.03)	**0.005***	**0.024***
Mean local efficiency	0.69	0.7	0.71	0.77 (0.02)	0.77 (0.02)	0.75 (0.04)	0.553	0.597
Mean normalized betweenness	0.02	0.02	0.03	0.01 (0.0)	0.02 (0.0)	0.02 (0.0)	**0.001***	**0.031***
Characteristic path length	2.63	2.83	3.36	2.13 (0.09)	2.24 (0.13)	2.42 (0.12)	**0.002***	**0.021***
Transitivity	0.38	0.4	0.4	0.45 (0.02)	0.46 (0.02)	0.46 (0.04)	0.555	0.904
Mean clustering coefficient	0.49	0.51	0.53	0.56 (0.03)	0.57 (0.03)	0.57 (0.04)	0.905	0.929
Mean degree	8.64	8.17	7.31	14.71 (1.27)	13.66 (1.33)	12.02 (1.62)	**0.005***	0.054
Cost	0.21	0.2	0.18	.35 (0.03)	0.33 (0.03)	0.29 (0.04)	**0.005***	0.054

Table 6.1 Network metrics of consensus and individual connectomes. Bold font and asterisks indicate p-values which were statistically significant.

the occipitoparietal lobes. Segmental Probst bundles corresponding to the agenetic callosal segment were confirmed in all patients. These bundles merged anteriorly with the ventral callosal remnant and extended posteriorly to the parietal lobes. Callosal ectopic bundles were identified in three patients.

6.3.1 Network and statistical analysis

Table 6.1 reports the topology metrics of consensus and individual connectomes. Patients with SegACC had less integrated structural connectivity compared with those with PVC and controls. No significant differences in the segregation metrics were found among patients with segACC and PVC and controls.

Figures 6.2 and 6.3 show the hubs found respectively for the consensus and individual connectomes. The analysis of within-group variability revealed that the spatial distribution of node degrees was significantly more variable in segACC, as demonstrated by a lower mean correlation coefficient ($r = 0.634 \pm 0.089$), compared with both controls ($r = 0.735 \pm 0.052$) and subjects with PVC ($r = 0.729 \pm 0.066$) at $p < 0.05$.

There were no differences in the connection strength correlation coefficients between the consensus network and each individual network, indicating that the consensus connectomes represented individuals in their group to approximately the same extent. Conversely, the inter-individual variability of the segACC connectome was greater than that of the control and PVC connectomes, as shown by a significantly lower consistency between individual networks ($p < 0.05$, Table B.2 in Appendix B).

The mean and standard deviation of modularity-related metrics are provided in Table 6.2. Six modules were identified in the consensus network of controls and those with PVC, while only 5 were found in patients with segACC, due to disruption of the module corresponding to the structural core (Figure 6.4 and Tables B.3-B.5 in Appendix B).

	Control [Mean (SD)]	PVC [Mean (SD)]	SegACC [Mean (SD)]	P values	
				SegACC vs Controls	SegACC vs PVC
Modularity	0.38(0.02)	0.41(0.03)	0.44(0.03)	**0.002***	0.151
Participation coefficient	0.39(0.05)	0.31(0.07)	0.28(0.04)	**0.003***	0.335
HRI (vs consensus)	0.53(0.05)	0.54(0.08)	0.58(0.09)	0.311	0.394
HRI (vs individual)	0.63(0.03)	0.61(0.06)	0.68(0.02)	**0.009***	**0.017***

Table 6.2 Modularity metrics of individual connectomes. SD: Standard deviation. HRI: Hubert-Rand Index. Bold font and asterisks indicate *p*-values which were statistically significant.

Network-based statistics identified 3 subnetworks of decreased connectivity in patients compared with controls (Figure 6.5 and Table 6.3).

Node 1	Node 2	*t* test value	*P* value
Network 1			0.001
L inferoparietal	L lingual	6.24	
L lingual	L middle temporal	5.89	
L paracentral	L postcentral	5.89	
L hippocampus	L middle temporal	4.16	
L paracentral	L amygdala	3.61	
L inferoparietal	L postcentral	3.61	
L paracentral	L middle temporal	3.53	
L pallidum	L medio-orbitofrontal	3.53	
L paracentral	R hippocampus	3.53	
L hippocampus	L thalamus proper	3.53	
L middle occipital	L medio-orbitofrontal	3.53	
L putamen	L pallidum	3.18	
L paracentral	L medio-orbitofrontal	3.18	
Network 2			0.009
L superior frontal	R rostral middle frontal	3.53	
R posterior cingulate	R rostral anterior cingulate	3.53	
R isthmus cingulate	R rostral anterior cingulate	3.53	
L rostral middle frontal	R rostral middle frontal	3.18	
R rostral anterior cingulate	R rostral middle frontal	3.18	
Network 3			0.01
R lingual	R insula	3.61	
R middle temporal	R lingual	3.61	
R middle temporal	R temporal pole	3.53	
R middle occipital	R insula	3.18	

Table 6.3 Subnetworks with decreased connectivity in patients with SegACC compared with controls with partial virtual callosotomy.
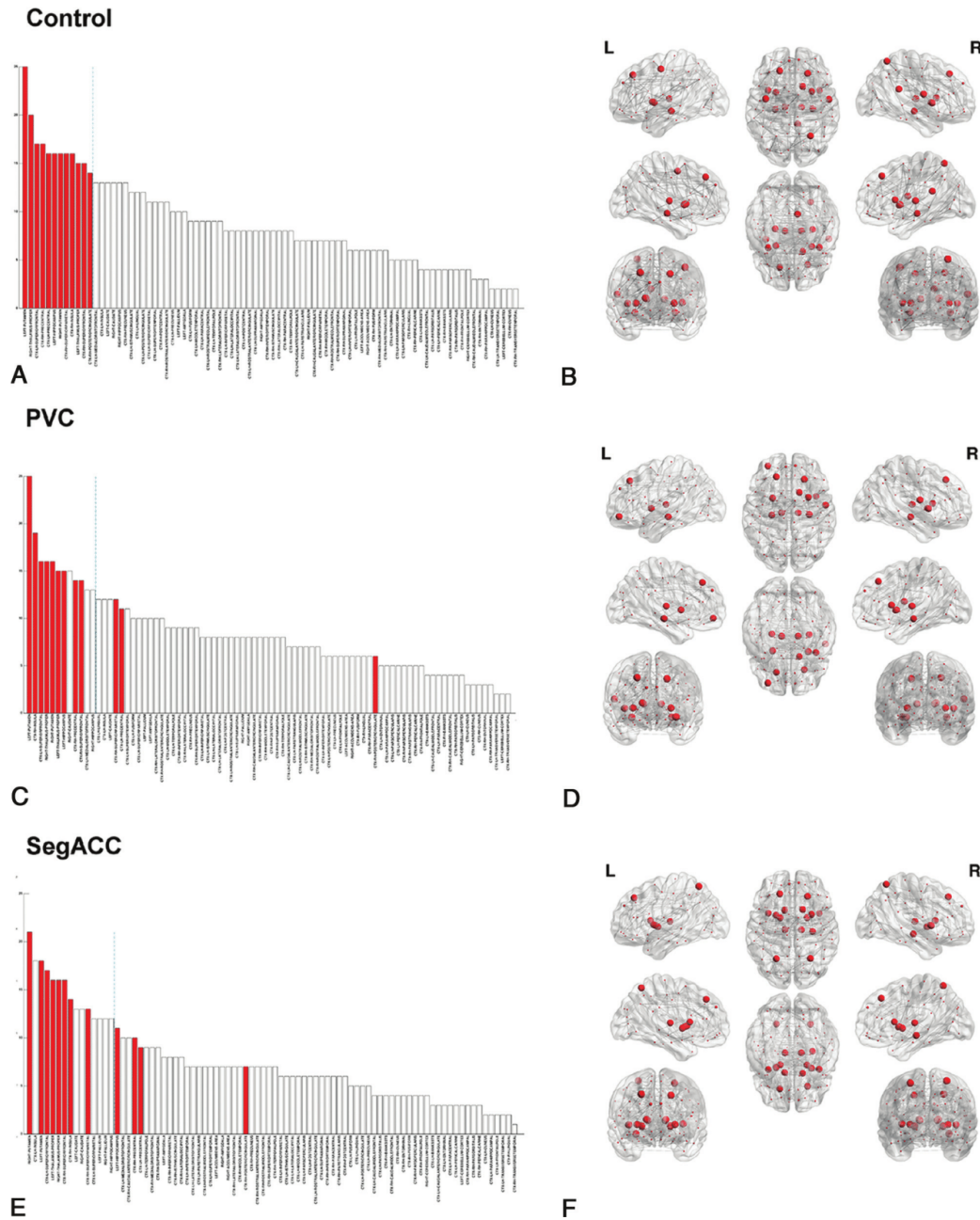
Figure 6.2 Hubs for the consensus connectomes in the control (A and B), PVC (C and D), and segACC (E and F) groups. The bar graphs reveal the degree of distribution across nodes for the consensus connectomes (A, C, and E): the red bars demonstrate the nodes with degrees greater than mean plus 1 standard deviation for the control consensus connectome in A. The dashed lines demonstrate the cut-off for mean plus 1 standard deviation in the PVC controls and patients with segACC. The red bars in C and E show the redistribution of hub regions in the PVC and segACC consensus connectomes, compared with control consensus connectomes: any red node appearing to the right of the dashed line has been demoted from hub status and any white bar to the left of the dashed line is a node that has been promoted to a hub. The 3D schematic graphs depict the spatial distribution of hubs (represented by larger red circles) within the corresponding consensus connectomes (B, D, and F).
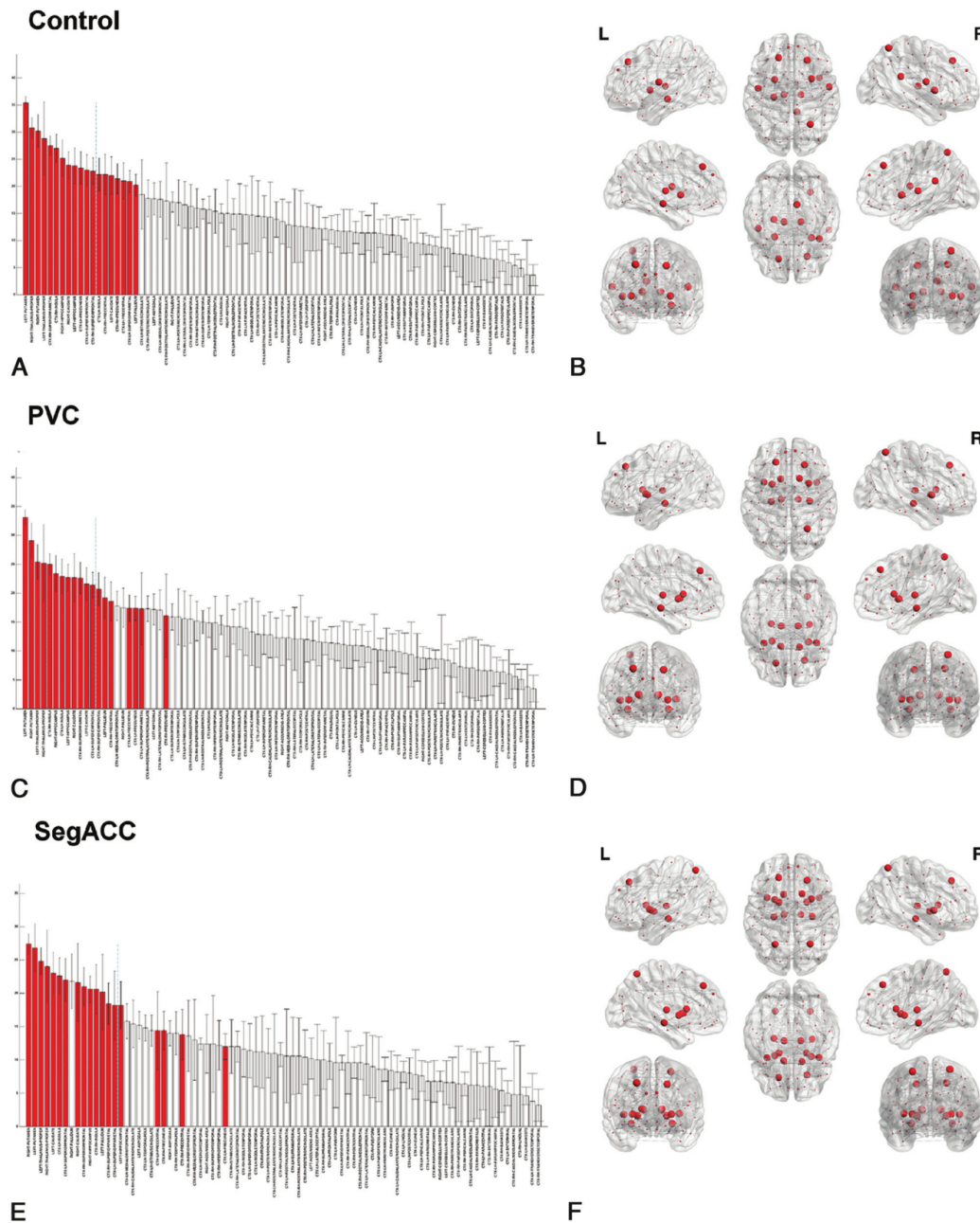
Figure 6.3 Hubs for individual connectomes in the control (A and B), partial virtual callosotomy (C and D), and segmental callosal agenesis (E and F) groups. The bar graphs reveal the mean degree of distribution across nodes for the individual connectomes with standard deviation error bars (A, C, and E): the red bars demonstrate the nodes with a degree greater than mean plus 1 standard deviation for the controls (A). The dashed lines demonstrate the cut-off for mean plus 1 standard deviation for the PVC and for segACC. The red bars in C and E show the redistribution of regions in the individual connectomes of the PVC and segACC groups, respectively, compared with the hubs in the individual connectomes of control subjects: any red node appearing to the right of the dashed line has been demoted from hub status, and any white bar to the left of the dashed line is a node that has been promoted to hub. The 3D schematic graphs depict the spatial distribution of hubs (represented by larger red circles) within the corresponding individual connectomes (B, D, and F).
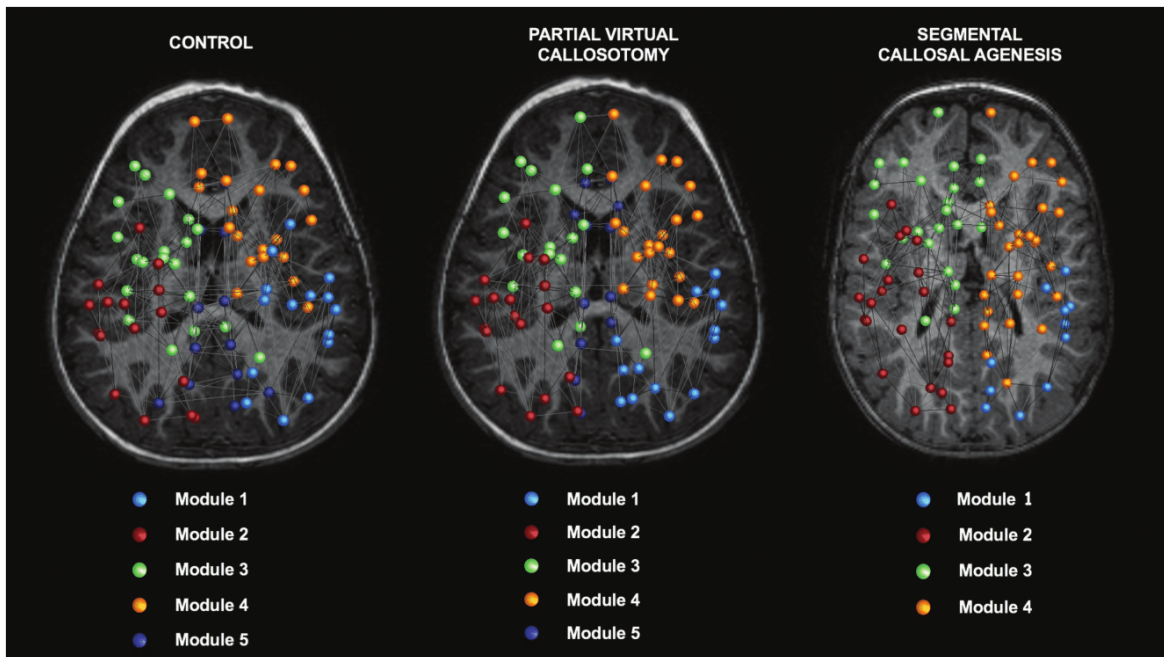
Figure 6.4 Module assignments for the consensus connectomes. Topology analysis of network modules reveals 5 modules for the control and partial virtual callosotomy groups and 4 modules for patients with segACC. Modules 3 and 4 largely consist of frontal nodes, while modules 1 and 2 are more posterior. Note that module 5, corresponding to the "structural core" of the network, is not present in the segACC consensus connectome. The 82 nodes are plotted with a circle coloured according to the community to which it was assigned. For the complete list of the regions included in each module, refer to Tables B.3-B.5 in Appendix B.
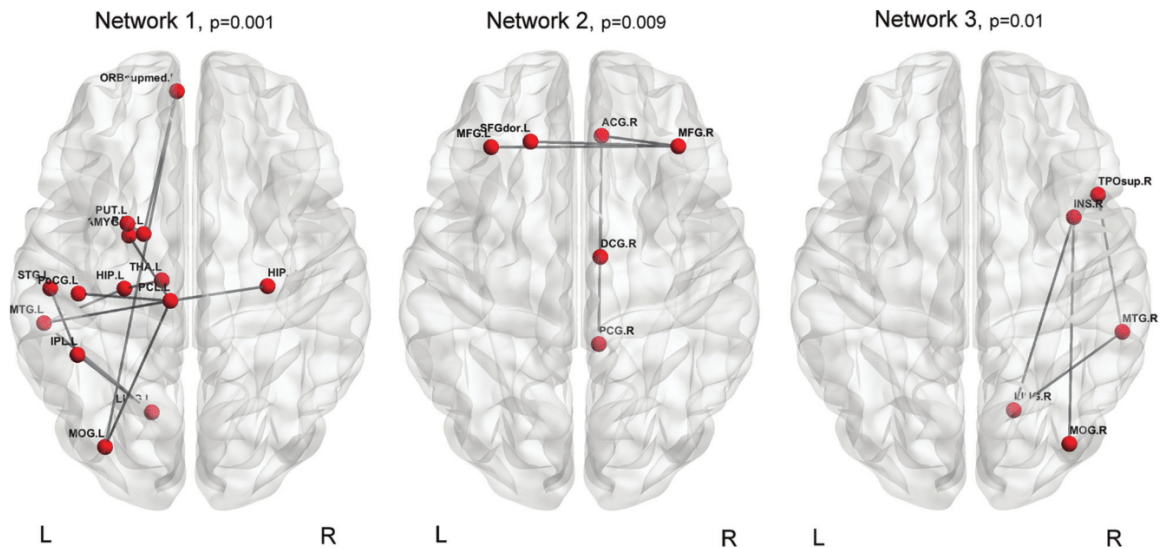
Figure 6.5 Subnetworks with decreased connectivity in patients with SegACC compared with controls with partial virtual callosotomy. Networks 1 and 3 are prevalently intra-hemispheric and involve the temporoinsular and nuclear regions, while network 2 is inter-hemispheric and connects the frontal lobes and right cingulum.

Part III

Discussion

Chapter 7

Conclusions

7.1 Main results

The main results of this PhD thesis can be summed up as: i) the characterisation of the statistical correlation between structural and functional connectivity in healthy adult subjects, using structural and functional analysis methods with higher precision and resolution than the methods most often used in literature; ii) the application of CSD-PT-based WM tracts reconstruction to neonatal and paediatric clinical data, with methods which are never applied in the clinical environment and overcoming the obstacles posed by its constraints; iii) the further characterisation of structural connectivity modifications brought by segmental agenesis of the corpus callosum, their effect on patients' functionality and the differences with the modifications and functional manifestations caused by complete agenesis of the corpus callosum.

7.2 Part I – Relation between structural and functional connectivity in the healthy adult

The first approach to the relationship between brain structure and function is almost always done on healthy adult subjects, to obtain a baseline description of the brain's workings. While analysis of diffusion MRI data is currently the only way to compute structural connectivity in vivo, many techniques exist to study functional connectivity, often converging to the same results [Hamandi et al. (2008); Garcés et al. (2016)]. Non-invasive methods such as BOLD-fMRI and scalp EEG suffer from different and opposite resolution problems, which

are overcome by the use of intra-cerebral electrodes in epileptic patients who will undergo surgery.

In the work presented in Chapter 4, I compared the structural connectomes of 57 healthy adult subjects from the HCP Young Adult Project with resting-state functional connectomes from 67 adult subjects affected by drug resistant focal epilepsy, implanted with intra cerebral electrodes for SEEG recording. All non-typical activity was removed from the SEEG recordings prior to computation of functional connectivity, effectively removing all contributions of epileptic activity from the data. I computed structural connectomes from DWI data downloaded from the HCP database, processed with CSD-PT, and analysed statistical correlation between average group connectivity matrices at three different granularity levels: a global comparison, a single-node-level analysis and a study of the community structure of both networks and of their correlation.

Global comparison between average structural and functional networks yields significant positive correlation for all parcellation schemes and FC acquisition frequencies, with values of the coefficient higher than 0.5 for the function-based parcellation scheme. This positive correlation does not vary at different densities of the original networks, suggesting it is driven by hub nodes presenting very high degree. It also does not vary strongly across different acquisition frequencies, while there is a higher variability across subjects, shown by the wide confidence intervals. The visual comparison between structural and functional average networks suggests that the structural connectivity — especially edges with high weights — might be the 'base' for functional connectivity, which can then be established also between areas not directly connected by WM fibres.

Node-wise correlation coefficients show several nodes with very high values of structural-functional correlation, up to 0.95 ($p < 0.02$, Pearson correlation test), and a few nodes with very low coefficients (minimum 0.2, $p < 0.02$, Pearson correlation test), varying quite coherently across four ranges of FC acquisition frequencies. The higher correlation coefficients are concentrated in the fronto-temporal and occipital lobes of the brain, while lower correlation is found for nodes in the parietal lobe: the regions of high correlation re located in the areas which define the Default Mode Network [Greicius et al. (2003)], a functional subnetwork linked to resting-state brain activity, where a good correspondence of structural and resting-state functional connectivity has been demonstrated [Greicius et al. (2009)]. This result is reasonable since the SEEG data acquisition was done with the patients in a resting-state condition, with eyes closed: the resulting connectomes can be seen as 'resting-state connectomes', reflecting the functional organisation in a 'default' state of rest, which appears to be strongly linked with the structural organisation of the brain. The

variability of correlation across nodes further confirm the hypothesis that the relationship between structural and functional organization is driven by a few hub nodes, composing the 'core' of the networks.

Community analysis revealed a strong modularity for structural networks (max 0.81 left, 0.74 right hemisphere), with a subdivision into five modules well responding to previous studies on both structural and functional connectivity [Hagmann et al. (2008); Owen et al. (2013)] and a slightly lower community structure in functional networks, with a smaller number of bigger modules (maximum modularity 0.50 left, 0.58 right hemisphere). The functional partition with the best modularity value for the right hemisphere was again composed of five modules, confirming the results from the previously cited works; the optimal partition for the left hemisphere, on the other hand, was composed of only two big modules. This might be caused by an uneven sampling of the brain's left hemisphere, which is often less implanted than the right hemisphere because of the high number of eloquent cortex areas present in the left side of the brain. We compared partitions of structural and functional networks composed of seven modules with the subdivision of the brain in seven subnetworks from Yeo et al. (2011), finding a good correspondence of module edges with the ones defined in the cited work. Comparison of partitions obtained from structural and functional networks produced a maximum normalized mutual information index of 0.79 for the left and 0.73 for the right hemisphere, corresponding to partitions of five to seven modules. This suggests a similar organization of structural and functional modules in both hemispheres. This similarity seems to increase with the number of modules detected in the networks, while for a lower number of modules the similarity decreases. This result, coupled with previous observations and subdivisions of the brain network with respect to functional characteristics [Yeo et al. (2011)], seems to suggest the existence of many functional sub-areas, well segregated with respect to each other, and supported by a similar subdivision of the structural network. It has been shown that single-edge-level analysis is often not enough to capture the relationship between brain structure and function [Mišić et al. (2016)]; the results of our global analysis were both confirmed and expanded by the analyses of other levels of connectivity, from single-node to community level, giving more information on the separate connectivities and on how they relate to one another.

This first part of the work established the existence of a strong relationship between structural and functional brain connectivity and showed that CSD-PT and SEEG can be used to investigate this link more finely than other methodologies, such as functional MRI and DTI, which suffer from known problems such as a poor temporal resolution and a too simplistic modelling of the diffusion MRI signal, producing low-quality reconstructions.

In the following part of the thesis, the analysis has focused on the application of these methods to the neonatal and paediatric age, and in particular to the computation of structural connectivity from paediatric clinical data with the advanced diffusion imaging used in this first part of the work.

7.3 Part II – Structural connectivity and its influence on function in the healthy and pathological child

While functional connectivity in children and neonates can be studied with the same methods applied in adults in the first part of this work [Cossu et al. (2008); Taussig et al. (2014); Vanhatalo and Kaila (2006)], the same cannot be said for advanced diffusion imaging methods for structural connectivity analysis. The second part of this thesis has focused on the adaptation and application of CSD-PT to diffusion MRI data of paediatric patients acquired with sequences commonly used in the clinical environment, where classical DTI is almost always the chosen method of WM and connectivity analysis. This part of the thesis has been developed in collaboration with the Neuroradiology Unit at the Giannina Gaslini Hospital in Genova.

7.3.1 Feasibility of advanced diffusion imaging in paediatric clinical data

In the work described in Chapter 5 we compared the reconstructions of three major WM tracts — cerebellar-thalamic tracts, cortico-ponto-cerebellar tracts, and corticospinal tracts — obtained with DTI and CSD-PT in 50 myelinated and unmyelinated subjects, scoring them on a five-points scale [Beddy et al. (2011)]. The diffusion MRI images from all subjects were acquired with a 1.5T scanner, using a sequence with suboptimal acquisition parameters (34 gradient directions, b-value 1000 s/mm^2) commonly applied during exams at the Gaslini Hospital. Color-coded maps have been computed using the Track-Density Imaging (TDI) framework [Calamante et al. (2010)], to compare the results with DTI eigenvector maps commonly used in diagnostic practice.

While both methodologies were able to reconstruct the tracts in all cases, lower scores were more frequently awarded to DTI reconstructions, and the frequency of higher scores was higher for CSD-PT reconstructions. DTI reconstructions appeared often thinner and

with reduced volumes with respect to known anatomy, especially for unmyelinated subjects, while CSD-PT fully characterized the tracts even in the younger subjects.

We found that TDI maps provide WM images of high quality and higher spatial resolution than the original diffusion-weighted data. TDI is performed by mapping reconstructed WM tracks to an image in which the intensity of each voxel reflects the number of tracks passing through that specific position in space [Calamante et al. (2010)]. A major advantage of this method is that TDI maps can be computed with a voxel size smaller than the original DWI data, thanks to the interpolation strategy used, thus allowing a better visualization of the results. Directionally encoded colour maps can be computed by assigning a colour to each spatial direction, and then colouring the map voxels with the correct colour depending on the directionality of the fibres in the voxel. The TDI maps presented a higher resolution and image quality with respect to eigenvector maps, allowing to precisely individuate anatomical structures which appeared blurred on indistinguishable in eigenvector maps. The use of TDI maps in place of eigenvector maps allows clinicians to better characterise the WM density and direction in each location of the brain and to better delineate anatomical structures of interest, either for diagnostic purposes or to better individuate ROIs for subsequent research work.

Our results corroborate the hypothesis that CSD-PT can be successfully applied using routine clinical MR protocols with low angular resolution and low b-value, even in paediatric subjects. The advantages of CSD-PT over DTI can thus be exploited in a clinical environment to investigate structural brain connectivity, both in health and pathology. Further refinements to the CSD-PT reconstructions may be obtained using additional frameworks; for example, Anatomically Constrained Tractography (ACT) [Smith et al. (2012)] incorporates anatomical priors from a tissue segmentation of a T1 image into the tractography process, in order to improve streamline termination criteria and the biological accuracy of the resulting tractograms. Another interesting method to eliminate reconstruction bias and improve biological plausibility of the tractograms is the Spherical-deconvolution Informed Filtering of Tractograms (SIFT) developed by Smith et al. (2013). As discussed in the study by Calamante et al. (2015), the application of these two methods also greatly improves the biological meaning of TDI maps and quantitative investigations on these maps. The anatomical information added by the tissue maps used in ACT allows streamlines passing through non-WM regions or having implausible trajectories to be rejected, while SIFT allows to reduce the bias toward major WM tracts in tractography reconstructions.

These two frameworks were incorporated in the analysis pipeline in a following work with the Gaslini hospital, in order to confirm the good results obtainable with CSD-PT on

paediatric clinical data and the applicability of this methodology to investigate structural connectivity in such an environment. For this study, we chose to apply this method to investigate structural connectivity and its modifications in a cohort of patients suffering from a congenital malformation of the corpus callosum: segmental agenesis of the corpus callosum.

7.3.2 Modifications in structural connectivity in segmental callosal agenesis

Segmental agenesis of the corpus callosum (segACC) is a specific form of partial callosal agenesis (ACC) where only the central portion of the corpus callosum is missing, causing a disconnection between the anterior and posterior segments. Despite the growing interest this malformation has garnered in the past years after the advent of high-angular-resolution diffusion imaging, little is still known about the modifications to structural connectivity it can cause. Graph-based structural analysis has helped characterize ACC structural abnormalities, revealing a decrease in global efficiency and a correspondent increase in local connectivity measures, along with higher variability in individual connectomes compared with healthy controls [Owen et al. (2013); Meoded et al. (2015); Jakab et al. (2015)].

In the last part of this thesis, presented in Chapter 6, we compared the structural connectivity of 5 patients diagnosed with segACC with that of 10 age- and sex-matched healthy controls, before and after virtual removal of the same section of the corpus callosum missing in the corresponding segACC patient (partial virtual callosotomy — PVC group). The structural connectomes were obtained from diffusion MRI data acquired at the Gaslini hospital, with the CSD-PT methodology adapted and validated in the previous part of the work. This allowed to fully characterize the WM connections between cortical areas and to apply network-based analyses to both groups, comparing network metrics and community structure.

As described in previous works [Owen et al. (2013)], we found a significant decrease in network integration, with decreased global efficiency metrics and increased path length and mean normalized betweenness. This has been shown to be a result of missing long-range inter-hemispheric callosal fibres [Owen et al. (2013); Meoded et al. (2015)]. However, while high-functioning ACC adults in the study by Owen et al. (2013) also showed an increase in local efficiency and segregation metrics, reflecting a profound rearrangement of cortical and subcortical connectivity, in our patients there was no such increase. This likely indicates that the compensatory WM rewiring mechanisms, demonstrated by the presence of Probst bundles and heterotopic callosal connections, were insufficient to compensate the absence

of direct inter-hemispheric callosal tracts; this was confirmed by the decreased connectivity found in three subnetworks related to cognitive, memory and language functions, and further supported by the presence of psychomotor delay in all patients and a worse neurologic prognosis than the adults with ACC studied in Owen et al. (2013). This is likely due to the fact that the compensatory rewiring mechanisms described in ACC patients have a high cost in terms of brain reorganization: while complete ACC can trigger this compensation because of its higher severity in terms of decreased connectivity, the absence of only part of the callosal fibres might not be enough to initiate the rewiring process, causing more severe disruption to connectivity and cognitive functions.

This work also demonstrated that the structural connectivity of segACC subjects was different from that of normally developing controls based on local changes in brain regions that normally serve as connection hubs [Hagmann et al. (2010)]. The so-called 'hub' nodes are hyper-connected nodes through which a high number of paths between other nodes pass. In particular, the cortical and subcortical hubs which were demoted or promoted from their statuses were different in the segACC group compared with the PVC group, indicating that network topology reorganization in segACC may not be explained only by the exclusion of callosal fibres from the normal brain [Owen et al. (2013)]. Moreover, we found an increased connectome variability in segACC, with higher variability in the spatial distribution of node degree and in correlation strengths in patients compared with controls, confirming results recently found both in adults and fetuses with ACC [Owen et al. (2013); Jakab et al. (2015)]. This might be due by a very wide variety of causes, from the connection variability of Probst bundles [Tovar-Moll et al. (2006)] to alternative tracts being generated through different parts of the brain in different subjects [Tovar-Moll et al. (2006); Tovar-Moll et al. (2014)].

We also found a lower number of modules and a higher intra-group correspondence in patients with segACC compared with PVC and controls. These findings suggest that neural plasticity in segACC reorganizes structural connectivity in an almost stereotyped way, causing the loss of a distinct posterior medial module corresponding to the structural core of the human brain, which comprises highly connected and central regions of the cortex [Hagmann et al. (2008)]. In particular, portions of posterior medial cortex, such as the posterior cingulate cortex, the precuneus, and the lateral and medial parietal cortex are key core components known to be highly activated at rest in the Default Mode Network. Therefore, it has been suggested that the structural core may have a central role in integrating information across functionally segregated brain regions [Hagmann et al. (2008)]. Owen et al. (2013) demonstrated a weakened structural core in adults with ACC associated with reduced connectivity between regions of the cingulate cortex. Most interesting, the focal absence of

callosal fibres connecting the parietal lobes in segACC may also disrupt the structural core and contribute to the impairment of large-scale brain dynamics in these patients.

This thesis further elucidates the relationship between structural and functional connectivity in the adult subject, demonstrating the existence of a robust statistical correlation between the two which is maintained at different levels of aggregation. It also poses the basis for investigation of structural and functional networks in the neonatal and paediatric subject in the clinical environment: by solving the problems posed by the sub-optimality of data from the paediatric clinical environment, it allows to apply advanced diffusion imaging methods in the clinical activity, in order to better investigate structural connectivity — and to elucidate its relationship with functional connectivity — in the healthy and pathological paediatric patient.

References

Abhinav, K., Yeh, F. C., Pathak, S., Suski, V., Lacomis, D., Friedlander, R. M., and Fernandez-Miranda, J. C. (2014). Advanced diffusion MRI fiber tracking in neurosurgical and neurodegenerative disorders and neuroanatomical studies: A review. *Biochimica et Biophysica Acta - Molecular Basis of Disease*, 1842(11):2286–2297.

Achard, S. and Bullmore, E. (2007). Efficiency and cost of economical brain functional networks. *PLoS computational biology*, 3(2):e17.

Addis, D. R., Moscovitch, M., and McAndrews, M. P. (2007). Consequences of hippocampal damage across the autobiographical memory network in left temporal lobe epilepsy. *Brain*, 130(9):2327–2342.

Akaike, H. (1974). A new look at the statistical model identification. *IEEE Transactions on Automatic Control*, 19(6):716–723.

Alexander, D., Barker, G., and Arridge, S. (2002). Detection and modelling of non-gaussian apparent diffusion coefficient profiles in human brain data. *Magnetic Resonance in Medicine: An Official Journal of the International Society for Magnetic Resonance in Medicine*, 48(2):331–340.

Andrews-Hanna, J. R., Snyder, A. Z., Vincent, J. L., Lustig, C., Head, D., Raichle, M. E., and Buckner, R. L. (2007). Disruption of large-scale brain systems in advanced aging. *Neuron*, 56(5):924–935.

Arnulfo, G., Wang, S. H., Williams, N., Hirvonen, J., Fato, M. M., Nobili, L., Cardinale, F., Rubino, A., Zhigalov, A., Palva, S., and Palva, J. M. (2018). Long-range phase synchronization of high-gamma activity in human cortex. *bioRxiv*.

Audoin, B., Guye, M., Reuter, F., Confort-Gouny, S., Malikova, I., Soulier, E., Viout, P., Chérif, A. A., Cozzone, P. J., Pelletier, J., et al. (2007). Structure of wm bundles constituting the working memory system in early multiple sclerosis: a quantitative dti tractography study. *Neuroimage*, 36(4):1324–1330.

Auriat, A. M., Borich, M. R., Snow, N. J., Wadden, K. P., and Boyd, L. A. (2015). Comparing a diffusion tensor and non-tensor approach to white matter fiber tractography in chronic stroke. *NeuroImage: Clinical*, 7:771–781.

Backes, W. H., Besseling, R. M. H., Jansen, J. F. A., Overvliet, G. M., van der Kruijs, S. J. M., Ebus, S. C. M., de Louw, A. J. A., Hofman, P. A. M., Aldenkamp, A. P., and Backes, W. H. (2014). Delayed convergence between brain network structure and function in rolandic epilepsy. *Frontiers in human neuroscience*, 8(September):1–9.

Barkovich, A. J. and Kjos, B. (1988). Normal postnatal development of the corpus callosum as demonstrated by mr imaging. *American Journal of Neuroradiology*, 9(3):487–491.

Basser, P. J., Mattiello, J., and LeBihan, D. (1994). MR diffusion tensor spectroscopy and imaging. *Biophysical journal*, 66(1):259.

Bassett, D. S., Meyer-Lindenberg, A., Achard, S., Duke, T., and Bullmore, E. (2006). Adaptive reconfiguration of fractal small-world human brain functional networks. *Proceedings of the National Academy of Sciences*, 103(51):19518–19523.

Batalle, D., Hughes, E. J., Zhang, H., Tournier, J.-D., Tusor, N., Aljabar, P., Wali, L., Alexander, D. C., Hajnal, J. V., Nosarti, C., Edwards, A. D., and Counsell, S. J. (2017). Early development of structural networks and the impact of prematurity on brain connectivity. *NeuroImage*, 149(January):379–392.

Beare, R., Adamson, C., Bellgrove, M. A., Vilgis, V., Vance, A., Seal, M. L., and Silk, T. J. (2016). Altered structural connectivity in ADHD: a network based analysis. *Brain Imaging and Behavior*, pages 1–13.

Beddy, P., Rangarajan, R. D., Kataoka, M., Moyle, P., Graves, M. J., and Sala, E. (2011). T1-weighted fat-suppressed imaging of the pelvis with a dual-echo Dixon technique: initial clinical experience. *Radiology*, 258(2):583–589.

Bedeschi, M. F., Bonaglia, M. C., Grasso, R., Pellegri, A., Garghentino, R. R., Battaglia, M. A., Panarisi, A. M., Di Rocco, M., Balottin, U., Bresolin, N., et al. (2006). Agenesis of the corpus callosum: clinical and genetic study in 63 young patients. *Pediatric neurology*, 34(3):186–193.

Blondel, V. D., Guillaume, J.-L., Lambiotte, R., and Lefebvre, E. (2008). Fast unfolding of communities in large networks. *Journal of Statistical Mechanics: Theory and Experiment*, 2008(10):P10008.

Buzsáki, G. and Mizuseki, K. (2014). The log-dynamic brain: how skewed distributions affect network operations. *Nature Reviews Neuroscience*, 15(4):264.

Calamante, F., Smith, R. E., Tournier, J.-d., Raffelt, D., and Connelly, A. (2015). Quantification of voxel-wise total fibre density: Investigating the problems associated with track-count mapping. *NeuroImage*, 117:284–293.

Calamante, F., Tournier, J.-D., Jackson, G. D., and Connelly, A. (2010). Track-density imaging (TDI): Super-resolution white matter imaging using whole-brain track-density mapping. *NeuroImage*, 53(4):1233–1243.

Calamante, F., Tournier, J.-D., Kurniawan, N. D., Yang, Z., Gyengesi, E., Galloway, G. J., Reutens, D. C., and Connelly, A. (2012). Super-resolution track-density imaging studies of mouse brain: Comparison to histology. *NeuroImage*, 59(1):286–296.

Cammoun, L., Gigandet, X., Meskaldji, D., Thiran, J. P., Sporns, O., Do, K. Q., Maeder, P., Meuli, R., and Hagmann, P. (2012). Mapping the human connectome at multiple scales with diffusion spectrum MRI. *Journal of Neuroscience Methods*, 203(2):386–397.

Catani, M. and de Schotten, M. T. (2008). A diffusion tensor imaging tractography atlas for virtual in vivo dissections. *Cortex*, 44(8):1105–1132.

Cohen, J. (1960). A coefficient of agreement for nominal scales. *Educational and psychological measurement*, 20(1):37–46.

Cohen, M. X., Elger, C. E., and Weber, B. (2008). Amygdala tractography predicts functional connectivity and learning during feedback-guided decision-making. *Neuroimage*, 39(3):1396–1407.

Cossu, M., Lo Russo, G., Francione, S., Mai, R., Nobili, L., Sartori, I., Tassi, L., Citterio, A., Colombo, N., Bramerio, M., Galli, C., Castana, L., and Cardinale, F. (2008). Epilepsy Surgery in Children: Results and Predictors of Outcome on Seizures. *Epilepsia*, 49(1):65–72.

Daducci, A., Canales-Rodríguez, E. J., Zhang, H., Dyrby, T. B., Alexander, D. C., and Thiran, J.-P. (2015). Accelerated Microstructure Imaging via Convex Optimization (AMICO) from diffusion MRI data. *NeuroImage*, 105:32–44.

Daducci, A., Descoteaux, M., Garyfallidis, E., Gur, Y., Lin, Y.-C., Mani, M., Merlet, S., Paquette, M., Ramirez-Manzanares, A., Reisert, M., Rodrigues, P. R., Sepehrband, F., Caruyer, E., Choupan, J., Deriche, R., Jacob, M., Menegaz, G., Rivera, M., Wiaux, Y., and Thiran, J.-P. (2014). Quantitative Comparison of Reconstruction Methods for Intra-Voxel Fiber Recovery From Diffusion MRI. *IEEE Transactions on Medical Imaging*, 33(2):384–399.

Damoiseaux, J. S. and Greicius, M. D. (2009). Greater than the sum of its parts: a review of studies combining structural connectivity and resting-state functional connectivity. *Brain Structure and Function*, 213(6):525–533.

Desikan, R. S., Ségonne, F., Fischl, B., Quinn, B. T., Dickerson, B. C., Blacker, D., Buckner, R. L., Dale, A. M., Maguire, R. P., and Hyman, B. T. (2006). An automated labeling system for subdividing the human cerebral cortex on MRI scans into gyral based regions of interest. *Neuroimage*, 31(3):968–980.

Destrieux, C., Fischl, B., Dale, A., and Halgren, E. (2010). Automatic parcellation of human cortical gyri and sulci using standard anatomical nomenclature. *Neuroimage*, 53(1):1–15.

Dhollander, T., Raffelt, D., and Connelly, A. (2016). Unsupervised 3-tissue response function estimation from single-shell or multi-shell diffusion MR data without a co-registered T1 image. *ISMRM Workshop on Breaking the Barriers of Diffusion MRI*, page 5.

Dobyns, W. (1996). Absence makes the search grow longer. *American journal of human genetics*, 58(1):7.

Draganski, B., Gaser, C., Busch, V., Schuierer, G., Bogdahn, U., and May, A. (2004). Neuroplasticity: changes in grey matter induced by training. *Nature*, 427(6972):311.

Farquharson, S., Tournier, J.-D., Calamante, F., Fabinyi, G., Schneider-Kolsky, M., Jackson, G. D., and Connelly, A. (2013). White matter fiber tractography: why we need to move beyond DTI. *Journal of neurosurgery*, 118(6):1367–77.

Fischl, B., Salat, D. H., Van Der Kouwe, A. J., Makris, N., Ségonne, F., Quinn, B. T., and Dale, A. M. (2004). Sequence-independent segmentation of magnetic resonance images. *Neuroimage*, 23:S69–S84.

Fleiss, J. L., Levin, B., and Paik, M. C. (2003). *Statistical Methods for Rates and Proportions*. Wiley Series in Probability and Statistics. John Wiley & Sons, Inc., Hoboken, NJ, USA.

Friston, K. J. (1994). Functional and Effective Connectivity in Neuroimaging: A Synthesis. *Human Brain Mapping*, 2(1):56–78.

Garcés, P., Pereda, E., Hernández-Tamames, J. A., Del-Pozo, F., Maestú, F., and Ángel Pineda-Pardo, J. (2016). Multimodal description of whole brain connectivity: A comparison of resting state MEG, fMRI, and DWI. *Human Brain Mapping*, 37(1):20–34.

Glasser, M. F., Coalson, T. S., Robinson, E. C., Hacker, C. D., Harwell, J., Yacoub, E., Ugurbil, K., Andersson, J., Beckmann, C. F., Jenkinson, M., et al. (2016). A multi-modal parcellation of human cerebral cortex. *Nature*, 536(7615):171–178.

Gordon, A. L., Wood, A., Tournier, J.-D., and Hunt, R. W. (2012). Corticospinal tract integrity and motor function following neonatal stroke: A case study. *BMC Neurology*, 12(1):53.

Greicius, M. D., Krasnow, B., Reiss, A. L., and Menon, V. (2003). Functional connectivity in the resting brain: A network analysis of the default mode hypothesis. *Proceedings of the National Academy of Sciences*, 100(1):253–258.

Greicius, M. D., Supekar, K., Menon, V., and Dougherty, R. F. (2009). Resting-state functional connectivity reflects structural connectivity in the default mode network. *Cerebral Cortex*, 19(1):72–78.

Hagmann, P. (2005). From diffusion mri to brain connectomics.

Hagmann, P., Cammoun, L., Gigandet, X., Meuli, R., Honey, C. J., Wedeen, V. J., and Sporns, O. (2008). Mapping the structural core of human cerebral cortex. *PLoS biology*, 6(7):e159.

Hagmann, P., Sporns, O., Madan, N., Cammoun, L., Pienaar, R., Wedeen, V. J., Meuli, R., Thiran, J.-P., and Grant, P. (2010). White matter maturation reshapes structural connectivity in the late developing human brain. *Proceedings of the National Academy of Sciences*, 107(44):19067–19072.

Hamandi, K., Powell, H. W. R., Laufs, H., Symms, M. R., Barker, G. J., Parker, G. J. M., Lemieux, L., and Duncan, J. S. (2008). Combined EEG-fMRI and tractography to visualise propagation of epileptic activity. *Journal of Neurology, Neurosurgery and Psychiatry*, 79(5):594–597.

Healy Jr, D. M., Hendriks, H., and Kim, P. T. (1998). Spherical deconvolution. *Journal of Multivariate Analysis*, 67(1):1–22.

Hoch, M. J., Chung, S., Ben-Eliezer, N., Bruno, M. T., Fatterpekar, G. M., and Shepherd, T. M. (2016). New Clinically Feasible 3T MRI Protocol to Discriminate Internal Brain Stem Anatomy. *AJNR. American journal of neuroradiology*, 37(6):1058–65.

Honey, C. J., Sporns, O., Cammoun, L., Gigandet, X., Thiran, J. P., Meuli, R., and Hagmann, P. (2009). Predicting human resting-state functional connectivity from structural connectivity. *Proceedings of the National Academy of Sciences*, 106(6):2035–2040.

Huang, H., Zhang, J., van Zijl, P., and Mori, S. (2004). Analysis of noise effects on DTI-based tractography using the brute-force and multi-ROI approach. *Magnetic Resonance in Medicine*, 52(3):559–565.

Hubert, L. J. and Baker, F. B. (1977). The comparison and fitting of given classification schemes. *Journal of Mathematical Psychology*, 16(3):233–253.

Hüppi, P. S. and Dubois, J. (2006). Diffusion tensor imaging of brain development. *Seminars in Fetal and Neonatal Medicine*, 11(6):489–497.

Jakab, A., Kasprian, G., Schwartz, E., Gruber, G. M., Mitter, C., Prayer, D., Schöpf, V., and Langs, G. (2015). Disrupted developmental organization of the structural connectome in fetuses with corpus callosum agenesis. *Neuroimage*, 111:277–288.

Jenkinson, M., Beckmann, C. F., Behrens, T. E. J., Woolrich, M. W., and Smith, S. M. (2012). Fsl. *NeuroImage*, 62(2):782–790.

Jensen, J. H. and Helpern, J. A. (2010). MRI quantification of non-Gaussian water diffusion by kurtosis analysis. *NMR in Biomedicine*, 23(7):698–710.

Jeurissen, B., Leemans, A., Tournier, J.-D., Jones, D. K., and Sijbers, J. (2013). Investigating the prevalence of complex fiber configurations in white matter tissue with diffusion magnetic resonance imaging. *Human brain mapping*, 34(11):2747–2766.

Job, D. E., Dickie, D. A., Rodriguez, D., Robson, A., Danso, S., Pernet, C., Bastin, M. E., Boardman, J. P., Murray, A. D., Ahearn, T., Waiter, G. D., Staff, R. T., Deary, I. J., Shenkin, S. D., and Wardlaw, J. M. (2017). A brain imaging repository of normal structural mri across the life course: Brain images of normal subjects (brains). *NeuroImage*, 144:299–304. Data Sharing Part II.

Kelly, C. E., Cheong, J. L. Y., Molloy, C., Anderson, P. J., Lee, K. J., Burnett, A. C., Connelly, A., Doyle, L. W., and Thompson, D. K. (2014). Neural correlates of impaired vision in adolescents born extremely preterm and/or extremely low birthweight. *PLoS ONE*, 9(3).

Koch, M. A., Norris, D. G., and Hund-Georgiadis, M. (2002). An investigation of functional and anatomical connectivity using magnetic resonance imaging. *Neuroimage*, 16(1):241–250.

Kuner, R. and Flor, H. (2017). Structural plasticity and reorganisation in chronic pain. *Nature Reviews Neuroscience*, 18(1):20.

Küpper, H., Groeschel, S., Alber, M., Klose, U., Schuhmann, M. U., and Wilke, M. (2015). Comparison of different tractography algorithms and validation by intraoperative stimulation in a child with a brain tumor. *Neuropediatrics*, 46(1):72–75.

Lancichinetti, A. and Fortunato, S. (2012). Consensus clustering in complex networks. *Scientific Reports*, 2.

Le Bihan, D. and Breton, E. (1985). Imagerie de diffusion in-vivo par résonance magnétique nucléaire. *Comptes-Rendus de l'Académie des Sciences*, 93(5):27–34.

Le Bihan, D., Mangin, J.-F., Poupon, C., Clark, C. A., Pappata, S., Molko, N., and Chabriat, H. (2001). Diffusion tensor imaging: concepts and applications. *Journal of Magnetic Resonance Imaging*, 13:534–546.

Lee, S.-K., Mori, S., Kim, D. J., Kim, S. Y., Kim, S. Y., and Kim, D. I. (2004). Diffusion tensor mr imaging visualizes the altered hemispheric fiber connection in callosal dysgenesis. *American Journal of Neuroradiology*, 25(1):25–28.

Lei, X., Qiu, C., Xu, P., and Yao, D. (2010). A parallel framework for simultaneous eeg/fmri analysis: Methodology and simulation. *NeuroImage*, 52(3):1123 – 1134. Computational Models of the Brain.

Liégeois, F., Mahony, K., Connelly, A., Pigdon, L., Tournier, J.-D., and Morgan, A. T. (2013a). Pediatric traumatic brain injury: Language outcomes and their relationship to the arcuate fasciculus. *Brain and Language*, 127(3):388–398.

Liégeois, F., Tournier, J.-D., Pigdon, L., Connelly, A., and Morgan, A. T. (2013b). Corti-cobulbar tract changes as predictors of dysarthria in childhood brain injury. *Neurology*, 80(10):926–932.

Lim, J. C., Phal, P. M., Desmond, P. M., Nichols, A. D., Kokkinos, C., Danesh-Meyer, H. V., Kaye, A. H., and Moffat, B. A. (2015). Probabilistic MRI Tractography of the Optic Radiation Using Constrained Spherical Deconvolution: A Feasibility Study. *PLOS ONE*, 10(3):1–15.

Logothetis, N. K., Eschenko, O., Murayama, Y., Augath, M., Steudel, T., Evrard, H., Besserve, M., and Oeltermann, A. (2012). Hippocampal–cortical interaction during periods of subcortical silence. *Nature*, 491(7425):547.

Meilă, M. (2007). Comparing clusterings—an information based distance. *Journal of Multivariate Analysis*, 98(5):873–895.

Meoded, A., Katipally, R., Bosemani, T., Huisman, T. A., and Poretti, A. (2015). Structural connectivity analysis reveals abnormal brain connections in agenesis of the corpus callosum in children. *European radiology*, 25(5):1471–1478.

Mišić, B., Betzel, R. F., de Reus, M. A., van den Heuvel, M. P., Berman, M. G., McIntosh, A. R., and Sporns, O. (2016). Network-Level Structure-Function Relationships in Human Neocortex. *Cerebral Cortex*, 26(7):3285–3296.

Mori, S., Crain, B. J., Chacko, V. P., and Van Zijl, P. C. M. (1999). Three-dimensional tracking of axonal projections in the brain by magnetic resonance imaging. *Annals of Neurology*, 45(2):265–269.

Mormina, E., Briguglio, M., Morabito, R., Arrigo, A., Marino, S., Di Rosa, G., Micalizzi, A., Valente, E. M., Salpietro, V., Vinci, S. L., Longo, M., and Granata, F. (2016). A rare case of cerebellar agenesis: a probabilistic Constrained Spherical Deconvolution tractographic study. *Brain Imaging and Behavior*, 10(1):158–167.

Murray, A. L., Thompson, D. K., Pascoe, L., Leemans, A., Inder, T. E., Doyle, L. W., Anderson, J. F. I., and Anderson, P. J. (2016). White matter abnormalities and impaired attention abilities in children born very preterm. *NeuroImage*, 124:75–84.

Naidich, T., Duvernoy, H., Delman, B., Sorensen, A., Kollias, S., and Haacke, E. (2009). *Duvernoy's Atlas of the Human Brain Stem and Cerebellum*. Springer Vienna, Vienna.

Narizzano, M., Arnulfo, G., Ricci, S., Toselli, B., Tisdall, M., Canessa, A., Fato, M. M., and Cardinale, F. (2017). SEEG assistant: A 3DSlicer extension to support epilepsy surgery. *BMC Bioinformatics*, 18(1).

Northam, G. B., Liégeois, F., Chong, W. K., Baker, K., Tournier, J.-D., Wyatt, J. S., Baldeweg, T., and Morgan, A. (2012). Speech and oromotor outcome in adolescents born preterm: Relationship to motor tract integrity. *Journal of Pediatrics*, 160(3):402–409.

Owen, J. P., Li, Y.-O., Ziv, E., Strominger, Z., Gold, J., Bukhpun, P., Wakahiro, M., Friedman, E. J., Sherr, E. H., and Mukherjee, P. (2013). The structural connectome of the human brain in agenesis of the corpus callosum. *Neuroimage*, 70:340–355.

Paydar, A., Fieremans, E., Nwankwo, J. I., Lazar, M., Sheth, H. D., Adisetiyo, V., Helpern, J. A., Jensen, J. H., and Milla, S. S. (2014). Diffusional kurtosis imaging of the developing brain. *American Journal of Neuroradiology*, 35(4):808–814.

Pieterman, K., Batalle, D., Dudink, J., Tournier, J.-D., Hughes, E. J., Barnett, M., Benders, M. J., Edwards, A. D., Hoebeek, F. E., and Counsell, S. J. (2016). Cerebello-cerebral connectivity in the developing brain. *Brain Structure and Function*, pages 1–10.

Ray, S., Niebur, E., Hsiao, S. S., Sinai, A., and Crone, N. E. (2008). High-frequency gamma activity (80–150 hz) is increased in human cortex during selective attention. *Clinical Neurophysiology*, 119(1):116–133.

Raybaud, C. (2010). The corpus callosum, the other great forebrain commissures, and the septum pellucidum: anatomy, development, and malformation. *Neuroradiology*, 52(6):447–477.

Raybaud, C. and Girard, N. (1998). Anatomic mri study of commissural agenesis and dysplasia of the telencephalon (agenesis of the corpus callosum and related anomalies). clinical correlations and morphogenetic interpretation. *Neuro-Chirurgie*, 44(1 Suppl):38–60.

Reijneveld, J. C., Ponten, S. C., Berendse, H. W., and Stam, C. J. (2007). The application of graph theoretical analysis to complex networks in the brain. *Clinical neurophysiology*, 118(11):2317–2331.

Rubinov, M. and Sporns, O. (2010). Complex network measures of brain connectivity: uses and interpretations. *Neuroimage*, 52(3):1059–1069.

Salvan, P., Tournier, J. D., Batalle, D., Falconer, S., Chew, A., Kennea, N., Aljabar, P., Dehaene-Lambertz, G., Arichi, T., Edwards, A. D., et al. (2017). Language ability in preterm children is associated with arcuate fasciculi microstructure at term. *Human brain mapping*, 38(8):3836–3847.

Schaefer, A., Kong, R., Gordon, E. M., Laumann, T. O., Zuo, X.-N., Holmes, A. J., Eickhoff, S. B., and Yeo, B. T. (2017). Local-Global Parcellation of the Human Cerebral Cortex from Intrinsic Functional Connectivity MRI. *Cerebral Cortex*, pages 1–20.

Scheck, S. M., Pannek, K., Raffelt, D. A., Fiori, S., Boyd, R. N., and Rose, S. E. (2015). Structural connectivity of the anterior cingulate in children with unilateral cerebral palsy due to white matter lesions. *NeuroImage: Clinical*, 9:498–505.

Schell-Apacik, C. C., Wagner, K., Bihler, M., Ertl-Wagner, B., Heinrich, U., Klopocki, E., Kalscheuer, V. M., Muenke, M., and von Voss, H. (2008). Agenesis and dysgenesis of the corpus callosum: clinical, genetic and neuroimaging findings in a series of 41 patients. *American Journal of Medical Genetics Part A*, 146(19):2501–2511.

Severino, M., Tortora, D., Toselli, B., Uccella, S., Traverso, M., Morana, G., Capra, V., Veneselli, E., Fato, M. M., and Rossi, A. (2017). Structural connectivity analysis in children with segmental callosal agenesis. *American Journal of Neuroradiology*, 38(3):639–647.

Sharp, D. J., Scott, G., and Leech, R. (2014). Network dysfunction after traumatic brain injury. *Nature Reviews Neurology*, 10(3):156–166.

Skudlarski, P., Jagannathan, K., Calhoun, V. D., Hampson, M., Skudlarska, B. A., and Pearlson, G. (2008). Measuring brain connectivity: diffusion tensor imaging validates resting state temporal correlations. *Neuroimage*, 43(3):554–561.

Smith, R. E., Tournier, J.-D., Calamante, F., and Connelly, A. (2012). Anatomically-constrained tractography: Improved diffusion MRI streamlines tractography through effective use of anatomical information. *NeuroImage*, 62(3):1924–1938.

Smith, R. E., Tournier, J.-D., Calamante, F., and Connelly, A. (2013). SIFT: Spherical-deconvolution informed filtering of tractograms. *NeuroImage*, 67:298–312.

Sotiropoulos, S. N., Jbabdi, S., Xu, J., Andersson, J. L., Moeller, S., Auerbach, E. J., Glasser, M. F., Hernandez, M., Sapiro, G., Jenkinson, M., Feinberg, D. A., Yacoub, E., Lenglet, C., Van Essen, D. C., Ugurbil, K., and Behrens, T. E. (2013). Advances in diffusion MRI acquisition and processing in the Human Connectome Project. *NeuroImage*, 80:125–143.

Sotiropoulos, S. N. and Zalesky, A. (2017). Building connectomes using diffusion mri: Why, how and but. *NMR in Biomedicine*, page e3752.

Sporns, O. (2007). Brain connectivity. *Scholarpedia*, 2(10):4695. revision #91084.

Sporns, O. (2013). Structure and function of complex brain networks. *Dialogues in clinical neuroscience*, 15(3):247–62.

Sporns, O. (2014). Contributions and challenges for network models in cognitive neuroscience. *Nature neuroscience*, 17(5):652.

Sporns, O., Tononi, G., and Kötter, R. (2005). The human connectome: a structural description of the human brain. *PLoS computational biology*, 1(4):e42.

Stefanou, M. I., Lumsden, D. E., Ashmore, J., Ashkan, K., Lin, J. P., and Charles-Edwards, G. (2016). Tensor and non-tensor tractography for the assessment of the corticospinal tract of children with motor disorders: a comparative study.

Stejskal, E. O. and Tanner, J. E. (1965). Spin diffusion measurements: spin echoes in the presence of a time-dependent field gradient. *The journal of chemical physics*, 42(1):288–292.

Taussig, D., Chipaux, M., Lebas, A., Fohlen, M., Bulteau, C., Ternier, J., Ferrand-Sorbets, S., Delalande, O., and Dorfmüller, G. (2014). Stereo-electroencephalography (SEEG) in 65 children: an effective and safe diagnostic method for pre-surgical diagnosis, independent of age. *Epileptic disorders : international epilepsy journal with videotape*, 16(3):280–95.

Thompson, D. K., Chen, J., Beare, R., Adamson, C. L., Ellis, R., Ahmadzai, Z. M., Kelly, C. E., Lee, K. J., Zalesky, A., Yang, J. Y., Hunt, R. W., Cheong, J. L., Inder, T. E., Doyle, L. W., Seal, M. L., and Anderson, P. J. (2016). Structural connectivity relates to perinatal factors and functional impairment at 7years in children born very preterm. *NeuroImage*, 134:328–337.

Thompson, D. K., Thai, D., Kelly, C. E., Leemans, A., Tournier, J.-D., Kean, M. J., Lee, K. J., Inder, T. E., Doyle, L. W., Anderson, P. J., and Hunt, R. W. (2014). Alterations in the optic radiations of very preterm children - Perinatal predictors and relationships with visual outcomes. *NeuroImage: Clinical*, 4:145–153.

Toselli, B., Tortora, D., Severino, M., Arnulfo, G., Canessa, A., Morana, G., Rossi, A., and Fato, M. M. (2017). Improvement in White Matter Tract Reconstruction with Constrained Spherical Deconvolution and Track Density Mapping in Low Angular Resolution Data: A Pediatric Study and Literature Review. *Frontiers in Pediatrics*, 5:182.

Tournier, J.-D., Calamante, F., and Connelly, A. (2007). Robust determination of the fibre orientation distribution in diffusion MRI: Non-negativity constrained super-resolved spherical deconvolution. *NeuroImage*, 35(4):1459–1472.

Tournier, J.-D., Calamante, F., and Connelly, A. (2009). How many diffusion gradient directions are required for HARDI. In *Proc. Intl. Soc. Mag. Reson. Med*, volume 17, page 358.

Tournier, J.-D., Calamante, F., and Connelly, A. (2010). Improved probabilistic streamlines tractography by 2nd order integration over fibre orientation distributions. *Proceedings of the International Society for Magnetic Resonance in Medicine*, 88(2003):2010.

Tournier, J.-D., Calamante, F., and Connelly, A. (2012). MRtrix: Diffusion tractography in crossing fiber regions. *International Journal of Imaging Systems and Technology*, 22(1):53–66.

Tournier, J.-D., Calamante, F., and Connelly, A. (2013). Determination of the appropriate b value and number of gradient directions for high-angular-resolution diffusion-weighted imaging. *NMR in Biomedicine*, 26(12):1775–1786.

Tournier, J.-D., Calamante, F., Gadian, D. G., and Connelly, A. (2004). Direct estimation of the fiber orientation density function from diffusion-weighted MRI data using spherical deconvolution. *NeuroImage*, 23(3):1176–1185.

Tournier, J.-D., Mori, S., and Leemans, A. (2011). Diffusion tensor imaging and beyond. *Magnetic Resonance in Medicine*, 65(6):1532–1556.

Tovar-Moll, F., Moll, J., de Oliveira-Souza, R., Bramati, I., Andreiuolo, P. A., and Lent, R. (2006). Neuroplasticity in human callosal dysgenesis: a diffusion tensor imaging study. *Cerebral Cortex*, 17(3):531–541.

Tovar-Moll, F., Monteiro, M., Andrade, J., Bramati, I. E., Vianna-Barbosa, R., Marins, T., Rodrigues, E., Dantas, N., Behrens, T. E., de Oliveira-Souza, R., et al. (2014). Structural and functional brain rewiring clarifies preserved interhemispheric transfer in humans born without the corpus callosum. *Proceedings of the National Academy of Sciences*, 111(21):7843–7848.

Traag, V., Waltman, L., and van Eck, N. J. (2018). From louvain to leiden: guaranteeing well-connected communities. *arXiv preprint arXiv:1810.08473*.

Vanhatalo, S. and Kaila, K. (2006). Development of neonatal EEG activity: From phenomenology to physiology. *Seminars in Fetal and Neonatal Medicine*, 11(6):471–478.

Wahl, M., Strominger, Z., Jeremy, R., Barkovich, A., Wakahiro, M., Sherr, E., and Mukherjee, P. (2009). Variability of homotopic and heterotopic callosal connectivity in partial agenesis of the corpus callosum: a 3t diffusion tensor imaging and q-ball tractography study. *American Journal of Neuroradiology*, 30(2):282–289.

Warach, S., Chien, D., Li, W., Ronthal, M., and Edelman, R. (1992). Fast magnetic resonance diffusion-weighted imaging of acute human stroke. *Neurology*, 42(9):1717–1717.

Wedeen, V. J., Wang, R. P., Schmahmann, J. D., Benner, T., Tseng, W. Y. I., Dai, G., Pandya, D. N., Hagmann, P., D'Arceuil, H., and de Crespigny, A. J. (2008). Diffusion spectrum magnetic resonance imaging (DSI) tractography of crossing fibers. *NeuroImage*, 41(4):1267–1277.

Yeo, B. T. T., Krienen, F. M., Sepulcre, J., Sabuncu, M. R., Lashkari, D., Hollinshead, M., Roffman, J. L., Smoller, J. W., Zollei, L., Polimeni, J. R., Fischl, B., Liu, H., and Buckner, R. L. (2011). The organization of the human cerebral cortex estimated by intrinsic functional connectivity. *Journal of neurophysiology*, 106(3):1125–1165.

Yepes-Calderon, F., Lao, Y., Fillard, P., Nelson, M. D., Panigrahy, A., and Lepore, N. (2017). Tractography in the clinics: Implementing a pipeline to characterize early brain development. *NeuroImage: Clinical*, 14:629–640.

Zalesky, A., Fornito, A., and Bullmore, E. T. (2010). Network-based statistic: identifying differences in brain networks. *Neuroimage*, 53(4):1197–1207.

Zhang, H., Schneider, T., Wheeler-Kingshott, C. A. M., and Alexander, D. C. (2012). NODDI: Practical in vivo neurite orientation dispersion and density imaging of the human brain. *NeuroImage*, 61(4):1000–1016.

Appendix A

Methods: Diffusion-weighted MRI, diffusion tensor imaging and constrained spherical deconvolution

A.1   The diffusion-weighted MRI signal and the *b*-value

Diffusion-weighted MRI (DWI) is a specific type of magnetic resonance imaging (MRI) which measures the random Brownian motion of water molecules within a tissue. This motion is driven by the thermal energy of the molecules, and is perfectly equal in all directions (*isotropic diffusion*) in an homogeneous medium. In structured tissue, however, this diffusion is restricted by the presence of cell membranes and macromolecules and thus is not equal in all directions (*anisotropic diffusion*). In a given amount of time, molecules in different locations of the imaged part will experience different amounts of movement, depending on the organization of the tissue in that specific voxel. This difference in diffusion is exploited to produce contrast in DWI images.

To sensitize the images to water diffusion, the homogeneity of the magnetic field is varied linearly using a pulsed field gradient, which causes the protons to precess with different rates depending on their position along the gradient. This causes de-phasing of the spins, and thus signal loss. After a given amount of time, another gradient pulse is applied to the field, having equal magnitude but opposite direction than the first gradient: if the protons have not moved between the gradient applications, this causes a perfect re-phasing of the spins, and thus no signal loss. However, protons which have moved during this interval will not be

perfectly refocused and will cause a reduction in the signal measured by the machine after the second gradient. The measured signal can be expressed as [Stejskal and Tanner (1965)]:

$$S = S_0 \exp\left[-\gamma^2 G^2 \delta^2 \left(\Delta - \frac{\delta}{3} \right) D \right] \tag{A.1}$$

where S is the signal after application of the gradients, S_0 is the signal without diffusion weighting, γ is the gyromagnetic ratio, G and δ the strength and duration of the gradient pulse, Δ the interval between the de-phasing and re-phasing pulses, and D the diffusion coefficient. This equation was simplified by [Le Bihan and Breton (1985)] by gathering all gradient terms in a single factor, called the "b factor" or b-value, which depends only by the acquisition parameters. The signal attenuation thus becomes:

$$S = S_0 \exp(-bD) \tag{A.2}$$

As introduced before, isotropic diffusion of water is equal in all directions of the space and can be described simply by a constant D. If the diffusion is anisotropic, however, a tensor $\underline{\mathbf{D}}$ is required to fully describe molecular movement along all directions in space. Diffusion Tensor Imaging was the first method developed to characterise this tensor.

A.2 Diffusion Tensor Imaging

Diffusion Tensor Imaging (DTI) was introduced by Basser et al. (1994) to describe the diffusion of water molecules in body tissues, and specifically in the brain. The anisotropic nature of this diffusion means that a constant is not sufficient to characterise it, but a tensor is needed to fully describe the different amounts of movement in all directions. This tensor is of the form:

$$\underline{\mathbf{D}} = \begin{array}{ccc} D_{xx} & D_{xy} & D_{xz} \\ D_{yx} & D_{yy} & D_{yz} \\ D_{zx} & D_{zy} & D_{zz} \end{array} \tag{A.3}$$

and is symmetric ($D_{ij} = D_{ji}$). Equation A.2 then can be expressed as:

$$S = S_0 \exp\left(-\sum_{i=x,y,z} \sum_{j=x,y,z} \mathbf{b}_{ij} \underline{\mathbf{D}}_{ij} \right) \tag{A.4}$$

where $\underline{\mathbf{b}}$ is the *b*-value matrix, expressing the *b*-value along each direction. In practice, a single *b*-value is used for all directions, since it is neither necessary nor efficient in terms of SNR to apply different *b*-values for different directions [Le Bihan et al. (2001)].

Since the diffusion tensor is symmetric, the minimal set of images needed for its estimation is composed of six volumes acquired along six different gradient directions, plus an image with no diffusion weighting ($b = 0$). In practice, data is collected along as many directions as possible, distributed as uniformly as possible on the 3D sphere; advanced diffusion analysis and fibre tracking methods require a uniform sampling of the space, a specific number of gradient directions and a minimum *b*-value (see for example Tournier et al. (2009)), introducing constraints on their application in specific environments.

From the diffusion tensor $\underline{\mathbf{D}}$, many diffusion and anisotropy indices can be computed [Le Bihan et al. (2001)]. The most commonly used are the mean diffusivity (MD), describing the overall diffusion in a voxel, and the fractional anisotropy (FA), which quantifies the fraction of $\underline{\mathbf{D}}$ that can be explained with anisotropic diffusion. These indices are defined as:

$$
\begin{aligned}
\mathrm{MD} &= \frac{D_{xx} + D_{yy} + D_{zz}}{3} \\
\mathrm{FA} &= \sqrt{\frac{3}{2} \frac{[(\lambda_1 - \langle\lambda\rangle)^2 + (\lambda_2 - \langle\lambda\rangle)^2 + (\lambda_3 - \langle\lambda\rangle)^2]}{\lambda_1^2 + \lambda_2^2 + \lambda_3^2}}
\end{aligned}
\tag{A.5}
$$

where λ_i is the *i*-th eigenvalue of the tensor $\underline{\mathbf{D}}$ and $\langle\lambda\rangle = (\lambda_1 + \lambda_2 + \lambda_3)/3$. By computing the value of these parameters for each voxel of a DWI volume, we obtain parametric maps which are often used in clinical applications: for example, MD maps can highlight variations of water diffusivity in ischaemic regions very early after the ischaemic event, well before the appearance of abnormalities in conventional MRI, allowing to intervene when brain tissue is still salvageable [Warach et al. (1992); Le Bihan et al. (2001)]. The degree of diffusion anisotropy in WM has been shown to be proportional to the myelination of WM fibres in a voxel: for this reason, FA maps are often used to measure myelin integrity for microstructural WM analysis or brain maturation mapping in neonates and infants [Le Bihan et al. (2001)].

From the eigenvectors of $\underline{\mathbf{D}}$ we can also infer information about the directionality of the diffusion in a voxel, by assuming that the direction of the fibres is collinear with the first eigenvector $\mathbf{v}_1$, which is associated with the largest eigenvalue λ_1. By selecting for each voxel the first eigenvector of the voxels' diffusion tensor, we obtain a vector field which can be used as input for tractography algorithms to produce a reconstruction of the major WM fibre pathways in the brain.

A.2.1   Limitations of DTI

The assumption of a single main diffusion direction per voxel means that DTI can successfully resolve only a single WM fibre population in a single voxel. This limitation poses the problem of correctly reconstructing voxels containing more complex configuration of fibres, such as crossing or 'kissing' tracts (two fibre populations meeting and then separating again in the same voxel) and other multiple-fibre configuration, which is particularly important since it has been shown that about 90% of WM voxels in the brain contain multiple fibre tracts [Jeurissen et al. (2013)].

In the last decade, many methods have been developed to address this limitation (see for example Tournier et al. (2011) and Daducci et al. (2014) for reviews). These methodologies have not yet been integrated in the clinical practice, where DTI is still the most commonly used method of WM mapping and study. Some of the reasons for this missed adoption are scan times unfeasible for the clinical application, software and hardware availability and acquisition constraints [Farquharson et al. (2013)]. Among the many higher-order models overcoming the limitations of DTI, constrained spherical deconvolution (CSD) [Tournier et al. (2004)] has been shown many times to combine robustness to crossing-fibres effects and feasible time and hardware constraints (see for example Farquharson et al. (2013); Auriat et al. (2015); Stefanou et al. (2016)).

A.3   Constrained spherical deconvolution

The constrained spherical deconvolution model is based on the assumption that the diffusion signal originating from separate regions of the analysed sample will add independently, generating the total measured diffusion signal. This assumption is based on the time scale of the molecular diffusion: the average displacement of a water molecule during a typical diffusion-weighted acquisition is expected to be of the order of 10 μm [Tournier et al. (2004)], meaning that water molecules will likely visit only regions separated by a few tens of microns during the experiment. A second assumption is that the radius of curvature for curved fibre populations is greater than this length scale, and thus there can be no exchange between distinct sections of a single fibre tract. Under these assumptions, the measured diffusion signal from a voxel can be approximated as the sum of the signals from each fibre population contained in the voxel.

A third assumption made from this model is that the signal generated from a single, coherently-oriented fibre population is identical for all fibre tracts in the brain, and thus

the only difference between signals produced by different fibre populations is due to their orientation. The signal attenuation arising from such a coherent fibre tract is then represented as a response function $R(\theta)$, which is axially symmetric and depends only on the elevation angle θ expressed in spherical coordinates (where $\theta = 0$ if the tract is aligned with the z-axis). This single-fibre response can be estimated directly from the acquired data, using the diffusion signal from regions containing a single, coherently-oriented fibre population: these voxels are often selected among those with the highest FA coefficient, which indicates high diffusion anisotropy and thus a single, well-defined diffusion direction, suggesting the presence of a single fibre tract in the voxel.

Given this response function, the signal measured from a voxel containing several fibre populations can then be written as:

$$S(\theta, \phi) = \sum_i f_i \, \hat{A}_i \, R(\theta) \tag{A.6}$$

where f_i is the i-th fibre population in the voxel, ϕ is the azimuthal angle in spherical coordinates and $\hat{A}_i$ expresses a rotation onto the direction (θ_i, ϕ_i). This equation expresses the signal from a voxel as the sum of the single-fibre response function from each population, weighted by their volume fractions and aligned along their respective orientations. This is equivalent to the convolution of the response function $R(\theta)$ with a fibre orientation density (FOD) function over the unit sphere:

$$S(\theta, \phi) = F(\theta, \phi) \otimes R(\theta) \tag{A.7}$$

where $F(\theta, \phi)$ is the FOD function, expressing the fraction of fibres in the voxel aligned with the direction (θ, ϕ). Given a voxel containing N fibre populations, $F(\theta, \phi)$ is the sum of N Dirac deltas, each pointing along the direction of one fibre population and weighted by the corresponding volume fraction. If the single-fibre response $R(\theta)$ is known (or estimable from data), the FOD function can then be obtained through a spherical deconvolution of the acquired signal $S(\theta, \phi)$ with $R(\theta)$, thus obtaining the distribution of diffusion directions in the selected voxel.

Details on the spherical deconvolution process can be found in Healy Jr et al. (1998). Spherical harmonics are a complete orthonormal basis set of functions on the sphere; each can be denoted by its harmonic order n - directly proportional to angular frequency - and phase factor m ($n \geq 0$; $-n \leq m \leq n$). Even values of n identify symmetric harmonics, while harmonics with odd n are anti-symmetric. In the same way, rotational harmonics are a

complete orthonormal set over the rotations space and are denoted by harmonic order n and two phase factors, l and m ($n \geq 0$; $-n \leq l, m \leq n$).

The spherical convolution operation can be defined as the effect of a convolution kernel - composed by a set rotations - on a function over a sphere [Healy Jr et al. (1998); Tournier et al. (2004)]. Given the $2n+1$ vector $\underline{\mathbf{F}}^n$ representing the n-th order spherical harmonic decomposition of $F(\theta, \phi)$ and the $(2n+1)(2n+1)$ matrix $\mathbf{R}^n$ representing the n-th order rotational harmonic decomposition of $R(\theta)$, we can write:

$$\underline{S}^n = \mathbf{R}^n \, \underline{\mathbf{F}}^n \tag{A.8}$$

which expresses the n-th order spherical harmonic representation of $S(\theta, \phi)$. The spherical deconvolution operation can then be performed by inverting each $\mathbf{R}^n$ matrix to compute $\underline{\mathbf{F}}^n$. Since diffusion is symmetric about the origin, only even components are non-zero; moreover, since $R(\theta)$ is axially symmetric, $\mathbf{R}^n$ is a single constant for each harmonic order n. The spherical harmonics representation of $S(\theta, \phi)$ can be obtained with a linear least squares fit, as shown in Alexander et al. (2002), estimating the response function $R(\theta)$ from the data as described above.

The maximum harmonic order n_{max} which can be estimated depends on the number of independent samples of the signal attenuation, and thus, in practice, from the gradient directions used in the acquisition sequence. Given a value of n_{max}, the minimum number of separate directions required is given by $1/2 \, (n_{max} + 1) \, (n_{max} + 2)$ and is the number of spherical harmonics coefficients contained in the series up to n_{max} [Tournier et al. (2009)]. It is necessary to note that the spherical deconvolution operation is increasingly sensitive to noise as the maximum spherical harmonic increases, which introduces the need for an attenuation or the elimination of the higher harmonic components to limit noise effects [Tournier et al. (2004)].

Appendix B

Supplemental Material

Table B.1 Clinical, genetic, and neuroradiologic findings of patients with segACC. ACH indicates anterior commissure hypoplasia; ACTH, adrenocorticotropic hormone; BAEP, brain stem auditory-evoked potentials; CGH, comparative genomic hybridization; CS, cesarean delivery; del, deletion; dup, duplication; EEG, electroencephalography; GH, growth hormone; IP-II, incomplete partition type II; IUGR, intrauterine growth retardation; NA, not available; OFC, occipital frontal circumference; PFO, patent foramen ovale; PNH, periventricular nodular heterotopia; SOD, septo-optic dysplasia; TSH, thyroid-stimulating hormone; VEP, visual-evoked potentials; VSD, ventricular septal defect; —, normal; +, abnormal.

	Control	PVC	SegACC
Consistency of individual networks with the consensus network	0.844 ± 0.02	0.845 ± 0.059	0.852 ± 0.02
Consistency between individual networks	0.704 ± 0.083	0.707 ± 0.082	**0.647 ± 0.038***

Table B.2 Mean network consistency (correlation coefficient of connection strengths). Bold font and asterisk indicate significant difference from control and PVC groups ($P < 0.05$).

Module 1	Module 2	Module 3	Module 4	Module 5
L caudal anterior cingulate	L bankssts	L paracentral	L caudal middle frontal	R bankssts
L cuneus	L entorhinal	R caudal middle frontal	L frontal pole	R cuneus
L isthmus cingulate	L fusiform	R insula	L insula	R entorhinal
L posterior cingulate	L inferior parietal	R lateral orbitofrontal	L lateral orbitofrontal	R fusiform
L precuneus	L inferior temporal	R paracentral	L medial orbitofrontal	R inferoparietal
L rostral anterior cingulate	L lateral occipital	R pars opercularis	L pars opercularis	R inferotemporal
L superior parietal	L lingual	R pars orbitalis	L pars orbitalis	R lateral occipital
R caudal anterior cingulate	L middle temporal	R pars triangularis	L pars triangularis	R lingual
R isthmus cingulate	L parahippocampal	R postcentral	L postcentral	R middle temporal
R posterior cingulate	L pericalcarine	R precentral	L precentral	R parahippocampal
R precuneus	L superior temporal	R rostral middle frontal	L rostral middle frontal	R pericalcarine
R superior parietal	L supramarginal	R superior frontal	L superior frontal	R superotemporal
	L temporal pole	L cerebellum cortex	R frontal pole	R supramarginal
	L transverse temporal	R accumbens area	R medial orbitofrontal	R temporal pole
	L hippocampus	R amygdala	R rostral anterior cingulate	R transverse temporal
		R caudate	L accumbens area	R hippocampus
		R cerebellum cortex	L amygdala	
		R pallidum	L caudate	
		R putamen	L pallidum	
		R thalamus proper	L putamen	
			L thalamus proper	

Table B.3 Modules identified in healthy controls, with assignment of nodes to each module. "Bankssts" indicates cortical areas around superior temporal sulcus.

Module 1	Module 2	Module 3	Module 4	Module 5
L caudal anterior cingulate	L bankssts	R caudal middle frontal	L caudal middle frontal	R bankssts
L paracentral	L cuneus	R frontal pole	L entorhinal	R entorhinal
L posterior cingulate	L inferior parietal	R lateral orbitofrontal	L frontal pole	R fusiform
L rostral anterior cingulate	L inferior temporal	R medial orbitofrontal	L fusiform	R inferior parietal
L superior frontal	L isthmus cingulate	R paracentral	L insula	R inferior temporal
R caudal anterior cingulate	L lateral occipital	R pars opercularis	L lateral orbitofrontal	R insula
R cuneus	L lingual	R pars orbitalis	L medial orbitofrontal	R lateral occipital
R isthmus cingulate	L middle temporal	R pars triangularis	L parahippocampal	R lingual
R posterior cingulate	L pericalcarine	R precentral	L pars opercularis	R middle temporal
R precuneus	L precuneus	R rostral middle frontal	L pars orbitalis	R parahippocampal
R rostral anterior cingulate	L superior parietal	L cerebellum cortex	L pars triangularis	R pericalcarine
R superior frontal	L superior temporal	R accumbens area	L postcentral	R postcentral
	L supramarginal	R amygdala	L precentral	R superior parietal
	L transverse temporal	R caudate	L rostral middle frontal	R superior temporal
		R cerebellum cortex	L temporal pole	R supramarginal
		R pallidum	L accumbens area	R temporal pole
		R putamen	L amygdala	R transverse temporal
		R thalamus proper	L caudate	R hippocampus
			L hippocampus	
			L pallidum	
			L putamen	
			L thalamus proper	

Table B.4 Modules identified in subjects with PVC, with assignment of nodes to each module. "Bankssts" indicates cortical areas around superior temporal sulcus.

Module 1	Module 2	Module 3	Module 4
L bankssts	L caudal anterior cingulate	L caudal middle frontal	R bankssts
L cuneus	L medial orbitofrontal	L entorhinal	R cuneus
L inferior parietal	L rostral anterior cingulate	L frontal pole	R entorhinal
L inferior temporal	R caudal anterior cingulate	L fusiform	R fusiform
L lateral occipital	R caudal middle frontal	L insula	R inferior parietal
L lingual	R frontal pole	L isthmus cingulate	R inferior temporal
L middle temporal	R lateral orbitofrontal	L lateral orbitofrontal	R insula
L pericalcarine	R medial orbitofrontal	L paracentral	R isthmus cingulate
L superior temporal	R paracentral	L parahippocampal	R lateral occipital
L supramarginal	R pars opercularis	L pars opercularis	R lingual
L transverse temporal	R pars orbitalis	L pars orbitalis	R middle temporal
	R pars triangularis	L pars triangularis	R parahippocampal
	R posterior cingulate	L postcentral	R pericalcarine
	R precentral	L posterior cingulate	R postcentral
	R rostral anterior cingulate	L precentral	R precuneus
	R rostral middle frontal	L precuneus	R superior parietal
	R superior frontal	L rostral middle frontal	R superior temporal
	R accumbens area	L superior frontal	R supramarginal
	R caudate	L superior parietal	R temporal pole
	R cerebellum cortex	L temporal pole	R transverse temporal
	R pallidum	L accumbens area	R amygdala
	R putamen	L amygdala	R hippocampus
	R thalamus proper	L caudate	
		L cerebellum cortex	
		L hippocampus	
		L pallidum	
		L putamen	
		L thalamus proper	

Table B.5 Modules identified in patients with segmental callosal agenesis, with assignment of nodes to each module. "Bankssts" indicates cortical areas around superior temporal sulcus.
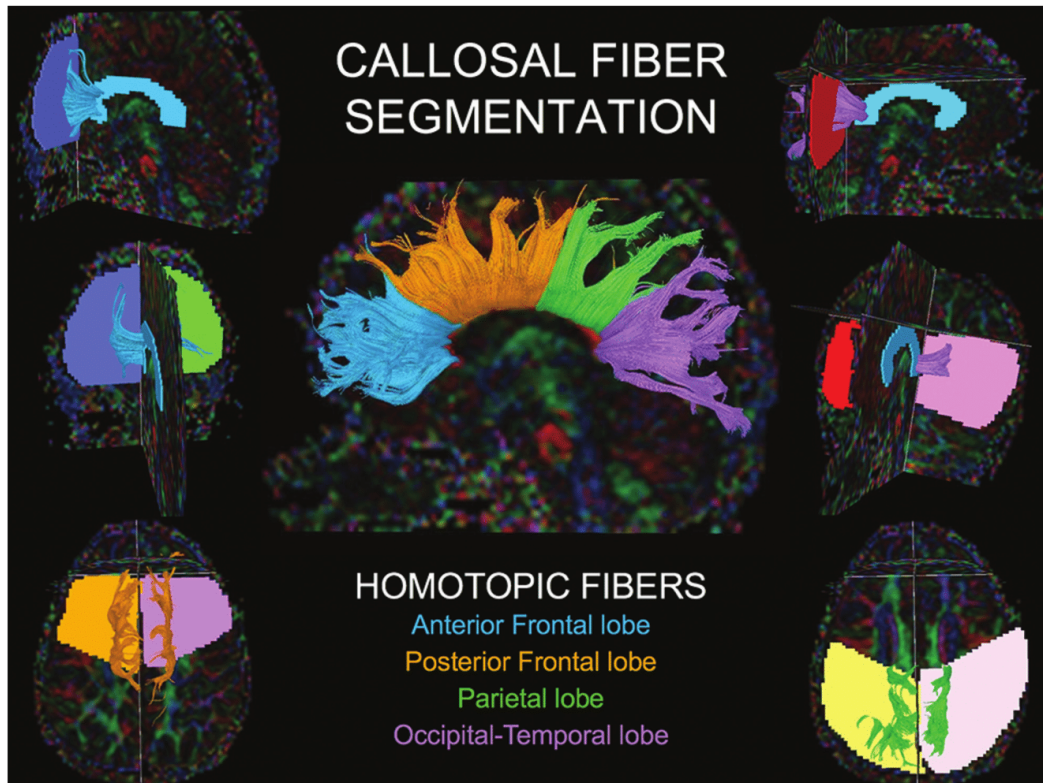
Figure B.1 Callosal tract segmentation procedure, shown for a control subject. A region of interest is first drawn on the midline sagittal section of fractional anisotropy colored maps to include all callosal fibers. These fibers are further segmented and colored according to their projections to specific lobar areas (i.e., homotopic anterior and posterior frontal, parietal, and occipitotemporal tracts [central image]). For the anterior frontal lobe projections, 2 additional ROIs are placed on a coronal section in each hemisphere anterior to the rostrum (left upper and middle images). For the posterior frontal lobe and parietal lobe projections, an axial section is chosen at the most posterior edge of the parieto-occipital sulcus. Two ROIs for posterior frontal projections are then placed to encompass the region between the coronal section used for anterior frontal fibers and the central sulcus (left lower image). Two ROIs for parietal lobe connections are placed on the same axial section, in the region posterior to the central sulcus (right lower image). Projections to the occipital and temporal lobes are segmented by using 2 ROIs placed on coronal images posterior to the callosum, encompassing regions inferior to the parieto-occipital sulcus (right upper and middle images).
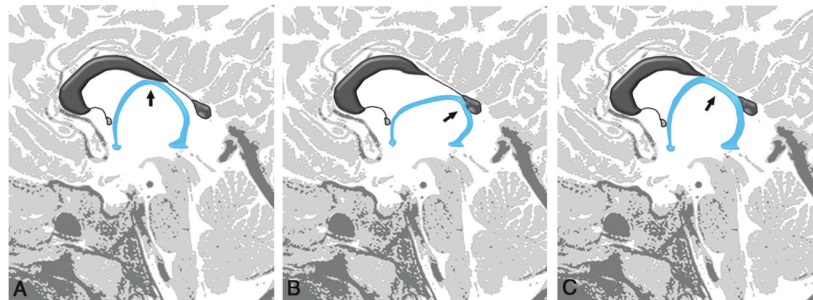
Figure B.2 Anatomic schemes of the 3 types of segmental callosal agenesis. In segACC type I (left), the fornices and the hippocampal commissure lie beneath the anterior callosal segment (arrow). In segACC type II (middle), the fornices and the hippocampal commissure lie beneath the posterior callosal segment (arrow). In segACC type III (right), the intermediate segment of the commissural plate is made of the joining fornices and hippocampal commissure (arrow).

List of publications

International peer-reviewed papers

1. Severino, M., Tortora, D., **Toselli, B.**, Uccella, S., Traverso, M., Morana, G., Capra, V., Veneselli, E., Fato, M.M., and Rossi, A. (2017). *Structural connectivity analysis in children with segmental callosal agenesis*. American Journal of Neuroradiology, 38(3), 639–647.

2. Narizzano, M., Arnulfo, G., Ricci, S., **Toselli, B.**, Tisdall, M., Canessa, A., Fato, M.M., and Cardinale, F. (2017). *SEEG assistant: A 3DSlicer extension to support epilepsy surgery*. BMC Bioinformatics, 18(1).

3. **Toselli, B.**, Tortora, D., Severino, M., Arnulfo, G., Canessa, A., Morana, G., Rossi A., and Fato, M. M. (2017). *Improvement of white matter tract reconstruction with constrained spherical deconvolution and track-density mapping in low angular resolution data: a pediatric study and literature review*. Frontiers in Pediatrics, 5, 182.

4. Tortora, D. , Severino, M. , Sedlacik, J. , **Toselli, B.**, Malova, M. , Parodi, A. , Morana, G. , Fato, M. M., Ramenghi, L. A. and Rossi, A. (2018). *Quantitative susceptibility map analysis in preterm neonates with germinal matrix-intraventricular hemorrhage*. J. Magn. Reson. Imaging, 48: 1199-1207.

Posters at conferences

1. **Toselli B.**, Tortora D., Severino M., Morana G., Rossi A., and Fato M.M., *Feasibility of constrained spherical deconvolution and probabilistic tractography in the pediatric clinical setting* (preliminary results). 5th GNB Congress in Naples (Italy), 20-22 June 2016.

2. **Toselli B.**, Tortora D., Severino M., Morana G., Rossi A., and Fato M.M., *Feasibility of constrained spherical deconvolution in diffusion imaging of children*. ISMRM

Workshop "Breaking the Barriers in Diffusion MRI" in Lisbon (Portugal), 11-16 September 2016.

3. **Toselli B.**, Chesi M., Arnulfo G., Canessa A., Tortora D., Severino M., Rossi A. and Fato M.M., *Comparison between NODDI metrics acquired at 3T and 7T in the human brain*. 6th GNB Congress in Milan (Italy), 25-27 June 2018.

4. **Toselli B.**, Nobili L., Rubino A., Fato M.M., Palva M. and Arnulfo G., *Comparison of structural and functional network-level brain connectivity in the healthy adult*. 25th OHBM Annual Meeting in Rome (Italy), 9-13 June 2019 (*accepted*).